DISSERTATION

Current-induced Domain Wall Dynamics Probed by Electrical Transport Measurements

zur Erlangung des akademischen Grades des
Doktors der Naturwissenschaften (Dr. rer. nat.)
an der Universität Konstanz
Mathematisch-Naturwissenschaftliche Sektion
Fachbereich Physik

vorgelegt von
Jan Arno Heinen

25. Juni 2012

Dissertation an der Universtität Konstanz

Tag der mündlichen Prüfung: 14.06.2012
erster Referent: Prof. Dr. Mathias Kläui
zweiter Referent: Prof. Dr. Ulrich Nowak

Zusammenfassung

Der Bedarf an immer besseren Speichermedien für die rasant anwachsende Anzahl an Informationen erweckte ein reges Interesse an neuen Speicherkonzepten. So entstand ein neues Forschungsfeld, die Spintronic. Ein Teilbereich dieser neuen Forschung beschäftigt sich mit der gezielten Manipulation von magnetischen Domänen mittels injizierten spin-polarisierten Strömen. Von großem Interesse sind hierbei die Übergangsbereiche zwischen den magnetischen Domänen, die so genannten Domänenwände. Die Forschungsergebnisse der letzten Jahre zeigen, dass mehrere Faktoren zur strominduzierten Domänenwandbewegung beitragen. Hierbei sind folgende Faktoren relevant: Joule-Wärme, Oersted-Feld-Effekte und vor allem die Spintransfer-Effekte (adiabatisch und nicht-adiabatisch).

Die vorliegende Arbeit befasst sich zuerst mit dem Aufbau einer Messapparatur zur Detektion von strominduzierten Domänenwandbewegungen und der Separation der zugrunde liegenden Faktoren. In Bezug auf spintronische Anwendungen ist vor allem die Bestimmung des nicht-adiabatischen Spintransfers von großem Interesse, da durch diese schnelle Domänenwandbewegungen ermöglicht werden. Der Nicht-adiabatizitäts-Faktor β dient hierbei als eine quantitative Größe (je größer desto schneller die Domänenwand).

Zunächst steht die Charakterisierung von ferromagnetischen Nanostrukturen mittels des Magnetowiderstandes im Vordergrund. Hierzu wurden die untersuchten Materialien zunächst in zwei Klassen eingeteilt: Die in-der-Ebene magnetisierten Materialien und diejenigen, deren Magnetisierung senkrecht zur Ebene ausgerichtet sind. Die Heusler-Legierung $Co_2FeAl_{0.4}Si_{0.6}$, welche der ersten Klasse zugeordnet wurde, zeigte während der Studien temperaturabhängige anisotropische Magnetowiderstandsänderungen, sowie

einen temperaturabhängigen, asymmetrischen planaren Hall-Effekt. Der erstere Effekt wird vermutlich durch Spannungen im Material ausgelöst. Der zweite Effekt tritt im Zusammenhang mit speziellen kristallographischen Strukturen auf, die generell bei Heusler-Legierungen präsent sind. Allerdings können in diesem Material Domänenwand-Positionen nicht einfach detektiert werden, so dass keine Studien zu strominduzierter Domänenwandbewegung durch geführt wurden.

Die zweite Klasse der Materialien hingegen zeigte ausgeprägte extraordinäre Hall-Effekte, mittels derer sich die Präsenz von Domänwanden in Hall-Kreuz-Geometrien nachweisen ließen. Genauere Untersuchungen des extraordinären Hall-Effektes ergaben eine starke Abhängigkeit von den Grundelementen der jeweiligen Zusammensetzung der Materialien. Jedoch unabhängig vom Grundelement, Platin oder Nickel, zeigte sich die Präsenz von Skew-Streuungs-Effekten und den kombinierten intrinsischen und Side-Jump-Effekt in den Temperaturbereichen mit konstanter Sättigungsmagnetisierung. Die Erweiterung der Multilagen mit CoFeB zeigt eine Verstärkung aller Effekte.

Abschließend beschäftigt sich die Arbeit mit dem eigentlichen Ziel, der strominduzierten Domänenwandbewegung. Basierend auf den Grundlagen früherer Forschungsarbeiten wurde ein Ansatz zur Separation der Mechanism, die an der Domänenwandbewegung beteiligt sind, mittels Symmetrieabhängigkeiten der einzelnen Faktoren erstellt. Dies ermöglicht die Bestimmung des Anteils des Spintransfers sowohl für ein Co/Pt Multilagenmaterial als auch für weitere Materialien basierend auf Nickel. Ein dominanter nicht-adiabatischer Spintransfer wurde, hier im Falle des Co/Pt Multilagenmaterials, gefunden und die Nicht-adiabatizitäts-Konstante $\beta = 0.24$ bestimmt, die eine gute Übereinstimmung mit vorangegangenen Experimenten zeigt. Für das Co/Ni Multilagematerial hingegen wurde ein dominanter adiabatischer Spintransfer bestimmt, welcher eine hohe Stromdichte im Bereich von $1 \cdot 10^{12}\,\mathrm{A/m^2}$ benötigt.

Das letzte Experiment konzentrierte sich auf thermischaktivierte Domänenwandbewegungen bei geringen Stromdichten um die Joule-Wärme-Effekte zu reduzieren. Die gleichzeitige Änderung von Strom und externen Magnetfeldern erlaubt es zwei voneinander unabhängige Ansätze zur selben Zeit an der gleichen Proben zu testen. Die Ergebnisse zeigen, dass sich die durch diese Ansätze bestimmten Nicht-adiabatizitäts-Faktoren gravierend unterscheiden. Dieses Verhalten kann auf die Ungenauigkeiten bei der Bestimmung auswertungskritischer Parameter aus den experimentellen Daten zurück geführt werden. Desweiteren zeigt sich, dass auf eindimensionalen Modellen basierende Analysen kritisch betrachtet werden müssen, wenn zweidimensionale Dynamiken, wie die Bewegung einer Domänenwand innerhalb eines Drahtes, untersucht werden.

Die im Verlauf der Arbeit erhaltenen Ergebnisse zeigen deutlich, dass die einzelnen Faktoren, die der strominduzierten Domänenwandbewegung zugrunde liegen, relativ einfach zu separieren sind. Es existieren jedoch starke Abhängigkeiten von den verwendeten Materialien. Eine genauere Bestimmung der einzelnen Materialparameter und deren Einfluss auf die einzelnen Faktoren ist hierbei der Schlüssel zur Entwicklung von effektiven spintronischen Anwendungen.

Contents

Introduction

During the last decades, the rising need for data storage devices exhibiting high storage density, fast access times, long data retention and a low power consumption inspired research on new materials and novel memory concepts [PHT08; Cow+07; Xu+08; Pav+97]. Amongst other approaches the magnetic hard disk drive [MFC06] is probably the best known data storage device. Its basic concept is the interpretation of information (bits 0 and 1) encoded in magnetic domains whose magnetization is pointing in either the left/right or up/down direction. The information is read and written using read/write heads, which are mounted on cantilever arms moving above the spinning magnetic disks. Based on the same storage concept, the MRAM and racetrack memory technology introduced novel mechanisms of manipulating the magnetic domains and especially the domain walls using electric currents, which are directly injected into the magnetic material. Hereby, the access time and power consumption could be drastically reduced since no mechanical components are required. Furthermore, the virtually unlimited endurance and data retention is kept for which the magnetic hard disk drive is well known.

This opened a new field of research, called spintronics, focusing on the interaction of spin polarized currents with magnetic domains and especially their interaction with domain walls separating the domains from each other. For applications, a number of domain walls need to be shifted at the same time by the same distance in order to keep the size of the domains and therefore the stored information. However, this turned out to be experimentally challenging since several mechanisms such as Joule heating, Oersted field effects and spin torque are involved in the current-induced domain wall motion.

Until now, two main spin torques, the adiabatic [Ber78] and non-adiabatic [ZL04; Thi+05] spin torque, acting on the domain walls have been theoretically and experimentally identified allowing for an efficient manipulation of the magnetization on the nanoscale. In experiments a strong dependence of these torques on the material composition and the magnetization configuration (in-plane or out-of-plane) has been found. First results on in-plane magnetized nanostructures exhibiting wide and complex domain wall structures revealed current-induced domain wall motion requiring large critical current densities ($> 1 \cdot 10^{12}$ A/m^2) [Klä+05; Hey+09], which is accompanied by Joule heating effects. Thus the interest shifted to out-of-plane magnetized materials for which large non-adiabatic contributions due to narrow domain walls were predicted. These non-adiabatic effects are expected to significantly lower the necessary current densities and should lead to higher domain wall velocities. For a quantitative comparison of the experiments the dimensionless non-adiabaticity parameter β was introduced being directly proportional to the domain wall velocity. Nevertheless, a vast variety of different and partly contradicting values has been found, highlighting the importance of detailed and fundamental studies of the mechanisms involved in current-induced domain wall motion and their dependence on the material compositions.

Besides Joule heating effects, the local injection of a charge current into nanowire structures also leads to the creation of an concentric magnetic field (Biot-Savart-law), the Oersted field, which is commonly used to manipulate the local magnetization [Ilg+08; You08] and nucleate domain walls [Koy+11; Ued+11; Koy+08; NIA11; Fuk+10; Tan+11; Chi+10; Ohs+11]. However, on the nanoscale, high currents are needed to create sufficiently large magnetic fields. These injected current densities are drastically increasing when the wire dimensions are further reduced thus causing unwanted Joule heating effects.

In this thesis, measurements for the characterization of different magnetic materials suitable for spintronic applications are presented. Furthermore, new methods for separating the contribution of spin torque, Oersted field and Joule heating effects to the current-induced domain wall dynamics are introduced. Finally, the non-adiabaticity parameter β is determined in various systems.

The last part of this thesis deals with experiments using low current densities to significantly lower the effects of Joule heating. At room temperature, the investigation of thermally activated magnetization dynamics allows to test the validity and robustness of two independent approaches to extract the non-adiabaticity parameter β at the same time on one sample.

The structure of this thesis is as follows:

Chapter 1 gives a general introduction of the theory behind ferromagnetism focusing on the interaction of spin polarized currents with the magnetization. Special emphasis is put on the spin torque terms and the extraction of the non-adiabaticity parameter β. Finally, magnetoresistance effects will be discussed used to characterize the magnetic materials.

Chapter 2 contains a detailed description of the cryogenic setup, the 3D-vector magnet system and the electrical setup, which have been developed within the framework of this thesis. This chapter is concluded by a description of the sample holder, which was specially designed for the injection of current pulse with widths in the nanosecond regime.

Chapter 3 briefly introduces the sample fabrication methods. Here, the focus is put on the patterning processes of magnetic materials.

Chapter 4 deals with the characterization of magnetic materials suitable for spintronic applications. A general overview of the material properties and results of magnetoresistance measurements to determine the magnetization configurations (in-plane or out-of-plane) are included in this chapter.

Chapter 5 focuses on the actual experimental results on current-induced domain wall dynamics. Besides a new approach for separating the contributions of spin torque, Oersted field and Joule heating effects on current-induced domain wall motion, an experiment about thermally activated domain wall motion is presented. The direct comparison of the β values determined allows a validation of the used experimental and theoretical approaches and to test their robustness.

In **Chapter 6** the main results of this thesis are summarized. An outlook on future experiments and challenges concludes this chapter.

The **Appendices** contain technical drawings of the instrumentation and a list of publications since most of the experiments performed during this work have been published in scientific journals. References to these publications are inserted wherever appropriate.

1

Theoretical Background

This chapter focuses on the theory of the physical mechanisms underlying current-induced domain wall dynamics, which is the focus of the experiments performed in this work. We start by providing a general introduction about ferromagnetism and the various models used to describe it.

A one dimensional model is introduced, which is commonly used to describe magnetization dynamics. The main part of this theoretical introduction is dedicated to the dynamics of ferromagnetic magnetization configurations. In particular, the influence of the electric current and the interaction between conduction electrons and localized electrons, the spin torque, will be explained in detail.

At last, magnetoresistance effects are introduced. We will describe how the magnetoresistance response of the system can be used to locally probe the magnetization dynamics.

1.1 Ferromagnetism

In the early 6th century BC, Thales of Miletus discovered an attractive force between lodestone (Magnetite) and iron, which is the earliest reference about ferromagnetism [TGS02]. Since then, many inventions based on this discovery followed, e.g. the compass (10th century AD) and electric motors. Another important application of highest scientific and economic interest is magnetic data storage (Nobel Price 2007).

After the development of classical electromagnetism, ferromagnetism was thought to arise from the magnetic dipole-dipole interaction. The energy of two magnetic dipoles using typical values ($\mu_1 = \mu_2 = 1\,\mu_\mathrm{B}$ and $\mathrm{r} = 2\,\text{Å}$) is $\mathrm{E} = 2.1 \cdot 10^{-24}\,\mathrm{J}$ and its corresponding temperature far below $1\,\mathrm{K}$. Since the ordering temperatures of typical ferromagnetic materials far exceed this temperature, the dipole-dipole interactions can not be the driving mechanism for ferromagnetism. Indeed, an adequate description and explanation of the ferromagnetism has been found in the last decades throughout the development of the quantum mechanical formalism.

Ferromagnetism is characterized by the existence of spontaneous magnetization at zero applied magnetic field below a certain temperature (Curie Temperature). The atomic spins try to align with one another through an exchange interaction based on the quantum-mechanical requirements for the symmetry of the wavefunctions and the Pauli exclusion principle. In the following two sections an introduction to this exchange interaction and a detailed band model describing a non-local mechanism are presented. The latter model has proven to be reliable in the case of the itinerant ferromagnetic materials such as cobalt, nickel and iron [Get08].

1.1.1 Exchange Interaction

The understanding of ferromagnetic interaction in the solid state can be provided by a simple model based on a two electron system with positions at $\mathbf{r}_1$ and $\mathbf{r}_2$. The total wave function is a product of the single electron states $\psi_\mathrm{a}(\mathbf{r}_1)$ and $\psi_\mathrm{b}(\mathbf{r}_2)$. Since Fermi particles are considered, the Pauli principle must be fulfilled, which means that an antisymmetric wave function is required. This can be realized either in the case of a symmetric spatial part and an antisymmetric spin part $\chi_{\uparrow\downarrow}$ or by the combination of an antisymmetric spatial part together with a symmetric spin part $\chi_{\uparrow\uparrow}$.

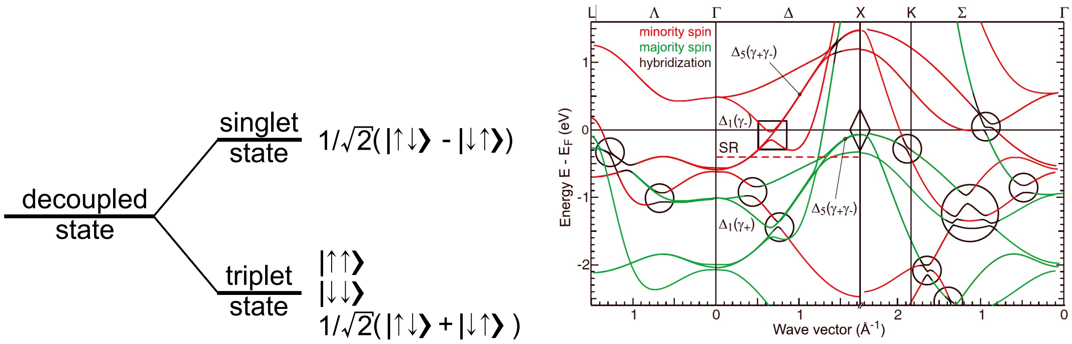

(a) (b)

Figure 1.1: (a) In the case of a ferromagnetic configuration the triplet state is energetically favorable. (b) Calculation of a spin-polarized band structure of fcc cobalt. The majority (colored green), minority (colored red) spin bands and the hybridization points are shown. (from Ref. [Pic+08])

The first combination leads to a singlet state Ψ_S with a total spin S=0, while the second case corresponds to a triplet state Ψ_T with a total spin S=1. The total wave functions are written as:

$$\Psi_S = \frac{1}{\sqrt{2}}(\psi_a(\mathbf{r}_1)\psi_b(\mathbf{r}_2) + \psi_a(\mathbf{r}_2)\psi_b(\mathbf{r}_1)) \cdot \chi_{\uparrow\downarrow}, \tag{1.1}$$

$$\Psi_T = \frac{1}{\sqrt{2}}(\psi_a(\mathbf{r}_1)\psi_b(\mathbf{r}_2) - \psi_a(\mathbf{r}_2)\psi_b(\mathbf{r}_1)) \cdot \chi_{\uparrow\uparrow}. \tag{1.2}$$

The corresponding energies of both states are:

$$E_S = \int \Psi_S^* \mathcal{H} \Psi_S dV_1 dV_2 \text{ and } E_T = \int \Psi_T^* \mathcal{H} \Psi_T dV_1 dV_2. \tag{1.3}$$

The effective Hamiltonian is given by:

$$\mathcal{H} = \frac{1}{4}(E_S + 3E_T) - (E_S - E_T)\mathbf{S}_1\mathbf{S}_2. \tag{1.4}$$

Assuming normalized spin parts of both wave functions ($\mathbf{S}^2 = 1$), the values $\mathbf{S}_1\mathbf{S}_2 = -3/4$ (singlet state) and $\mathbf{S}_1\mathbf{S}_2 = 1/4$ (triplet state) are obtained using the following equation:

$$\mathbf{S}_1\mathbf{S}_2 == \frac{1}{2}S(S+1) - \frac{1}{2}\sum_i S_i(S_i+1) \text{ with } S_1 = S_2 = \frac{1}{2} \tag{1.5}$$

Furthermore, introducing the exchange constant J, which is defined as:

$$\mathrm{J} = \frac{\mathrm{E_S} - \mathrm{E_T}}{2}, \tag{1.6}$$

the spin dependent part of the effective Hamiltonian can be rewritten as:

$$\mathcal{H}_{\mathrm{spin}} = -2\mathrm{J}\mathbf{S}_1\mathbf{S}_2. \tag{1.7}$$

In the case of $\mathrm{J} > 0$ the triplet state is energetically favorable ($\mathrm{E_S} > \mathrm{E_T}$; see Fig. 1.1(a)) leading to a parallel alignment of the spins (ferromagnet), while $\mathrm{J} < 0$ leads to a preferential singlet state ($\mathrm{E_T} > \mathrm{E_S}$) with antiparallel alignment of the spins (antiferromagnet).

In general, more than two electrons are present requiring the extension of the model to a many-body problem. Therefore, a general Hamiltonian can be introduced:

$$\mathcal{H} = -\sum_{\mathrm{ij}} \mathrm{J_{ij}}\mathbf{S}_\mathrm{i}\mathbf{S}_\mathrm{j}. \tag{1.8}$$

Here, $\mathrm{J_{ij}}$ is the exchange constant between spin i and spin j (in case of nearest neighbor spins: $\mathrm{J_{ij}} = \mathrm{J}$; otherwise: $\mathrm{J_{ij}} = 0$).

Furthermore, not only direct exchange occurs, e.g. in ionic solids a superexchange is present: The exchange interaction between non-neighboring magnetic ions is mediated via non-magnetic ions located in-between. Another important indirect exchange is the RKKY interaction (RKKY: Ruderman, Kittel, Kasuya and Yosida), which is present in metals with localized magnetic moments. The coupling is mediated by the conduction electrons and the distant-dependent exchange integral ($\mathrm{J_{RKKY}}$) shows an oscillatory behavior with changing sign, thus leading to either ferromagnetic or antiferromagnetic behavior. A more detailed treatment of direct and indirect exchange interaction can be found in Ref. [Get08] and Ref. [Aha00].

1.1.2 Band Model

The previously introduced model based on localized magnetic moments turns out to be insufficient to describe the magnetic moments and the temperature behavior (especially the Curie temperature $\mathrm{T_C}$) of the classical ferromagnets (Co, Ni and Fe). The

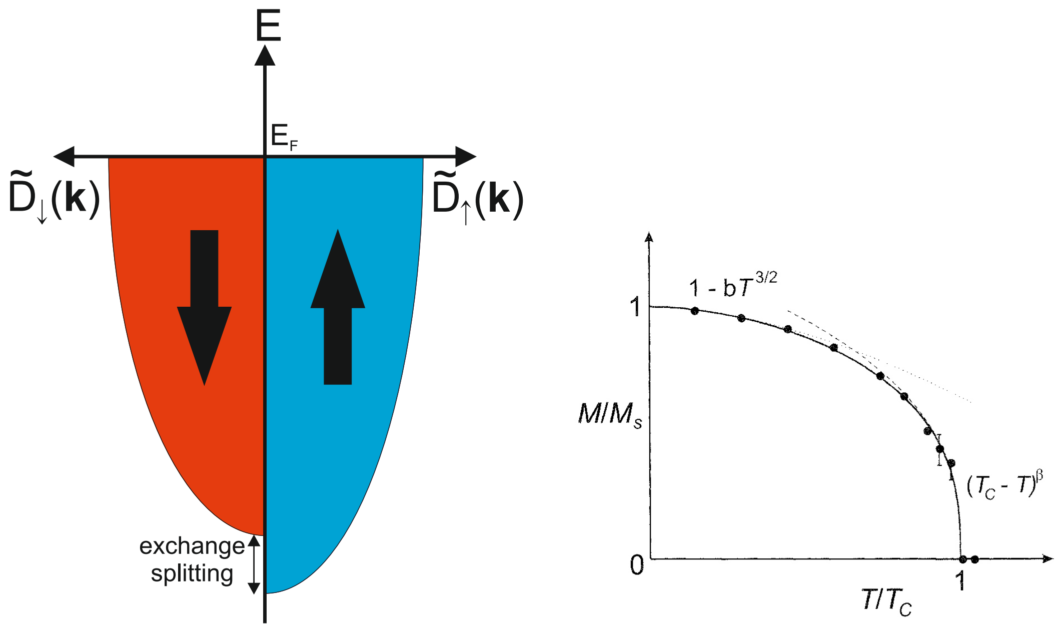

(a) (b)

Figure 1.2: (a) Schematic of the spin dependent band model assuming free electrons with a parabolic dispersion relation. The exchange splitting IR due to the recess of one spin kind is indicated. (b) Magnetization M of a ferromagnet divided by its saturation magnetization $\mathrm{M_S}$ as a function of the reduced temperature $\mathrm{T/T_C}$. The low temperature regime can be described by the Bloch-$\mathrm{T}^{\frac{3}{2}}$ law, whilst the regime close to $\mathrm{T_C}$ is described by $(\mathrm{T_C} - \mathrm{T})^{\beta}$ with β being a critical exponent.(from Ref. [Get08])

previous assumption of a simple direct exchange interaction between localized moments does not hold in case of these band ferromagnets, which are characterized by energy bands instead of discrete energy states (see Fig. 1.1(b)). The following band model developed by Stoner introduces the Stoner-criterion as a sufficient condition for ferromagnetism:

$$\mathrm{I\tilde{D}(E_F)} > 1, \tag{1.9}$$

with the Stoner parameter I and the density of states per atom and type of spin $\mathrm{\tilde{D}(E_F)}$ at the Fermi energy $\mathrm{E_F}$. Its derivation follows next.

To deduce this criterion two spin subbands for spin up (↑) and spin down (↓) electrons and their corresponding energies are introduced:

$$\mathrm{E}_{\uparrow}(\mathbf{k}) = \mathrm{E}(\mathbf{k}) - \mathrm{I}\frac{\mathrm{n}_{\uparrow}}{\mathrm{N}}, \tag{1.10}$$

$$\mathrm{E}_{\downarrow}(\mathbf{k}) = \mathrm{E}(\mathbf{k}) - \mathrm{I}\frac{\mathrm{n}_{\downarrow}}{\mathrm{N}}, \tag{1.11}$$

with $\mathrm{n}_{\uparrow}$ and $\mathrm{n}_{\downarrow}$ the number of spin up and spin down electrons, respectively. The number of total electrons is $\mathrm{N} = \mathrm{n}_{\uparrow} + \mathrm{n}_{\downarrow}$ and $\mathrm{E}(\mathbf{k})$ is the energy in case of a normal (non-magnetic) band. Furthermore, the Stoner-parameter I describes the energy reduction due to the electron interaction. Next, we define a relative excess of one kind of spin

$$\mathrm{R} = \frac{\mathrm{n}_{\uparrow} - \mathrm{n}_{\downarrow}}{\mathrm{N}}. \tag{1.12}$$

Using this relative excess R the Eqs. 1.10 and 1.11 can be rewritten as:

$$\mathrm{E}_{\uparrow}(\mathbf{k}) = \tilde{\mathrm{E}}(\mathbf{k}) - \frac{1}{2}\mathrm{IR}, \tag{1.13}$$

$$\mathrm{E}_{\downarrow}(\mathbf{k}) = \tilde{\mathrm{E}}(\mathbf{k}) + \frac{1}{2}\mathrm{IR}, \tag{1.14}$$

with $\tilde{\mathrm{E}}(\mathbf{k}) = \mathrm{E}(\mathbf{k}) - \mathrm{I}(\mathrm{n}_{\uparrow} + \mathrm{n}_{\downarrow})/2\mathrm{N}$. It can be seen that the splitting of the energy bands is dependent on the relative occupation of the two spin subbands (see also Fig. 1.2(a)).

Furthermore, we can express the relative excess R using the Fermi-Dirac distribution $\mathrm{f}(\mathrm{E}_{\mathrm{i}}(\mathbf{k}))$ with the energies E_{i} ($\mathrm{i} =\uparrow$ or $\downarrow$) as defined in Eqs. 1.13 and 1.14:

$$\mathrm{R} = \frac{1}{\mathrm{N}}\sum_{\mathbf{k}} \mathrm{f}(\mathrm{E}_{\uparrow}(\mathbf{k})) - \mathrm{f}(\mathrm{E}_{\downarrow}(\mathbf{k})) \tag{1.15}$$

$$= \frac{1}{\mathrm{N}}\sum_{\mathrm{k}} \frac{1}{\mathrm{e}^{\left[\tilde{\mathrm{E}}(\mathbf{k}) - \mathrm{IR}/2 - \mathrm{E}_{\mathrm{F}}\right]/\mathrm{k}_{\mathrm{B}}\mathrm{T}} + 1} - \frac{1}{\mathrm{e}^{\left[\tilde{\mathrm{E}}(\mathbf{k}) + \mathrm{IR}/2 - \mathrm{E}_{\mathrm{F}}\right]/\mathrm{k}_{\mathrm{B}}\mathrm{T}} + 1}. \tag{1.16}$$

This equation (self-consistency condition) has a non-vanishing solution for R under specific circumstances permitting a ferromagnetic ground state.

Finally, inserting the Eqs. 1.13 and 1.14 into Eq. 1.15 leads to the aforementioned Stoner-criterion (Eq. 1.9), which is independent of applied magnetic fields. The calculations for the classical ferromagnetic materials (Co, Ni, Fe) show that this criterion is fulfilled in each case.

A more detailed discussion and the temperature dependent calculations can be found in Ref. [IL09]. Important to mention is also the maximum temperature, the Curie-temperature ($\mathrm{T_C}$), at which the ferromagnetic behavior breaks down (see Fig. 1.2(b)).

1.2 Micromagnetic Formalism

The micromagnetic formalism uses a continuum approximation. The magnetization $\mathbf{M}$ and the magnetic field $\mathbf{H}$ are defined as continuous vector functions $\mathbf{M}(\mathbf{r})$ and $\mathbf{H}(\mathbf{r})$ allowing reliable predictions of structures on the nano- to micrometer scale [Get08; Aha00; Bro63]. Note, that the aforementioned models are used to describe the interaction of magnetic moments of isotropic systems, e.g. the energy levels described above are independent of their direction in space. In reality, materials often exhibit magnetic anisotropy. This anisotropy is commonly caused by magneto crystalline effects, whose influence will be discussed later. Other influences such as a demagnetization field and the Zeeman effect have also to be taken into account when describing micromagnetic systems.

In the next sections, the various magnetic energy contributions to a system are described. The most stable magnetic configuration is then given by minimizing the total energy.

1.2.1 Landau Free Energy

The sum of all energy contributions of a magnetic system can be expressed as the Landau free energy, which is under the present experimental conditions such as a constant temperature T and constant magnetic field $\mathbf{H}$ an appropriate thermodynamic potential:

$$\mathrm{G}(\mathbf{m}, \mathrm{T}) = \mathrm{U} - \mathrm{TS} - \mu_0 \mathbf{m}\mathbf{H}. \tag{1.17}$$

The normalized magnetization is $\mathbf{m} = \mathbf{M}/\mathrm{M_S}$ with the saturation magnetization $\mathrm{M_S}$. S is the entropy and μ_0 is the magnetic permeability in vacuum. The internal energy U consists of several terms, which are discussed in the following sections.

1.2.2 Exchange Energy

In the previous section the exchange interaction of next neighbor electron spins has been discussed and the energy difference has been expressed as $\mathrm{E} = -2\mathrm{J}\mathbf{S}_1\mathbf{S}_2$. Using a continuous limit the sum over all spins is replaced by an integral over the whole sample volume:

$$\mathrm{E}_{\mathrm{exchange}} = \mathrm{A}_{\mathrm{ex}} \int (\nabla \mathbf{m}(\mathbf{r}))^2 \mathrm{dV} \tag{1.18}$$

with the exchange stiffness $\mathrm{A}_{\mathrm{ex}} = (\mathrm{c}/\mathrm{a})\mathrm{JS}^2$ being directly proportional to the exchange constant J. Here, a is the lattice constant, c a parameter that depends on the lattice symmetry (cubic: c=1; bcc: c=2; fcc: c=4) and S the spin [Aha00].

1.2.3 Anisotropy Energy

As mentioned, realistic magnetic systems are anisotropic. Due to this anisotropy the spins cannot rotate in any direction by use of an infinitely small amount of energy. The contribution to the Landau free energy is:

$$\mathrm{E}_{\mathrm{anisotropy}} = \int \epsilon_{\mathrm{crys.}}(\mathbf{m}(\mathbf{r}))\mathrm{dV} + \int \epsilon_{\mathrm{surface}} \cdot (\mathbf{n} \cdot \mathbf{m})^2 \mathrm{dS} \tag{1.19}$$

consisting of a magneto crystalline anisotropy $\epsilon_{\mathrm{crys.}}(\mathbf{m}(\mathbf{r}))$ and a second term including the contributions from the surfaces/interfaces $\epsilon_{\mathrm{surface}}(\mathbf{m}(\mathbf{r}))$. Here, $\mathbf{n}$ is the surface normal and dS the integration over the sample surface.

Magnetocrystalline Anisotropy

In materials with a specific crystallographic structure, the magnetocrystalline anisotropy is one of the most important magnetic anisotropy terms. The electron orbitals are linked to the crystallographic structure. Therefore, the spin orbit interaction causes preferential directions for the spin orientation. In general, the spins will align along a well-defined crystallographic axis, the 'easy axis'. In most cases, the crystallographic axes perpendicular to the easy axes are not preferred and therefore classified as 'hard axes' (see Fig. 1.3(b)). Note, that even a whole plane might be preferred (easy plane) or shunned (hard plane).

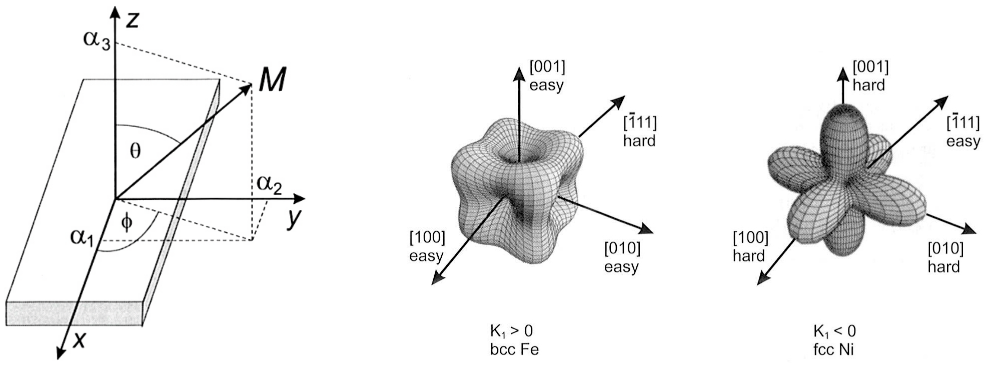

(a) (b)

Figure 1.3: (a) Schematic showing the definition of the direction cosines α_{i} and the angles θ and ϕ with respect to the magnetization **M** (from Ref. [Get08]) (b) Energy surfaces for cubic systems (bcc Fe and fcc Ni) with anisotropy constants K_1 of opposite sign. The easy and hard axes are indicated. (from Ref. [Get08])

In order to derive an expression for the corresponding energy term, the magnetization $\mathbf{m} = \mathbf{M}/\left|\mathbf{M}\right|$ is described by the direction cosines α_{i} and the angles θ and ϕ (see Fig. 1.3(a)). The corresponding energy is expressed as:

$$\epsilon_{\mathrm{crys.}}(\mathbf{m}(\mathbf{r})) = \mathrm{E}_0 + \sum_{\mathrm{ij}} \mathrm{b}_{\mathrm{ij}}\alpha_{\mathrm{i}}\alpha_{\mathrm{j}} + \sum_{\mathrm{ijkl}} \alpha_{\mathrm{i}}\alpha_{\mathrm{j}}\alpha_{\mathrm{k}}\alpha_{\mathrm{l}} + \cdots . \tag{1.20}$$

As a result of symmetry considerations, the energy for a cubic system can be written as:

$$\epsilon^{\mathrm{cubic}}_{\mathrm{crys.}}(\mathbf{m}(\mathbf{r})) = \mathrm{K}_0 + \mathrm{K}_1(\alpha_1^2\alpha_2^2 + \alpha_1^2\alpha_3^2 + \alpha_2^2\alpha_3^2) + \mathrm{K}_2\alpha_1^2\alpha_2^2\alpha_3^2 + \cdots, \tag{1.21}$$

and in case of uniaxial anisotropy (along the z-direction) as:

$$\epsilon^{\mathrm{uni}}_{\mathrm{crys.}}(\mathbf{m}(\mathbf{r})) = \mathrm{K}_0 + \mathrm{K}_1\cos(2\theta) + \cdots = \mathrm{K}_0 + \mathrm{K}_1(1 - \alpha_3^2) + \cdots. \tag{1.22}$$

The coefficients K_{i} (magnetocrystalline anisotropy constants) are functions of the coefficients b_{ij}. Further expressions and calculations of more complex systems are described in Ref. [Get08] and in Ref. [Aha00].

Surface and Interface Anisotropies

In the case of confined structures such as thin films or strips, the effects from surfaces and interfaces become important. Terms with lower order in α, which are not relevant in bulk systems, have to be taken into account due to the symmetry breaking at the surface or interface. In the framework of this thesis, these additional anisotropies are most important in the case of multilayer materials, which exhibit a strong/pronounced out-of-plane magnetization configuration.

The influence of these new anisotropies can be illustrated phenomenologically by introducing an effective anisotropy constant $\mathrm{K_{eff}}$, which consists of two terms [BHB91]:

$$\mathrm{K_{eff}} = \mathrm{K_V} + 2\mathrm{K_S}/\mathrm{d}. \tag{1.23}$$

The first term describes the previously discussed volume contribution and the second one the contributions arising from the creation of two surfaces (inclusion of a factor of 2). The inverse dependence on the thickness d highlights the importance of this term in the case of thin systems. The contribution of one surface to the energy is then written as:

$$\epsilon_{\mathrm{surface}} = \frac{1}{2}\mathrm{K_S}. \tag{1.24}$$

Assuming that $\mathrm{K_S}$ favors an out-of-plane magnetization while $\mathrm{K_V}$ favors an in-plane magnetization (negative sign) the multiplication of Eq. 1.23 with the thickness d leads to the criterion:

$$\mathrm{d_c} = -\frac{2\mathrm{K_S}}{\mathrm{K_V}} \tag{1.25}$$

for the sign of the total anisotropy $\mathrm{K_{eff}}$. Thus for $\mathrm{d} < \mathrm{d_c}$ an out-of-plane magnetization, and for $\mathrm{d} > \mathrm{d_c}$ an in-plane magnetization is favored. An example for this behavior is shown in the upper left picture of Fig. 1.4 for thin Co films with variable thickness using different Pt layers showing a good agreement with this phenomenological model. Furthermore, the additional measurements in Fig. 1.4 indicate the strong dependence of the anisotropy on the non-magnetic materials used, e.g. on the (material) specific properties of the interface. As a result, an out-of-plane magnetization would occur only for Pt, Au or Ir.

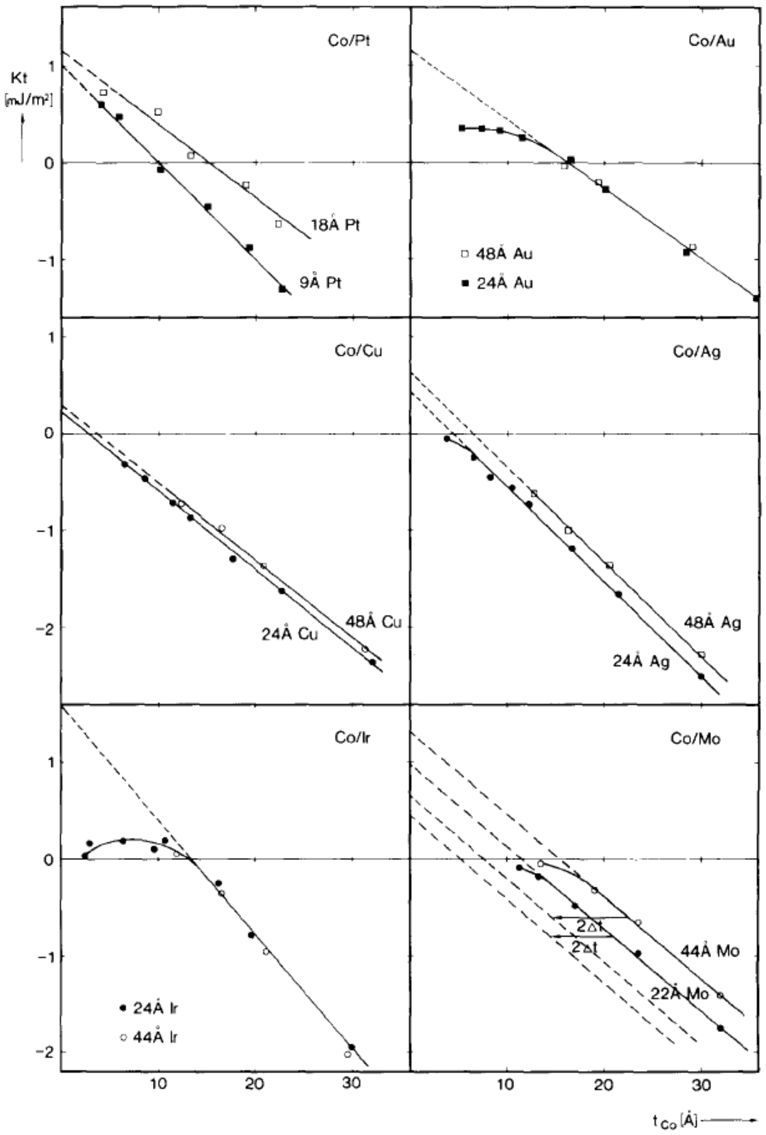

Figure 1.4: Effective anisotropy multiplied with the Co thickness t_{Co} as a function of t_{Co} for different Co/X multilayers with X=Pt, Au, Cu, Ag, Ir, Mo. (from Ref. [BHB91])

Apart from this phenomenological approach, experimental [Nak+98] and theoretical [Zho+96; Újf+96] studies have identified the electronic hybridization at the interfaces between the magnetic and non-magnetic materials as the origin for the strong out-of-plane anisotropy. Pt turns out to be the most suitable material since strong spin-orbit interactions have been reported [Nak+98].

1.2.4 Demagnetization Field Energy

A third anisotropic effect is the shape anisotropy, which becomes important for instance in the case of polycrystalline samples without preferred crystalline axes. The demagnetization field due to the generation of a stray field outside the sample leads to the creation of an easy axis defined by the geometrical shape of the magnetic structure. To gain further insight into this effect, the Maxwell equation $\nabla \mathbf{B} = 0$ with $\mathbf{B} = \mu_0(\mathbf{H} + \mathbf{M})$ needs to be considered. Outside a finite sample a stray field, which is caused by the magnetization of the sample itself, is generated. The energy cost of this stray field is expressed in terms of a demagnetization field $\mathbf{H}_{\mathrm{demag}}$ inside the sample. In the continuum formalism this energy is written as:

$$\mathrm{E}_{\mathrm{stray}} = -\frac{1}{2}\mu_0 \int \mathbf{M} \cdot \mathbf{H}_{\mathrm{demag}} \mathrm{dV}. \tag{1.26}$$

For an arbitrarily shaped object, the calculation of the demagnetization field is rather complicated [HS98]:

$$\mathrm{H}_{\mathrm{demag}} = \int_{\Omega} \frac{(\mathbf{r} - \mathbf{r}')\rho(\mathbf{r}')}{|\mathbf{r} - \mathbf{r}'|^3} \mathrm{dV} - \int_{\partial\Omega} \frac{(\mathbf{r} - \mathbf{r}')\sigma(\mathbf{r}')}{|\mathbf{r} - \mathbf{r}'|^3} \mathrm{ds} \tag{1.27}$$

with the volume charges $\rho = \nabla \mathbf{M}$ and surface charges $\sigma = \mathbf{n} \cdot \mathbf{M}$ (surface normal $\mathbf{n}$).

In the case of symmetric objects and uniform magnetic states, the demagnetization field can be written as:

$$\mathbf{H}_{\mathrm{demag}} = -\mathcal{N}\mathbf{M} \tag{1.28}$$

with the demagnetization tensor:

$$\mathcal{N} = \begin{pmatrix} N_x & 0 & 0 \\ 0 & N_y & 0 \\ 0 & 0 & N_z \end{pmatrix} \tag{1.29}$$

where the demagnetizing factors for each axes (i=x,y,z) N_{i} depend on the geometry. For example, for a sphere the demagnetizing factors are $\mathrm{N}_{\mathrm{x}} = \mathrm{N}_{\mathrm{y}} = \mathrm{N}_{\mathrm{z}} = 1/3$, while for an infinitely long cylinder (a=b, c=∞) the demagnetizing factors are $\mathrm{N}_{\mathrm{x}} = \mathrm{N}_{\mathrm{y}} = 1/2$ and $\mathrm{N}_{\mathrm{z}} = 0$.

1.2.5 Zeeman Energy

In an external magnetic field, the spins try to align along the direction of the magnetic field to minimize the energy of the system. In a continuum approach, the Zeeman energy is given by:

$$\mathrm{E}_{\mathrm{Zeeman}} = -\mu_0 \int \mathbf{M} \cdot \mathbf{H} \mathrm{dV}. \tag{1.30}$$

1.2.6 Brown's Equation

In order to find a stable magnetic configuration M_0, the Landau free energy has to be minimized:

$$\left.\frac{\partial \mathrm{G}}{\partial \mathbf{M}}\right|_{\mathrm{M}_0} = 0. \tag{1.31}$$

Excluding the temperature dependent term of the Landau free energy (see Eq. 1.17) the left side of Eq. 1.31 leads to a definition of an effective field $\mathbf{H}_{\mathrm{eff}}$ [Aha00]. A total of three coupled partial differential equations, which are known as Brown's equations, can be obtained [Bro63]:

$$\mathbf{H}_{\mathrm{eff}} = \mathbf{H}_{\mathrm{exchange}} + \mathbf{H}_{\mathrm{anisotropy}} + \mathbf{H}_{\mathrm{demag}} + \mathbf{H}_{\mathrm{Zeeman}}, \tag{1.32}$$

$$\mathbf{M} \times \mathbf{H}_{\mathrm{eff}} = 0, \tag{1.33}$$

$$\mathbf{M} \times \frac{\partial \mathbf{M}}{\partial \mathbf{n}} = 0 \tag{1.34}$$

with the surface normal $\mathbf{n}$. By defining the effective field, an iterative solution of the equations can be found for realistic problems. The convergence criterion therefore is derived from the second of Brown's equations:

$$\int |\mathbf{M} \times \mathbf{H}_{\mathrm{eff}}| \, \mathrm{dV} = 0. \tag{1.35}$$

Examples of static magnetization configurations are discussed in the following section. However, as this model can be only used for static magnetization configurations, further terms will be introduced later on in order to describe the magnetization dynamics. Extensive details can be found in Ref. [Aha00] and in Ref. [Bro63].

1.3 Static Magnetization Configurations

In confined magnetic systems on the nano- to micrometer scale, which are the focus of this work, various types of stable magnetic configurations are possible. As discussed before, many parameters (used materials and production processes, geometric dimensions, etc.) affect the strength of certain energies and therefore the preferential configuration for which the energy of the system can be minimized. For a further classification, the materials in the context of this work are split into two main groups of preferred magnetic configurations: i) in-plane magnetized materials and ii) out-of-plane magnetized materials. Furthermore, of particular interest is the transition region from one magnetic domain to an adjacent domain, which is called domain wall. Some relevant domain wall structures will be discussed, while a more detailed treatment can be found in Ref. [HS98].

1.3.1 In-plane Magnetization

An in-plane magnetic configuration is preferred for thin films in the range of a few to tens of nanometers. In this case the shape anisotropy will dominate the energy contributions and the magnetization will align along the surface of a film (in the plane) or along a wire structure. When more than one domain exist, various types of domain walls depending on the sample geometry may be formed. A simple case is the transverse domain wall, whose characteristic feature is the triangular shape as shown in Fig. 1.5(a). Another domain wall type is the vortex wall shown in Fig. 1.5(b). This rather complex structure consists of a circular alignment of the magnetization around a vortex core, whose magnetization is pointing out-of-plane. The vortex domain wall structure becomes more relevant for thick and wide sample geometries, where the dominance of the shape anisotropy over the other energy contributions is less pronounced.

1.3.2 Out-of-plane Magnetization

In section 1.2.3 the thickness dependence of the effective anisotropy energy was discussed. The result of this discussion are based on the assumption that $\mathrm{K_S}$ favors an out-of-plane magnetization and $\mathrm{K_V}$ an in-plane magnetization thus leading to a critical thickness for which materials exhibit an out-of-plane magnetization. In such cases, the surface

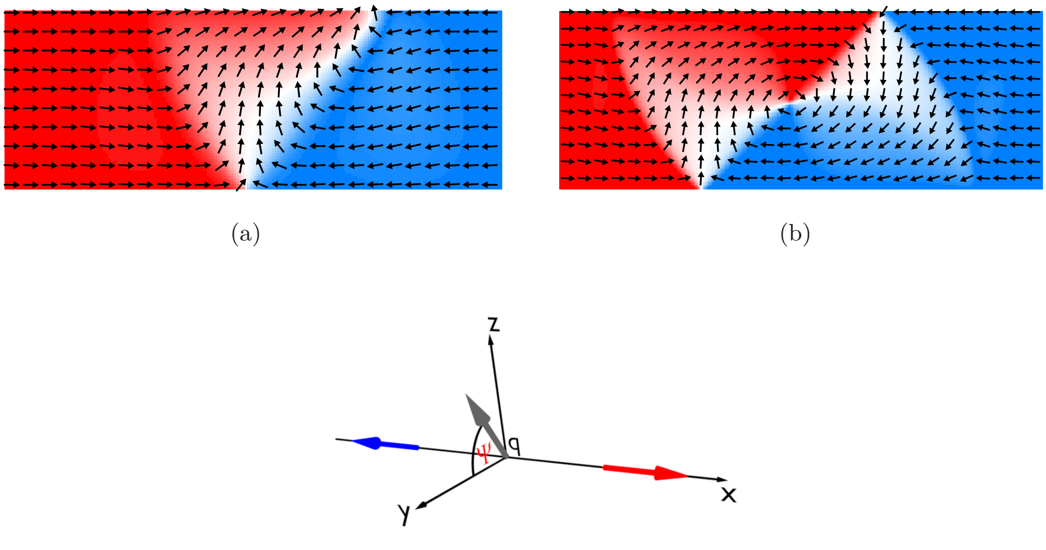

(a)

(b)

(c)

Figure 1.5: Simulation of a transverse domain wall (a) and a vortex domain wall (b) both performed using the simulation tool OOMMF [DP99]. Here, the arrows and the color code indicate the in-plane magnetization direction. (from Ref. [Möh11]) (c) Definition of the domain wall center position q and the tilt angle Ψ of the domain wall's magnetization.

anisotropy becomes the dominant contribution compared to the shape anisotropy. Especially multilayer materials exhibit such an out-of-plane magnetization since magnetic layers with thicknesses of a few Ångström are used.

Compared to in-plane magnetized structures, only simple domain wall types such as Néel or Bloch walls occur in out-of-plane magnetized materials. The Néel wall is, in analogy to the in-plane magnetization case, a structure where a rotation of the magnetization by 180° in a plane perpendicular to the domain wall plane occurs (see Fig. 1.6(a)). The Bloch wall consists of a rotation of the magnetization by 180° in the plane of the domain wall (see Fig. 1.6(b)).

The stabilization of either a Bloch or a Néel wall within a wire geometry depends on the magnetic energy difference between both domain wall types, which is:

$$\mathrm{K_d} = \frac{\mu_0 \mathrm{M_S^2}}{2}(\mathrm{N_x} - \mathrm{N_y}) \tag{1.36}$$

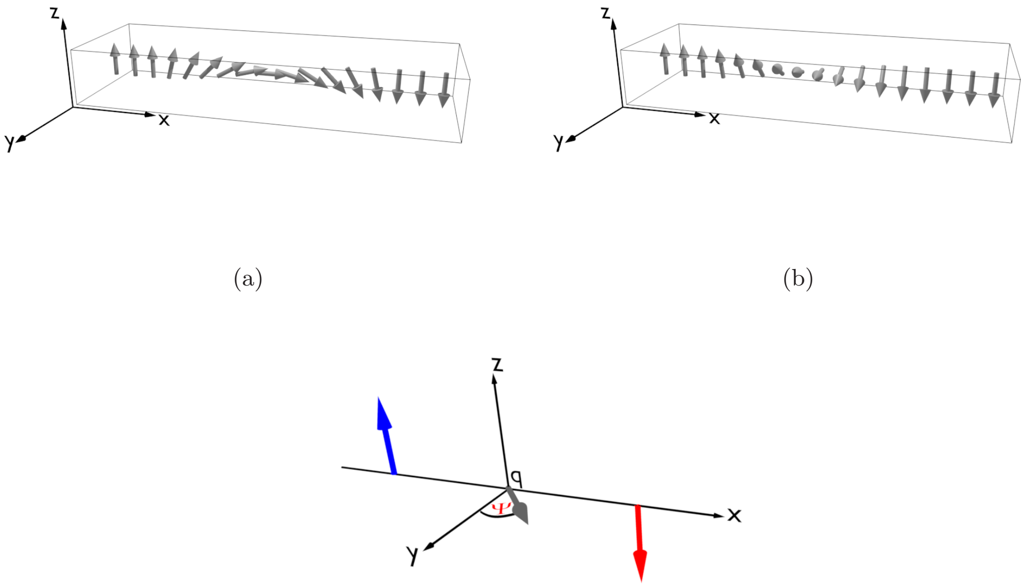

(a) (b)

(c)

Figure 1.6: Schematic of a Néel domain wall (a) and a Bloch domain wall (b). (c) Definition of the domain wall center position q and the tilt angle Ψ of the domain wall's magnetization.

with the demagnetizing factors for each axes (i=x,y,z) $\mathrm{N_i}$ depending on the geometry. The domain wall energy is given by:

$$\sigma = 4\sqrt{\mathrm{A_{ex}} \cdot \mathrm{K_{eff}}} \tag{1.37}$$

with the exchange constant $\mathrm{A_{ex}}$ (see Sec. 1.2.2) and an effective anisotropy [BMK11]:

$$\mathrm{K_{eff}} = \mathrm{K} - \mathrm{N_z}\mu_0\mathrm{M_S^2}/2 + \mathrm{K_d}\mathrm{sin}^2(\Psi). \tag{1.38}$$

Here, the first term is the anisotropy constant K, the second term arises from the shape anisotropy and the last term describes the demagnetization energy depending on the in-plane angle Ψ as defined in Fig. 1.5(c) and Fig. 1.6(c) (Bloch wall: $\Psi = 0$; Néel wall: $\Psi = \pi/2$). The sign of $\mathrm{K_d}$ depends on the dimensions of the nanowire, generally decreasing as its width and thickness decrease. In the case of a positive sign, a minimum domain wall energy is realized for $\Psi = 0$ or $\Psi = \pi$ leading to a Bloch domain wall. For a negative sign of $\mathrm{K_d}$, a Néel wall is the resulting stable magnetization configuration.

Another important parameter is the domain wall width λ (the region over which the magnetization vector varies locally), which is given by:

$$\lambda = \sqrt{\frac{\mathrm{A_{ex}}}{\mathrm{K_{eff}}}}. \tag{1.39}$$

Due to the strong dependence on the material parameters $(\mathrm{A_{ex}}, \mathrm{K_{eff}})$, domain wall widths ranging from a few nanometers in case of hard magnetic materials to more than 100 nanometers in soft magnetic materials can be achieved.

1.4 Magnetization Dynamics

In the following sections, models and equations used in the understanding of the experimental results presented in this work are introduced to describe the magnetization dynamics. More specifically, the interactions between spin polarized conduction electrons and the local magnetization, influences from external magnetic fields and thermally activated processes will be discussed.

1.4.1 Landau-Lifshitz-Gilbert Equation

Away from its equilibrium configuration, the magnetization starts to precess around an effective field $\mathbf{H}_{\mathrm{eff}}$ including the aforementioned contributions to Brown's equations. In 1935, Landau and Lifshitz [LL35] introduced an equation consisting of a precession term and another term to account for energy losses (damping):

$$\frac{\mathrm{d}\mathbf{M}}{\mathrm{dt}} = -\gamma_{\mathrm{LL}}\mathbf{M} \times \mathbf{H}_{\mathrm{eff}} - \frac{\alpha_{\mathrm{LL}}}{\mathrm{M_S}}\mathbf{M} \times (\mathbf{M} \times \mathbf{H}_{\mathrm{eff}}) \tag{1.40}$$

with the gyromagnetic ratio γ_{LL} and the Landau-Lifshitz damping parameter α_{LL}, which causes a motion of the magnetization towards the local effective field direction. A few decades later, Gilbert [Gil04] used a slightly different form:

$$\frac{\mathrm{d}\mathbf{M}}{\mathrm{dt}} = -\gamma\mathbf{M} \times \mathbf{H}_{\mathrm{eff}} - \frac{\alpha}{\mathrm{M_S}}\mathbf{M} \times \frac{\mathrm{d}\mathbf{M}}{\mathrm{dt}}, \tag{1.41}$$

which can be transformed into the the Landau-Lifshitz equation with the following substitutions:

$$\gamma_{\mathrm{LL}} = \gamma/(1+\alpha^2) \quad \text{and} \quad \alpha_{\mathrm{LL}} = \gamma\alpha/(1+\alpha^2) \tag{1.42}$$

with the Gilbert damping parameter α. Note that in both equations the magnetization vector length $|\mathbf{M}|$ does not change.

To account for current induced domain wall dynamics, two further terms are introduced into the modified Landau-Lifshitz-Gilbert equation (LLG):

$$\frac{\mathrm{d}\mathbf{M}}{\mathrm{dt}} = -\gamma\mathbf{M}\times\mathbf{H}_{\mathrm{eff}} - \frac{\alpha}{\mathrm{M_S}}\mathbf{M}\times\frac{\mathrm{d}\mathbf{M}}{\mathrm{dt}} - (\mathbf{u}\cdot\nabla)\mathbf{M} + \beta[\mathbf{M}\times(\mathbf{u}\cdot\nabla)\mathbf{M}]. \tag{1.43}$$

The additional third and fourth term describe the dynamics arising from an adiabatic spin transfer torque and a non-adiabatic spin transfer torque, respectively. The newly introduced parameters characterizing the torques are the domain wall velocity $\mathbf{u}$ and a dimensionless parameter β. The following sections aim at describing the various contributions to the domain wall motion.

Field-Induced Domain Wall Motion (Oersted Field Effects)

The manipulation of magnetization using an externally applied magnetic field, which is included in the effective field $\mathbf{H}_{\mathrm{eff}}$, can lead to the nucleation of domain walls within confined nanostructures and to their motion. Here, the domain walls will move in such a

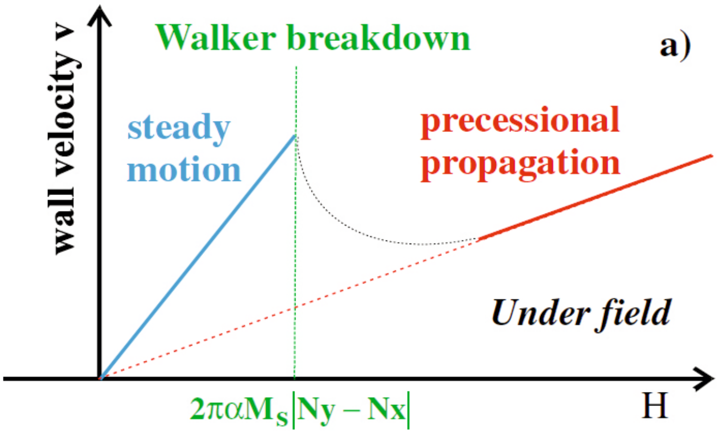

Figure 1.7: Sketch of the velocity of a Bloch domain wall as a function of an external magnetic field H. The linear regimes and the Walker breakdown field are indicated. (from Ref. [Mou+07])

way so that the Zeeman energy is minimized. Therefore, the domains with spins parallel to the external magnetic field will grow in size. If a single domain wall is present, the direction of the domain wall motion can be controlled by changing the direction of the external magnetic field. Two adjacent domain walls will move in opposite directions. For weak external magnetic fields, the domain wall velocity will increase linearly until a critical field, the Walker breakdown field H_W, is reached (see Fig. 1.7) [SW74]. Above the Walker breakdown field the domain wall structure starts to change periodically (precession of the magnetization around the effective field direction), resulting in a decreased velocity. The new domain wall structure then starts again to accelerate before a new transformation occurs.

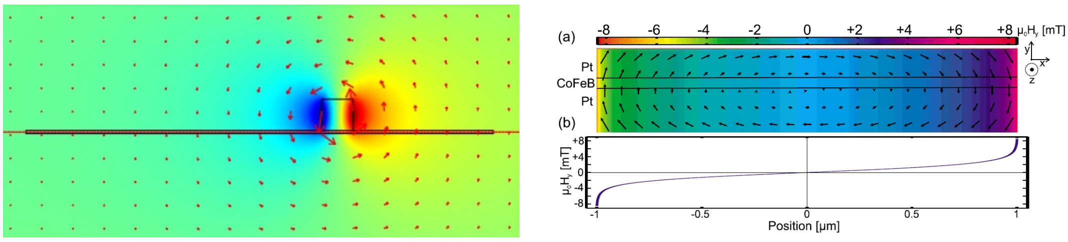

(a)

(b)

Figure 1.8: (a) Simulation of a homogeneous current density ($1 \cdot 10^{11}$ A/m^2) creating a circular magnetic field. The current density is perpendicular to the small rectangle (100 nm × 100 nm) representing a current line across a 10 nm thick wire. (b) A homogeneous current density ($1 \cdot 10^{12}$ A/m^2) flowing through a wire in -z direction creates a circular Oersted field, whose out-of-plane component H_y is plotted as a function of the lateral position x, too. (from Ref. [Bou+09])

Apart from an external applied magnetic field, a charge current passing through a wire/device creates a local concentric magnetic field (Biot-Savart-law), the Oersted field. A simulation of a local Oersted field created by a constant current through a rectangular wire is shown in Fig. 1.8(a). At the nanoscale, extremely high current densities in these additional wires are required to create Oersted fields large enough to nucleate and/or to move domain wall structures, entailing a disadvantageous scaling.

Considering the magnetic structures itself, Oersted field simulations of a perfect nanowire structures with a constant current flowing along the wire reveal that the net force on a DW should be zero, but in out-of-plane magnetized materials it can lead to local depinning of the domain wall due to an effective Oersted field at the edges of the wire (see Fig.

1.8(b)). In soft-magnetic materials with a perpendicular uniaxial anisotropy these effective Oersted fields might also induce a change in the domain structure (domain wall plane is perpendicular to the wire axis) into a domain wall aligned along the wire axis, which then can be reversibly switched due to the Oersted field effect [Bou+09].

Adiabatic Torque

Beyond the manipulation of magnetization using magnetic fields, there is another approach based on the interaction of spin polarized conduction electrons with the local magnetization, which was first proposed by L. Berger more than 30 years ago [Ber78]. If the local magnetization changes slowly (e.g. the domain wall is sufficiently wide), the conduction electron spins can adiabatically follow the local magnetization. As the total spin is conserved in this process, an angular momentum d**S** is transferred to the magnetization and the domain wall will move along the electron flow direction [Thi+04; XZS06; TK04; ZL04].

For an injected current **I** with spin polarization P, the total change of angular momentum during the time dt is given by

$$\mathrm{d}\mathbf{S} = -\mathbf{I}\frac{\hbar \mathrm{P}}{\mathrm{e}}\frac{\nabla_\mathrm{e}\mathbf{M}}{\mathrm{M_S}}\mathrm{dt}. \tag{1.44}$$

∇_e denotes the derivative of the magnetization in the direction of the electron flow. Together with the cross-sectional area A of the wire, one can calculate the angular momentum per volume:

$$\mathrm{d}\mathbf{M} = \frac{1}{2}\mathrm{g}\mu_\mathrm{B}\frac{\mathrm{d}\mathbf{S}}{\hbar \mathrm{Adx}} = -\mathbf{J}\frac{\mathrm{g}\mu_\mathrm{B}\mathrm{P}}{2\mathrm{eM_S}}\nabla_\mathrm{e}\mathbf{M}\mathrm{dt} \tag{1.45}$$

with the Bohr magneton μ_B, the Landé factor g, the current spin polarization P, the saturation magnetization $\mathrm{M_S}$ and the current density **J**=**I**/A. Allowing an arbitrary direction of the electron flow, the adiabatic spin torque introduced in Eq. 1.43 is written as:

$$\frac{\mathrm{d}\mathbf{M}}{\mathrm{dt}} = \boldsymbol{\tau}_\mathrm{ad.} = -(\mathbf{u}\cdot\nabla)\mathbf{M} \tag{1.46}$$

with the wall velocity **u** defined as:

$$\mathbf{u} = \frac{\mathrm{Pg}\mu_\mathrm{B}}{2\mathrm{eM_S}}\cdot\mathbf{J}. \tag{1.47}$$

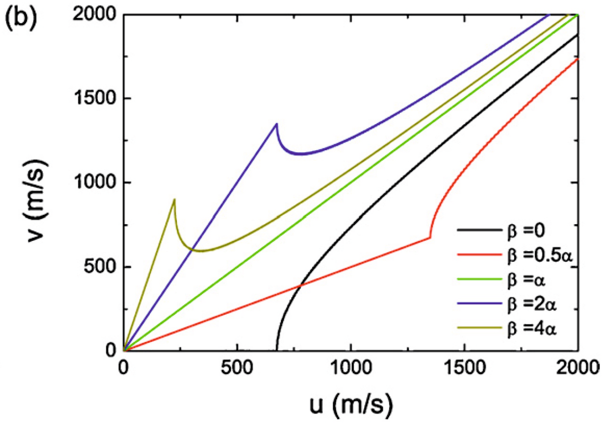

Figure 1.9: Sketch of the velocity of a Bloch domain wall as a function of u for different ratios between the non-adiabaticity parameter β and the Gilbert damping constant α. (from Ref. [BMK11])

The model predicts a critical current density J_c for which a domain wall motion sets in as indicated in Fig. 1.9 for the pure adiabatic case ($\beta = 0$). For current densities below J_c the domain wall is displaced by a few nanometers and relaxes back to its original position when the current is turned off [Thi+04; SW74].

Non-adiabatic Torque

To circumvent high critical current densities ($> 1 \cdot 10^{12}$ A/m^2) necessary for domain wall motion in materials with dominant adiabatic spin torque (e.g. Permalloy), materials with narrow domain wall structures with predicted strong contributions from non-adiabatic effects, are the focus of current research. First introduced by Zhang *et al.* [ZL04] and Thiaville *et al.* [Thi+05] describing spin relaxation processes (SR) [Nak+10; ZL04; Thi+05; Tat+06; TK04] and a linear momentum transfer (NA) [XZS06; VV07; WV04; TK04; TKS08b] the non-adiabatic effects enable high domain velocities at much smaller current densities ($<< 1 \cdot 10^{12}$ A/m^2).

The first process, spin relaxation (SR), arises from spin-flip scattering due to spin-orbit interaction, which can occur in either wide or narrow domain walls. Here, the strength of the non-adiabatic torque expressed by $\beta_{\rm SR}$ is directly linked to the exchange energy $J_{\rm ex}$ and the spin relaxation time $\tau_{\rm sf}$ [ZL04; Thi+05]:

$$\beta_{\rm SR} = \hbar / J_{\rm ex} \tau_{\rm sf}. \tag{1.48}$$

Theory predicts $\beta_{\rm SR}$ to be of the order of the Gilbert damping constant α [TF97].

The second non-adiabatic effect, linear momentum transfer (NA), is expected to become important and dominant in the case of narrow domain walls (large magnetization gradients) where a domain wall can be regarded as a rigid object so that the conduction electrons will be reflected. This leads to a domain wall motion along the direction of the conduction electron flow. The torque by the electrons on the domain wall is directly proportional to the domain wall resistivity ρ_{DW} [LZ97; TF97]. The non-adiabaticity parameter in the case of linear momentum transfer is given by:

$$\beta_{\mathrm{NA}} = \frac{\mathrm{e}^2 \mathrm{n} \rho_{\mathrm{DW}} \lambda^2}{\mathrm{P} \hbar} \tag{1.49}$$

with the electron density n, the domain wall width λ and the spin polarization of the current P.

The dimensionless parameter β introduced in the LLG includes both non-adiabatic effects:

$$\beta = \beta_{\mathrm{SR}} + \beta_{\mathrm{NA}}. \tag{1.50}$$

This non-adiabatic torque defined by:

$$\boldsymbol{\tau}_{\mathrm{non-ad.}} = \beta [\mathbf{M} \times (\mathbf{u} \cdot \nabla) \mathbf{M}] \tag{1.51}$$

moves a domain wall at much lower current densities compared to the pure adiabatic case (see Fig. 1.9). The final velocity now scales below the Walker breakdown as follows:

$$\mathbf{v} = \frac{\beta}{\alpha} \mathbf{u} \tag{1.52}$$

with the Gilbert damping constant α [ZL04; Tat+06; Thi+04]. In case of $\beta = \alpha$ no Walker breakdown occurs and the domain wall will move with velocity $\mathbf{u}$ (green solid line in Fig. 1.9).

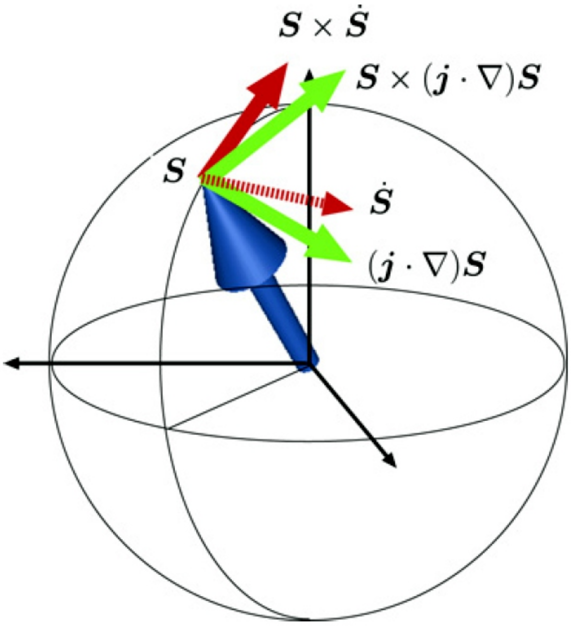

Figure 1.10: Direction of the torques acting on a localized spin **S**: damping torque $\mathbf{S} \times \dot{\mathbf{S}}$, adiabatic torque $(\mathbf{j} \cdot \nabla)\mathbf{S}$ and non-adiabatic torque $\mathbf{S} \times (\mathbf{j} \cdot \nabla)\mathbf{S}$. (from Ref. [TKS08a])

1.4.2 Description using a One-Dimensional Model

For a rigid domain wall profile, a one-dimensional model (1D-model) is appropriate. In this model, the domain wall dynamics can be described by a set of two parameters, the domain wall center position q and an effective out-of-plane angle Ψ, which are indicated in Fig. 1.5(c) and Fig. 1.6(c). The LLG (Eq. 1.43) can then be reduced to [Thi+05]:

$$\dot{\Psi} + \frac{\alpha}{\lambda}\dot{\mathrm{q}} = \gamma\mu_0\mathrm{H} + \beta\frac{\mathrm{u}}{\lambda} - \frac{\gamma}{2\mathrm{M_S}}\frac{\partial \mathrm{V_{pin}}}{\partial \mathrm{q}} \tag{1.53}$$

$$\frac{\dot{\mathrm{q}}}{\lambda} - \alpha\dot{\Psi} = \frac{\gamma\mu_0\mathrm{H_k}}{2}\sin(2\Psi) + \frac{\mathrm{u}}{\lambda} \tag{1.54}$$

with the gyromagnetic ratio $\gamma = \mathrm{g}\mu_\mathrm{B}/\hbar$, the restoring field for the transverse orientation $\mathrm{H_k}$, the external magnetic field H along the easy axis, the domain wall width λ, domain wall velocity u and the pinning potential $\mathrm{V_{pin}}(\mathrm{q}, \Psi)$. The various directions of the torques acting are illustrated in Fig. 1.10. Assuming the pure adiabatic case ($\beta = 0$), the stationary solutions, solving $\dot{\Psi} = 0$, $\dot{\mathrm{q}} = 0$ and $\sin(2\Psi) = 1$, allow one to deduce the aforementioned critical current density for which the domain wall motion sets in:

$$\mathrm{J_c} = \frac{\mathrm{eS^2}}{\mathrm{Pa^3}\hbar}\mathrm{K_\perp}\lambda \tag{1.55}$$

with the current spin polarization P, the lattice constant a and the magnitude of the local spin S. The resulting domain wall velocity for the pure adiabatic case is [Thi+04; Tat+06]:

$$\mathrm{u_c} = \gamma\mu_0\mathrm{H_k}\lambda/2. \tag{1.56}$$

However, the domain wall dynamics are strongly modified when the non-adiabatic torque is taken into account. From Eq. 1.53 it can be seen that the non-adiabatic torque enters the equation with an analytical form similar to an effective field reducing the necessary critical current density for domain wall motion. This field-like behavior is helpful to determine the non-adiabaticity parameter β from experiments (details see Sec. 1.4.5).

1.4.3 Pinning Regimes

In the presence of pinning, the calculation of the critical current density is even more complex. Three different regimes, depending on the pinning strength, can be identified. The following overview is based on the detailed study by Tatara *et al.* [Tat+06].

Weak Pinning Regime

The weak pinning regime considers low current densities, which do not affect the angle Ψ, but allows one to describe the dynamics by the domain wall center position q. Furthermore, the weak pinning regime can be divided into two sub-regimes: In regime Ia) β is small and domain wall depinning occurs throughout the adiabatic spin torque. The kinetic energy therefore is supplied by the spin transfer. In regime Ib) β governs the depinning process lowering the necessary critical current density $\mathrm{J_c} \propto \mathrm{V_0}/\beta$ with the pinning potential strength per spin $\mathrm{V_0}$.

Intermediate Pinning Regime

In this regime, the depinning is governed by the adiabatic torque resulting in a constant, but modified, critical current density due to β. Theory predicts therefore a 0.7 to 0.8 times smaller $\mathrm{J_c}$ (Eq. 1.55), but being independent of the pinning potential itself.

Strong Pinning Regime

The third pinning regime is one with so strong pinning that a domain wall stays in the potential well even for $\mathrm{J} = \mathrm{J_c}$. Only the domain wall angle Ψ starts to oscillate. In general, the dynamics in this regime are largely independent of β.

1.4.4 Thermal Excitation

So far, thermally activated processes have not been taken into account. The inclusion of thermal effects, such as Joule heating due to current densities exceeding $1 \cdot 10^{12}\,\mathrm{A/m^2}$, is relevant when analyzing real experiments. Here, the injection of current may lead to local temperature increases up to hundreds of Kelvin [Bou+08; Bur+10] depending on the wire structure, material composition and the possibility of heat dissipation [YSJ06; YH07] into the surrounding environment. In general, thermal activation is treated by adding a stochastic Gaussian distributed magnetic field [Bro63] into the Landau-Lifshitz-Gilbert equation. Thermal excitation has been used to explain different phenomena at high current densities, such as decreasing domain wall depinning fields, spontaneous nucleation and domain wall motion independent of the direction of the conduction electron flow.

Another approach to account for thermal effects has been put forward by Duine *et al.* [DNM07] adding stochastic Gaussian distributed forces η_Ψ and η_q to account for thermal effects. The extended equations of the 1D-model are then given by:

$$\dot{\Psi} + \frac{\alpha}{\lambda}\dot{\mathrm{q}} = -\frac{\gamma}{2\mathrm{M_S}}\frac{\delta \mathrm{V_{eff}}}{\delta \mathrm{q}} + \eta_\Psi \tag{1.57}$$

$$\frac{\dot{\mathrm{q}}}{\lambda} - \alpha\dot{\Psi} = -\frac{\gamma}{2\mathrm{M_S}\lambda}\frac{\delta \mathrm{V_{eff}}}{\delta \Psi} + \eta_\mathrm{q} \tag{1.58}$$

including an effective potential

$$\mathrm{V_{eff}} = \mu_0 \mathrm{H_K M_S} \lambda \sin^2\Psi + \frac{2\mathrm{M_S}}{\gamma}\mathrm{u}\Psi - 2\mathrm{M_S q}(\mu_0 \mathrm{H} + \frac{\beta \mathrm{u}}{\lambda\gamma}) + \mathrm{V_{pin}}(\mathrm{q}, \Psi) \tag{1.59}$$

summarizing the terms of the restoring field for the transverse orientation $\mathrm{H_K}$, the adiabatic and non-adiabatic torques, the external magnetic field H and the pinning potential $\mathrm{V_{pin}}(\mathrm{q}, \Psi)$. One can note that the effective potential $\mathrm{V_{eff}}$ is changed by the adiabatic torque only along the Ψ direction, whereas the non-adiabatic torques causes changes along the q direction as does the magnetic field H. This current-field equivalence is the key mechanism to determine the non-adiabaticity parameter β.

1.4.5 Extraction of the Non-adiabatic Spin Torque

The determination of the extent to which the adiabatic torque, the non-adiabatic torque or the Oersted field contribute to the domain wall displacement is one of the key challenges of modern spintronic research. Many experimental techniques have been developed to characterize current-induced domain wall dynamics. A few examples are presented in the experimental chapter of this work focusing on the extraction and separation of the various mechanisms.

The next sections are dedicated to aid the understanding of the theory behind two independent approaches to extract the non-adiabaticity parameter β, which acts as an indicator for efficient current-induced domain wall dynamics: i) the current-field equivalence and ii) a survey of the influence of the electric current on a thermally activated motion of the domain wall across an energy barrier separating two metastable pinning states. The second is referred to as Arrhenius law approach.

Current-Field Equivalence

The first approach can be deduced directly from the equations of motion of the 1D-model (Eq. 1.53 and 1.54). As highlighted before, the non-adiabatic torque enters as an effective field $\mathrm{H_{eff}}$, which is directly proportional to the current density J [Bou+08; Vir+05]:

$$\mu_0 \mathrm{H_{eff}} = \beta \frac{\mathrm{u}}{\lambda\gamma} = \epsilon \mathrm{J}. \tag{1.60}$$

using the efficiency ϵ defined as:

$$\epsilon = \beta \frac{\mathrm{P}\hbar}{2\mathrm{eM_S}\lambda}. \tag{1.61}$$

A systematic study of the interaction of applied fields and injected currents e.g. during DW depinning processes can now give information about the efficiency and allow for the evaluation of the non-adiabaticity parameter β.

Arrhenius Law Approach

The second approach relies on the assumption that a rigid domain wall, which is pinned at a defect, can be described as a quasi particle moving in a one dimensional potential landscape. For this specific work, a one dimensional landscape is considered with two metastable potential wells, which are separated by a current density (J) and magnetic field (H) dependent energy barrier $\epsilon(\mathrm{J},\mathrm{H})$ (see Fig. 1.11). The thermally activated domain wall depinning from one metastable pinning state to the other can be described by an Arrhenius law [HTB90]. The time τ_S for which a domain wall stays in state S is then given by:

$$\frac{1}{\tau_\mathrm{S}} = \frac{1}{\tau_{0,\mathrm{S}}} \exp\left[-\frac{\epsilon(\mathrm{J},\mathrm{H})}{\mathrm{k_B T}}\right] \tag{1.62}$$

with the attempt frequency $1/\tau_{0,S}$, temperature T and Boltzmann constant $\mathrm{k_B}$. In the presence of a charged current and magnetic field, the energy barrier can be described as:

$$\epsilon_\mathrm{S}(\mathrm{J},\mathrm{H}) = \epsilon_{0,\mathrm{S}}(\mathrm{H}) - \sigma\mathrm{J} - \eta\mathrm{J}^2. \tag{1.63}$$

Here, $\epsilon_{0,\mathrm{S}}(\mathrm{H})$ denotes the energy barrier height in the absence of current for an external magnetic field H. The third term describes the contribution arising from the adiabatic torque, which becomes important for sufficiently high current densities where a linear approximation is not appropriate [Kim+11; RCL11]. Under the usual conditions of the present experiments, the dominant contribution is expected from the non-adiabatic spin torque, which is described by the second term of Eq. 1.63 with the proportionality coefficient defined as [Elt+10]:

$$\sigma = \beta \frac{2\mathrm{A}\hbar\mathrm{P}}{\mathrm{e}} \frac{\mathrm{X_0}}{\lambda} \tag{1.64}$$

with the electron charge e, the cross-sectional area A of the domain wall, the current spin polarization P, the ratio between the domain wall displacement distance $\mathrm{X_0}$ and the domain wall width λ and most importantly the non-adiabaticity parameter β.

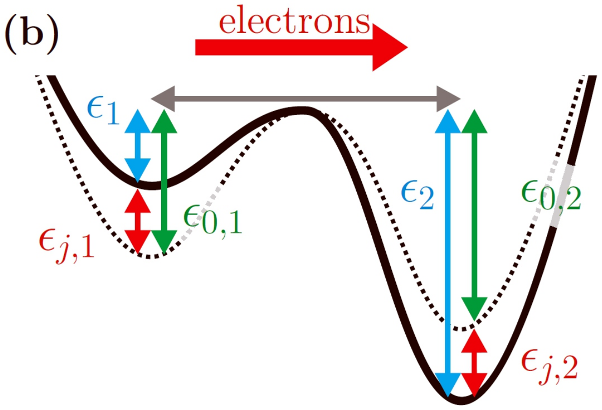

Figure 1.11: Illustration of a one dimensional potential landscape with two metastable wells. The energy barriers ϵ_S of the states S consist of a current independent contribution ($\epsilon_{0,S}$) and a current dependent contribution ($\epsilon_{J,S}$). The domain wall displacement distance X_0 is indicated by the gray arrow. (from Ref. [Elt+10]).

Furthermore, Lucassen *et al.* [LD09] pointed out that the non-adiabatic torque again enters as an effective field ($H_{\mathrm{eff}} = \beta u/\lambda\gamma$).

The non-adiabaticity parameter β can therefore be deduced by determining the dwell times (τ_1 and τ_0) as a function of the injected current density and fitting the acquired data with the following equation [Elt+10]:

$$\ln\left(\frac{\tau_1}{\tau_0}\right) = \ln\left(\frac{\tau_{0,1}}{\tau_{0,0}}\right) + \frac{\epsilon_{0,1} - \epsilon_{0,0}}{k_B T} + \frac{\sigma J}{k_B T}. \tag{1.65}$$

For constant magnetic fields, β can be extracted from the resulting slope $\sigma/k_B T$.

A detailed theoretical and experimental discussion related to the adiabatic torque can be found in the work of Ryu *et al.* [RCL11] and Kim *et al.* [Kim+11].

1.5 Magnetoresistance Effects

This part of the introduction chapter is devoted to the magnetoresistance effects enabling the characterization and detection of magnetization configurations and dynamics. These effects include the anisotropic magnetoresistance (AMR) effect, which is suitable for in-plane magnetized materials, the planar Hall effect (PHE) and the extraordinary Hall effect (EHE). The latter is most useful for the detection of domain walls within Hall cross structures when using out-of-plane magnetized materials.

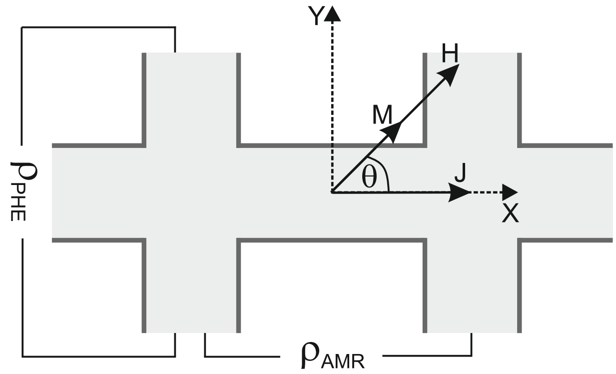

Figure 1.12: Schematic of the measurement scheme for anisotropic magnetoresistance and planar Hall effect. The directions of injected current density J and applied magnetic field H are indicated. The local magnetization M will align along the magnetic field direction for $\mathrm{H} > \mathrm{H}_{\mathrm{saturation}}$.

1.5.1 Anisotropic Magnetoresistance

Already in 1857 W. Thomson discovered an anisotropic resistance in metals and its correlation to the magnetization configuration [Tho57; MP75]. This effect can commonly be observed in ferromagnetic metals and arises from the anisotropic scattering of electrons due to spin-orbit interactions. In general, electrons flowing parallel to the local magnetization experience a stronger scattering leading to a higher resistivity $\rho_{\|}$ compared to the electrons flowing perpendicular to the local magnetization having a lower resistivity $\rho_{\perp}$.

A phenomenological approach to describe this phenomena is given by McGuire *et al.* [MP75] and R. R. Birss [Bir64] introducing a resistivity tensor ρ_{ij}. For a known current density J_{j} along a crystallographic axes, the electric field is given by:

$$\mathrm{E}_{\mathrm{i}} = \rho_{\mathrm{ij}}(\alpha_{\mathrm{i}})\mathrm{J}_{\mathrm{j}} \tag{1.66}$$

with a resistivity tensor ρ_{ij} as a function of the direction cosine α_{i} of the magnetization with respect to the crystallographic axes. Performing a series expansion, the tensor can be divided into a symmetric and an antisymmetric part. Symmetry considerations allow one to simplify the symmetric part of the tensor in the case of polycrystalline systems leading to the following expression [MP75]:

$$\rho_{\mathrm{AMR}}(\theta) = \rho_{\perp} + (\rho_{\|} - \rho_{\perp})\cos^2(\theta). \tag{1.67}$$

This final resistivity depends on the parallel resistivity $\rho_{\|}$ and perpendicular resistivity $\rho_{\perp}$ with respect to the direction of the current flow and furthermore on the angle θ

between the direction of the current flowing in the material and the local magnetization (see Fig. 1.12). For typical ferromagnetic metals (Co, Ni, Fe and alloys), the resistance change can be up to 1% of the total resistance allowing also for the detection of the presence of domain walls [MP75; Kl03].

1.5.2 Planar Hall Effect

The measurement of the transverse voltage developed perpendicular to the current, while applying an in-plane magnetic field (see Fig. 1.12), allows one to determine the planar Hall effect sharing the same physical origin as the anisotropic magnetoresistance [See+11]. A detailed discussion of the spin-orbit interaction and the resulting differences between the longitudinal and transversal resistivity is given by J. Smit [Smi51] and McGuire *et al.* [MP75].

For further considerations with respect to the analysis of the experimental data in this work, the phenomenological approach will be used. Taking into account the off-diagonal elements of the resistivity tensor ρ_{ij} as introduced in Sec. 1.5.1, one can derive the planar Hall resistivity ρ_{PHE} analogously to the anisotropic magnetoresistivity ρ_{AMR} [MP75; Bir64]. In the case of a polycrystalline material, a simple expression can be derived as [Mud+05]:

$$\rho_{\mathrm{PHE}}(\theta) = \rho_{\mathrm{s}}\sin(2\theta) \tag{1.68}$$

with the coefficient $\rho_{\mathrm{s}} = \frac{1}{2}(\rho_{\|} - \rho_{\perp})$ (s: symmetric part). Here, $\rho_{\|}$ denotes the resistivity parallel to the direction of the current flow, $\rho_{\perp}$ the perpendicular resistivity and θ the angle between the direction of the current flowing in the material and the local magnetization (see Fig. 1.12).

For the more general case of crystalline materials, the antisymmetric part of the magnetoresistivity tensor and the crystallographic axes have to be taken into account thus leading to the addition of further terms to Eq. 1.68 [Mud+05]:

$$\rho_{\mathrm{PHE}}(\theta) = \rho_{\mathrm{s}}\sin(2\theta) + \rho_{\mathrm{as}}^{0}\cos(\theta) + \rho_{\mathrm{as}}^{1}\cos^{3}(\theta) \tag{1.69}$$

using the coefficients $\rho_{\mathrm{as}}^{\mathrm{i}}$ (as: antisymmetric part).

1.5.3 Extraordinary Hall Effect

The well known ordinary Hall effect (OHE) leads to the development of a transverse voltage with respect to the current direction when applying an external magnetic field. This effect is also relevant even in non-magnetic materials, being proportional to the magnetic induction B. Its sign is determined by the type of charge carried (electron or hole). In addition to the ordinary Hall effect, ferromagnetic materials, especially out-of-plane magnetized ones, exhibit a further contribution to the Hall effect, the extraordinary or anomalous Hall effect (EHE or AHE). Its magnitude is directly proportional to the local magnetization M. In general, the total Hall resistivity is given by:

$$\rho_{\mathrm{H}} = \rho_{\mathrm{OHE}}\mathrm{B} + \rho_{\mathrm{EHE}}\mathrm{M}. \tag{1.70}$$

Despite a long history of research the mechanisms leading to the extraordinary Hall effect remain controversial. By now, three main contributions are commonly accepted: i) an intrinsic anomalous velocity (ρ_{int}) [KL54], ii) an extrinsic skew scattering at impurities (ρ_{sk}) [Smi58] and iii) an extrinsic side jump at impurities (ρ_{sj}) [Ber70]. The total extraordinary Hall resistivity is the sum of all these contributions:

$$\rho_{\mathrm{EHE}} = \rho_{\mathrm{int}} + \rho_{\mathrm{sk}} + \rho_{\mathrm{sj}}. \tag{1.71}$$

Next, a brief introduction of each contribution will be given. A more detailed review about theory and experimental state of the art is presented by Nagaosa *et al.* [Nag+10] and N. A. Sinitsyn [Sin08].

Intrinsic Anomalous Velocity

Electrons in real crystals do not behave like free particles due to a strong interaction with the periodic potential of the lattice. Karplus and Luttinger [KL54] formulated a theory based on the spin-orbit interaction together with an interband mixing resulting in an anomalous velocity. As indicated in Fig. 1.13a), the resulting velocity is transverse to the electric field E. Various other theoretical approaches (linear transport, Boltzmann equation, Berry phase theory, etc.) were developed later leading to formulations of an intrinsic resistivity scaling with the normal longitudinal resistivity ρ_{xx} [Nag+10; Sin08;

KL54; TYJ09]:

$$\rho_{\mathrm{int}} \propto \rho_{\mathrm{xx}}^2. \tag{1.72}$$

Extrinsic Skew Scattering

The skew scattering approach to explain the extraordinary Hall effect was developed by J. Smit [Smi58] in 1958 proposing an extrinsic source (impurities) being responsible for changes of the resistivity. Calculations of the Hall resistivity assuming spin-orbit interactions reveal an imbalance in the transition probability when describing scattering processes. The skew scattering represents the asymmetric part of the transition probability, as it turns out that the scattering probability $\mathrm{W}(\mathbf{k} \rightarrow \mathbf{k}')$ is different from $\mathrm{W}(\mathbf{k}' \rightarrow \mathbf{k})$ leading to an additional transverse current with respect to the longitudinal current. In this case, the following proportionality to the longitudinal resistivity can be found [Nag+10; Sin08; Smi58; TYJ09]:

$$\rho_{\mathrm{sk}} \propto \rho_{\mathrm{xx}}. \tag{1.73}$$

Extrinsic Side Jump

L. Berger suggested a further mechanism related to impurities, the side jump. Based on the spin-orbit interaction L. Berger [Ber70] calculated a finite sideways displacement (10^{-10} to $10^{-11}\,\mathrm{m}$) for the center of mass of a wave packet when scattered at a central potential (e.g. an impurity). Here, the impurity cause a distortion of the wave function resulting in a local current density. The scaling of the resistivity with respect to the longitudinal resistivity is given by [Nag+10; Sin08; Ber70; TYJ09]:

$$\rho_{\mathrm{sj}} \propto \rho_{\mathrm{xx}}^2. \tag{1.74}$$

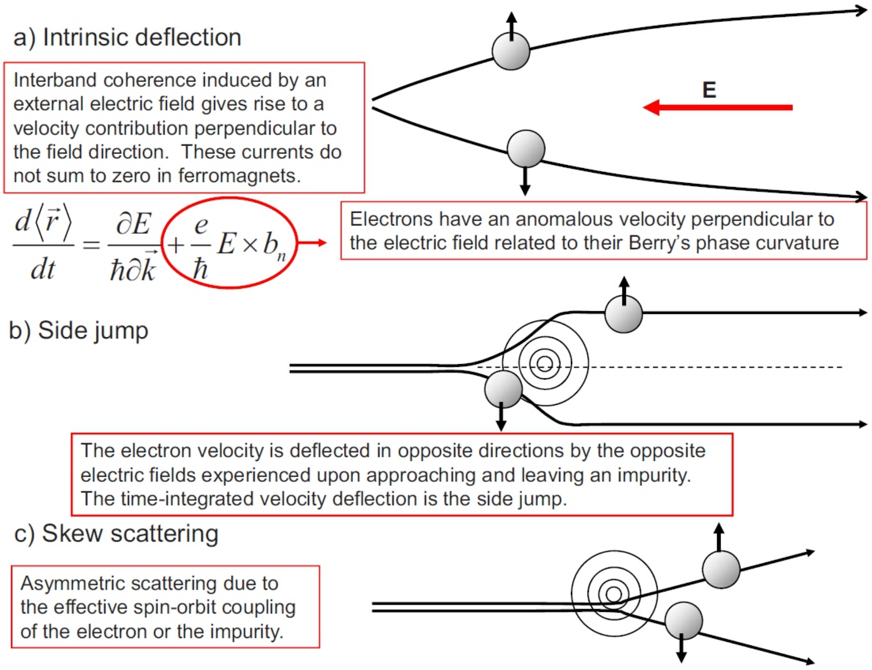

Figure 1.13: Brief explanation and illustration of the three main contributions to the extraordinary Hall effect. (from Ref. [Nag+10]).

In general, the longitudinal resistivity can be split in a temperature independent resistivity, the residual resistivity ρ_{xx0}, and a temperature dependent phonon-induced resistivity ρ_{xxT} [TYJ09; VSJ11]. The overall scaling for the extraordinary Hall effect combining all the aforementioned effects is then given by [VSJ11]:

$$\rho_{\mathrm{EHE}}(\mathrm{T}) = \rho_{\mathrm{xy0}} + (\mathrm{a} + 2\sigma^{\mathrm{int-sj}}\rho_{\mathrm{xx0}})\rho_{\mathrm{xxT}}(\mathrm{T}) + \sigma^{\mathrm{int-sj}}\rho_{\mathrm{xxT}}(\mathrm{T})^2 \tag{1.75}$$

with the temperature independent contribution to the extraordinary Hall effect

$$\rho_{\mathrm{xy0}} = \mathrm{a}\rho_{\mathrm{xx0}} + \sigma^{\mathrm{int-sj}}\rho_{\mathrm{xx0}}^2. \tag{1.76}$$

The coefficient a contains the information about the skew scattering, while the coefficient $\sigma^{\mathrm{int-sj}}$ combines the information of the intrinsic contribution and the side jump effect. A more detailed derivation of these equations can be found in the work of Vilanova *et al.* [VSJ11].

Furthermore, these equations highlight the problem of separating the various contributions to extraordinary Hall effect since the skew scattering scales with the residual resistivity ρ_{xx0} and the temperature dependent phonon-induced resistivity ρ_{xxT}. Intrinsic contribution and side jump effect scale with ρ_{xx}^2 preventing an easy experimental separation of each contribution. A proposal for an experimental determination of the intrinsic and side jump effect is presented by Tian *et al.* [TYJ09] requiring a variation of the material layer thicknesses.

2

Instrumentation

The magnetoresistance and magnetotransport measurements in the framework of this thesis were performed using the measurement setup presented in Fig. 2.1. The various components to fulfill the specialized requirements of these measurements, such as a tunable environmental temperature, in-plane and out-of-plane magnetic fields and high-frequency compatible electrical leads, are presented in the following sections.

2.1 Cryostat

To provide a tunable environmental temperature, we use a bath cryostat system designed by Scientific Magnetics [Mag08]. A schematic of the cryostat is shown in appendix A (see Fig. A.1). The large Helium reservoir allows for long term measurements of about two to three days depending on the use of the magnet system and the set temperature. Since the 3D-vector magnet system is built of a superconductive material, it is placed within the helium reservoir to provide continuous cooling.

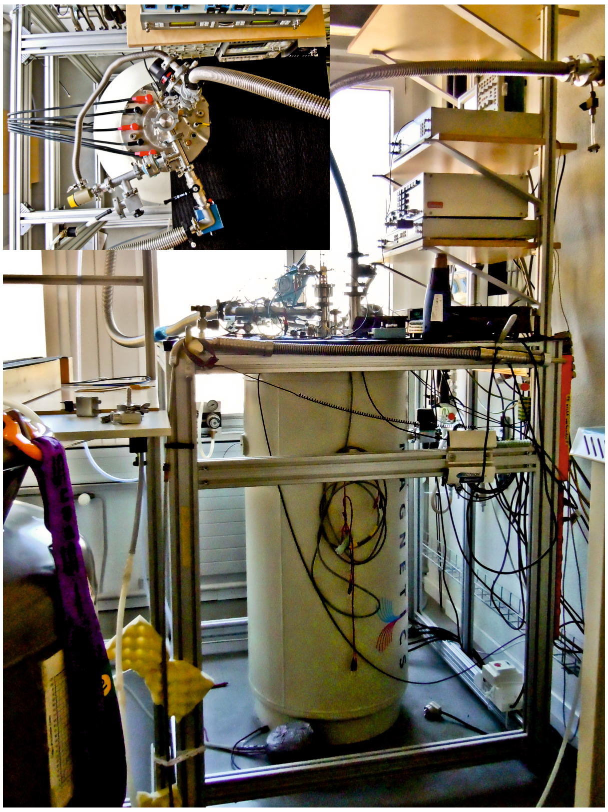

Figure 2.1: Front and top view (inset) of the measurement setup located at the Paul-Scherrer-Institut in Switzerland.

The sample is loaded from the top into a variable temperature insert (VTI), which is isolated from the helium reservoir by an isolating vacuum. The VTI temperature can be set between 1.2 K (experimentally only tested down to 1.8 K) and 325 K (limited by the temperature sensors used). The temperature can be monitored continuously using two temperature sensors (model: *Cernox CX-1050-SD-1.4L*). The first sensor is permanently positioned close to the heater foil within the VTI, which is used to control the temperature of the helium flowing into the VTI. The second sensor is optionally located on the sample holder close the sample for a more accurate determination of the sample temperature.

2.2 Design of the Magnet System

The 3D-vector magnet system, shown in Fig. 2.2, consists of three coils, which are independently controlled by three separate power supplies (*Lake Shore Model 625*). The main features of each coil are listed in the table 2.1. The Y-coil creates a magnetic field perpendicular to the sample holder, while the X- and Z-coil can be used to create in-plane magnetic fields (see Fig. A.1). The superposition of the magnetic fields allows one to apply a magnetic field in any arbitrary direction. The installed Hall sensors in the center of each coil (see Fig. 2.2(b)) can be used to monitor the applied magnetic field.

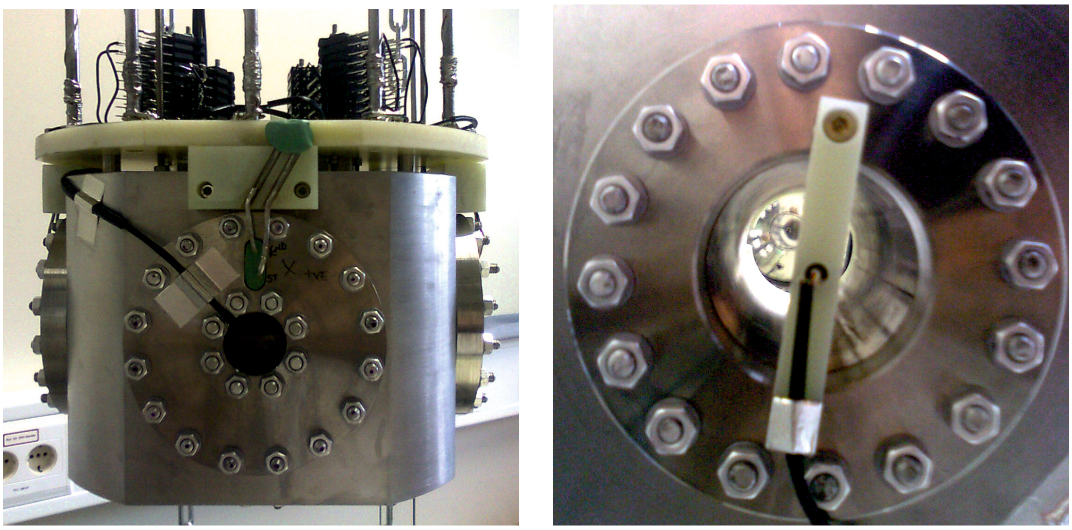

(a) (b)

Figure 2.2: (a) Side view of the 3D-vector coil magnet. (b) Bottom view of the 3D-vector coil magnet. Hall sensors are installed in the center of each coil.

Magnetic field direction	Maximum field	measured hysteresis	Ramp rate
out-of-plane (Y-coil)	5 T at 56.9 A	4.8 G from > 1000 G	$1.05\,\mathrm{T\,min^{-1}}$
in-plane (X-coil)	1 T at 57 A	11.9 G from > 300 G	$1.03\,\mathrm{T\,min^{-1}}$
in-plane (Z-coil)	1 T at 56.7 A	15.7 G from > 100 G	$1.05\,\mathrm{T\,min^{-1}}$

Table 2.1: Specifications of the 3D-vector coil magnet system. The values are taken from the test summary performed by Scientific Magnetics [Mag08].

The measured hysteresis of the three coils (see table 2.1) is confirmed experimentally (see Fig. 2.3), but beginning at lower magnetic fields in the case of the X-coil and the Z-coil. Here, the measurements reveal an increasing hysteresis, which limits the maximum magnetic field amplitude for the experiments performed during this work. In the case of the Y-coil, no significant hysteresis can be observed for magnetic fields below 1000 G.

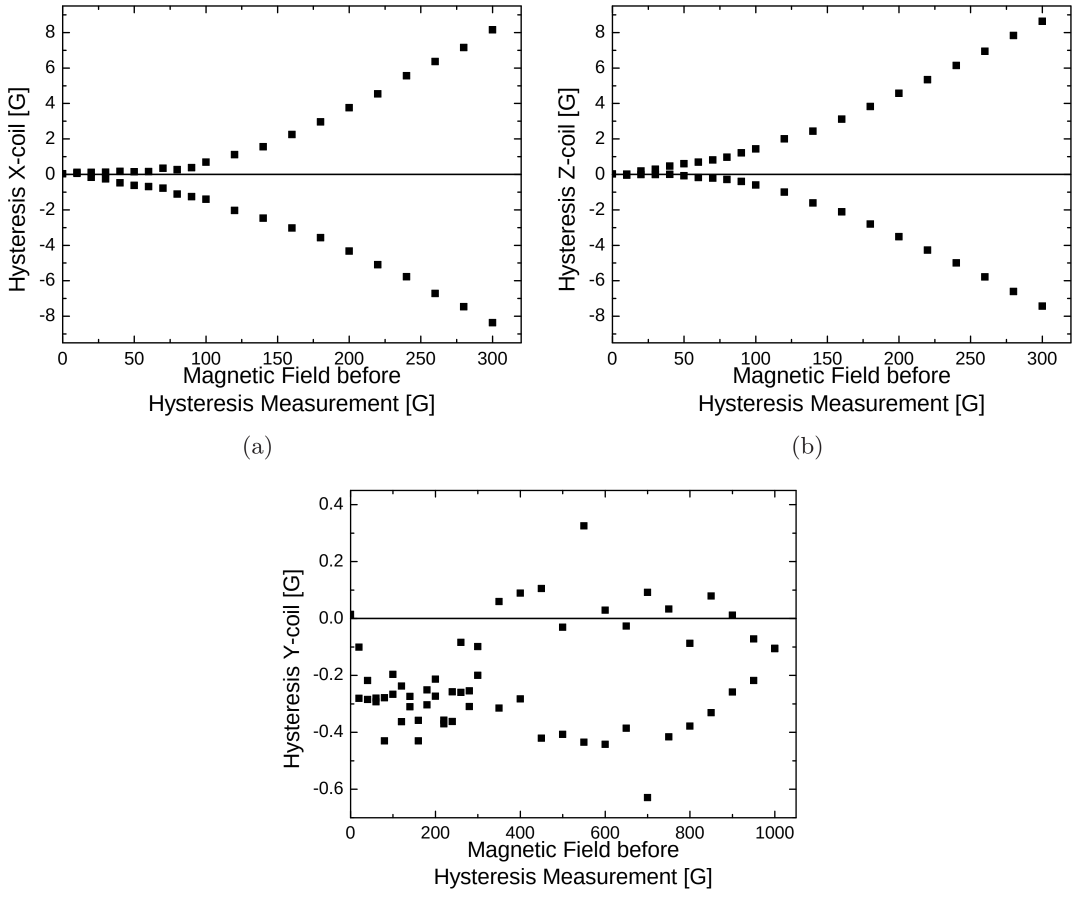

(a)

(b)

(c)

Figure 2.3: Hysteresis of the X-coil (a), Z-coil (b) and Y-coil (c) as a function of the magnetic field, which was applied before setting the magnetic field to zero. The remanent magnetic field was then measured using Hall sensors.

2.3 Design of the Sample Holder

Significant effort has been put into the design of the sample holder.[1] Limited by the inner diameter of the VTI, the sample holder offers only limited space for the sample (10 mm × 10 mm) and the large quantity of electrical contacts necessary to meet the experimental requirements. In Fig. 2.4 the front side of the sample holder is shown. The sample can be glued onto the central pad, which is permanently connected to the ground to improve the injection of high-frequency signals. The reduction of the total number of low-frequency contacts allowed us to install a temperature sensor close to the sample.

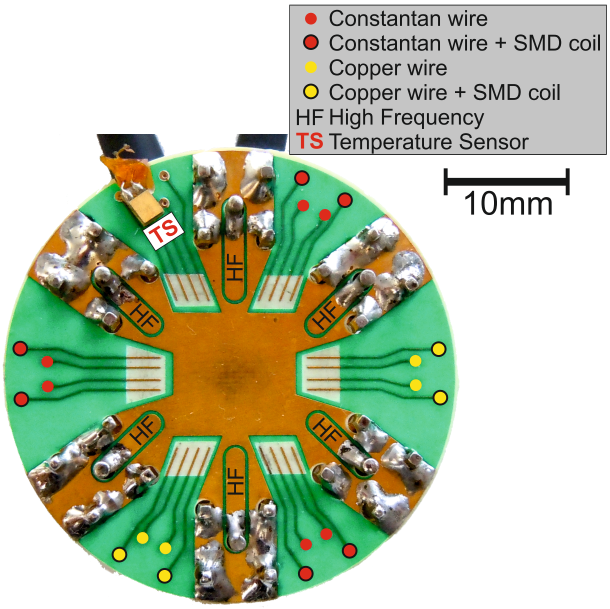

Figure 2.4: Front side view of sample holder. The electrical leads, high-frequency and low-frequency, and the position of the temperature sensor are indicated.

To prevent heat conduction/exchange from outside the cryostat to the sample, the sample holder is fixed at the bottom of the sample rod using semirigid high-frequency cables (see Fig. A.2). Furthermore, baffles are attached along the whole sample rod.

---

[1] Thanks to C. Dette (University Konstanz).

2.3.1 Low-frequency Connections

The remaining low-frequency contacts available on the sample holder (see Fig. 2.4) are connected to the top of the sample rod using copper and constantan leads. The constantan wires are suitable for low temperature experiments for which the thermal conduction needs to be reduced. The total resistance of one constantan lead from the sample holder to the BNC connector of the switching box is about $120\,\Omega$. In contrast, the copper leads can be used for experiments requiring high electrical conductivity since the total wire resistance is only a few Ω. For both types of leads we used a cable consisting of twelve twisted pairs. Here, one wire of the twisted pair is the signal lead, while the other wire is connected to the ground in order to reduce crosstalk between two signal leads.

During this work, further alterations were required due to the need for the injection of ns-long pulses into nanowire structures. In order to reduce reflections at the Hall cross contacts, SMD-coils were attached to some of the low-frequency leads on the back side of the sample holder increasing the total resistance of each lead by about $40\,\Omega$.

2.3.2 High-frequency Connections

Six semirigid coaxial cables provide high-frequency connections to the sample. At the bottom side the sample holder is directly attached to these cables using SMA couplers. On the top side of the sample rod, SMA feedthroughs are used, which are inserted into a flange (see Fig. A.2). Since the sample rod has to endure many cycles between low temperatures of only a few Kelvin and room temperature, the semirigid cables are tempered to avoid a rupture of the central conductor and damages due to dielectric extrusion.

On the sample side (see Fig. 2.4), the SMA connectors are soldered to specially designed coplanar waveguides to ensure the required impedance matching. A detailed description of the coplanar waveguide design and testing procedures can be found in the work of D. Bedau [Bed08]. The final sample holder was then tested using a time-domain reflectometer (TDR). The results are shown in Fig. 2.5. The first strong reflections of the injected pulse, which is indicated by the first steep increase, occur at the top side of the sample rod where SMA feedthroughs have been used. As discovered by D. Bedau [Bed08], the reflections, which occur at the sample holder and the sample (bonding wires) itself, are reduced when the number of bonding wires is increased.

In general, the sample itself seems to be the strongest source of reflections. Finally, reflections occur again at the top of the sample holder, where a 50 Ω resistor had been used as a terminating resistor.

To further test the high-frequency connections, short 10 ns long pulses with a short rise time of 55 ps were injected in the same configurations as used for the TDR measurements. Here, the effect of the number of used bonding wires on the width, rise and fall time is small. However, the measurements show that the short rise time of the original pulse (55 ps) was not reproduced. The measured rise times shown in Fig. 2.5 range from 900 ps to 1080 ps.

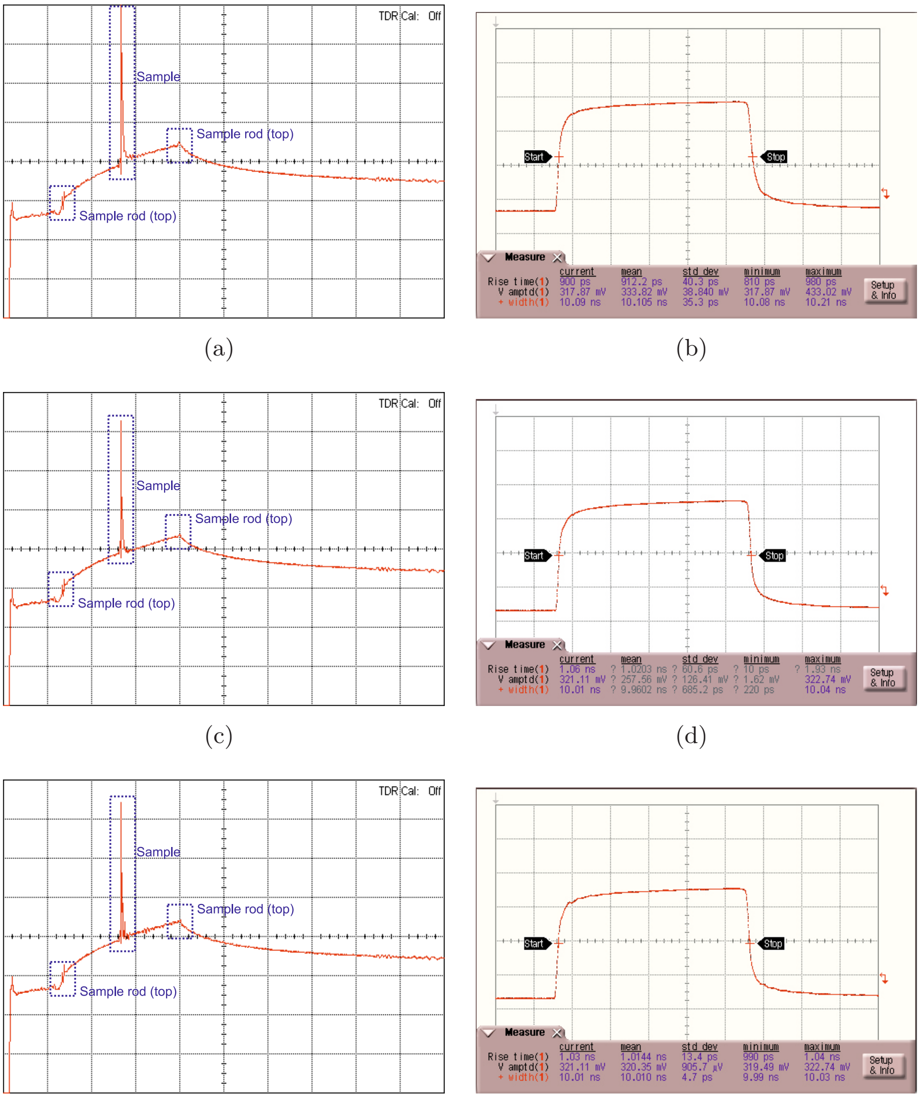

```
             current    mean       std dev    minimum    maximum
Rise time(1) 900 ps     912.2 ps   40.3 ps    810 ps     980 ps
 V amptd(1)  317.87 mV  333.82 mV  38.840 mV  317.87 mV  433.02 mV
 + width(1)  10.09 ns   10.105 ns  35.3 ps    10.08 ns   10.21 ns
```

(a) (b)

```
             current     mean           std dev        minimum      maximum
Rise time(1) 1.06 ns   ? 1.0203 ns  ? 60.6 ps    ? 10 ps     ? 1.93 ns
 V amptd(1)  321.11 mV ? 257.56 mV  ? 126.41 mV  ? 1.62 mV     322.74 mV
 + width(1)  10.01 ns  ? 9.9602 ns  ? 685.2 ps   ? 220 ps      10.04 ns
```

(c) (d)

```
             current    mean       std dev    minimum    maximum
Rise time(1) 1.03 ns    1.0144 ns  13.4 ps    990 ps     1.04 ns
 V amptd(1)  321.11 mV  320.35 mV  905.7 µV   319.49 mV  322.74 mV
 + width(1)  10.01 ns   10.010 ns  4.7 ps     9.99 ns    10.03 ns
```

(e) (f)

Figure 2.5: Time-domain reflectometry using (a) a single bonding wire between two coplanar waveguides and (e) four bonding wires. In the case (c), a gold contact pad was used between two coplanar waveguides contacted by three bonding wires on each side. The main reflections are caused by the sample itself, but additional strong reflections occur at the SMA connectors and feedthroughs at the top side of the sample rod. The time resolution is 10 ns/div for all TDR images. The right picture column (b,d and f) shows the transmitted shape of 10 ns long pulses injected into the corresponding configuration used for the time-domain reflectometry.

2.3.3 Switch Box

The low-frequency leads are contacted outside the VTI using two Fisher connectors, one for each type of material (copper and constantan). A special switch box was designed to provide access to the sample and a safety circuit is used to prevent the sample from being damaged due to voltage discharges.

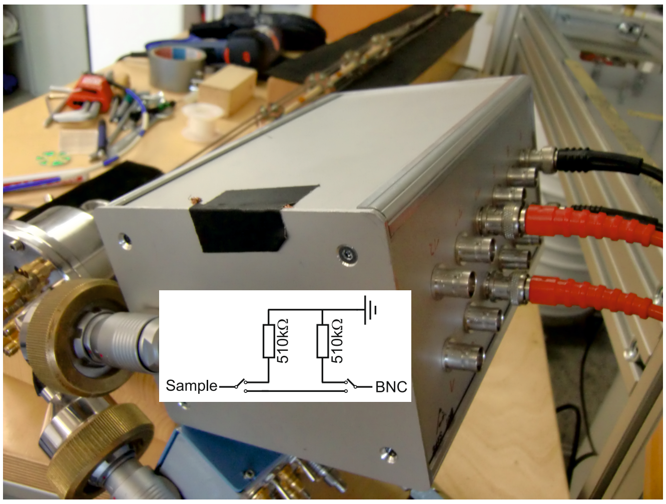

Figure 2.6: The switch box and a schematic of the safety circuit.

In Fig. 2.6 the switch box is shown including a schematic of the safety circuit used for each signal lead. Using a series of two switches allows one to discharge a device or cable via a large resistor (several kΩ) before closing the direct connection to the sample. Here, the resistor is chosen to be much larger than the sample resistance to reduce the maximum possible current in case of voltage discharges occurring, e.g. while turning on a device or in the case of general power failures. The same safety procedure works for the sample when first connecting it to the sample holder.

2.3.4 Electrical Connections and Grounding

If two or more devices sharing the same ground connection are used for a measurement, the connections and ground span an area which will act as an antenna for radio frequencies. This effect caused by ground-loops can be reduced by the use of short wires and at least by providing a central earth ground. A schematic of the electrical wiring is shown in Fig. 2.7. The first constraint (short wires) is met by positioning all devices in close proximity to the switch box and the high-frequency connections at the top of the sample rod. To fit the second constraint (central earth ground), all devices are separated from the ground of the common power grid using isolating transformers. The device ground is then provided from a central earth ground connection fixed to the metal frame surrounding the cryostat. This star-shape geometry includes also the cryostat itself, which is separated from the common ground by electrically isolating elements installed in the helium recovery pipes and the pipes leading to the vacuum pump.

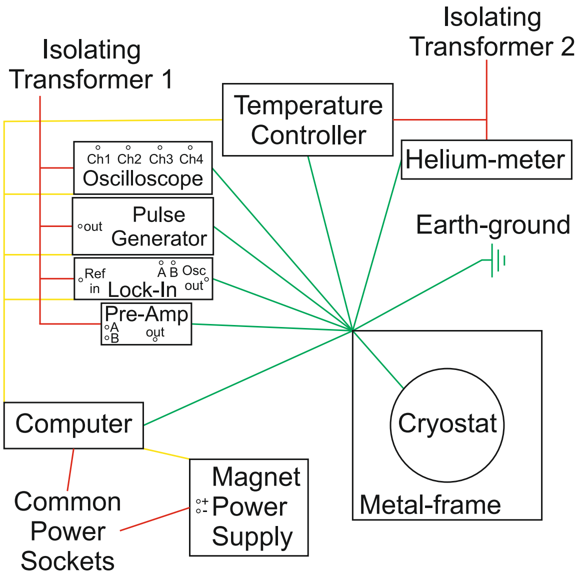

Figure 2.7: Schematic of the electrical wiring of the measurement setup. The devices involved in the measurement are separated from the common power grid using isolating transformers. A star-shaped earth ground connection is re-established (green lines) from a central ground knot at the metal-frame surrounding the cryostat. The power supply is indicated by red lines. A GPIB system is used to control the devices (yellow lines).

Note that the GPIB system used for communication between the computer and the measurement devices uses cables and therefore causes further ground-loops. This problem is not solved yet, but a solution might be given by the use of optocouplers.

3

Sample Fabrication

The fabrication of nanostructures suitable for spintronic applications is technically demanding. The experiments performed during this work required nanostructures with an exact material composition and very accurate and precise layouts. Although the sample fabrication is a crucial step towards the success of an experiment, only a brief introduction about the material deposition and the patterning processes will be given in the next sections.

Since the sample fabrications consumes a significant amount of time the help of many people from various locations were required.[1]

---

[1] Thanks to O. Boulle, G. Malinowski, C. Ulysse, and G. Faini for the design and fabrication of the Co/Pt based multilayer materials, B. Ocker and co-workers of Singulus Technologies AG for fruitful discussions and the preparation of the Co/Ni based multilayer materials, the group of D. Ravelosona for providing the Co/Ni-CoFeB sample, the group of C. Felser for the fabrication of the Heusler alloys and J. Rhensius for the patterning and contacting of the many nanostructures.

3.1 Material Deposition

As discussed in the theory chapter, the correct material composition determines whether a magnetic structure has an in-plane or an out-of-plane magnetization configuration. Even small changes of a few Ångström in the layer thickness can alter the whole magnetization configuration. Therefore, precisely controlled material deposition techniques are necessary.

3.1.1 Thermal Evaporation

This technique is mainly used for the deposition of materials used for the alignment markers and electrical leads to the nanostructures. The material (Cr, Au, Al, etc.) is placed on a tungsten crucible, which is heated by applying a high current (Joule heating effect). The evaporated material is then deposited on the sample located upside down above the tungsten crucible. The pressure inside the evaporation chamber is lowered to about 10^{-5} mbar to reduce impurities. The film thickness is controlled using a quartz thickness monitor. Typical material compositions for the electrical contacts are Cr($6 - 8\,\mathrm{nm}$)/Au($50 - 200\,\mathrm{nm}$)[Rhe11] using the Cr as an adhesion layer.

3.1.2 Sputter Deposition

This technique is used to precisely deposit thin material layers with specific layer thicknesses [KA00]. A quartz thickness monitor located in close proximity to the sample is used to measure the thickness, while the material is deposited. The sputtering process itself is driven by a momentum transfer between ions and atoms in a target material. The ions (typically Argon) are accelerated out of a cathode and redirected towards a target material. If the kinetic energy and ion mass is sufficiently large, the binding energy of the surface atoms of the target material is overcome and atoms are broken off, redepositing on the nearby placed sample.

3.2 Patterning Processes

Two different patterning processes were used to fabricate the nanostructures studied in this work: i) the lift-off process and ii) the etching process. A more detailed introduction of these processes is given by J. Rhensius [Rhe11].

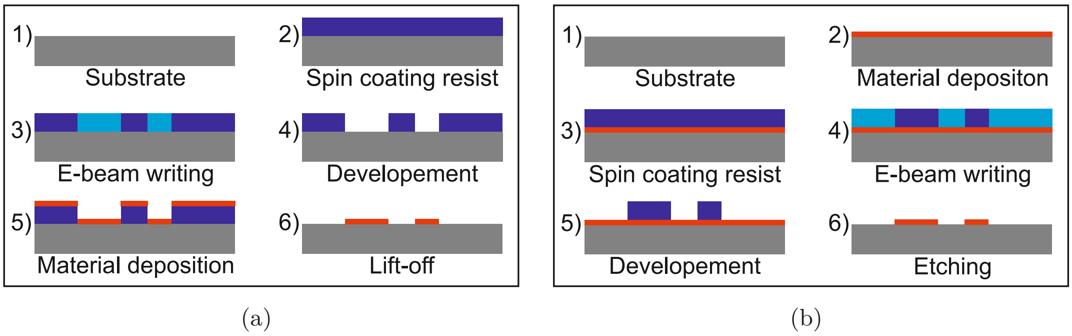

(a) (b)

Figure 3.1: Schematic overview on the sample fabrication process using (a) the lift-off technique or (b) the etching technique.

3.2.1 Patterning by Lift-off

A schematic of the patterning by lift-off process is shown in Fig. 3.1(a). This process starts with a substrate (1), on which a thin layer of a positive photoresist is deposited using spin coating (2). The region of interest (structure geometry) is exposed using an e-beam lithography system (3). This exposed positive photoresist is then removed in a developer solution leaving free space on the substrate (4). The desired material composition is then deposited using techniques such as described in the sections 3.1.1 and 3.1.2 (5). The remaining resist, as well as the material on top of it, is removed (lift-off) using a solvent (6).

If further electrical leads are required, the whole process has to be repeated using a marker system to control the e-beam writing process for a precise alignment of the contacts to the nanostructure.

3.2.2 Patterning by Etching

The second patterning process shown schematically in Fig. 3.1(b) starts again with a substrate (1), on which the desired material is deposited (2) before spin coating a thin layer of negative photoresist (3). The region of interest (structure geometry) is exposed using an e-beam lithography system (4). In contrast to the lift-off process, the exposed negative photoresist remains on the substrate, while the rest is removed in a developer solution (5). Using e.g. an Ar-Ion miller, one is able to etch away the deposited material leaving only the region covered by the remaining negative photo resist, which is removed in a solvent later on. Additional electrical leads can be fabricated using a second lift-off step.

In the case of special experimental requirements, such as the use of insulating substrates (e.g. the Heusler alloy deposited on MgO studied in Sec. 4.3), extended patterning processes are necessary, which are described in detail by J. Rhensius [Rhe11].

4

Experiments for Sample Characterization

The outcome of the experimental work will be presented in the following two chapters. To begin with, the sample characterization is one of the first steps towards a detailed overview of the physical properties of a magnetic material and its capability to be suitable for spintronic applications.

First, a short introduction to scanning electron microscopy will be given followed by a discussion of the various nanowire geometries used in the experiments. The following two sections focus on the two magnetization configurations, out-of-plane and in-plane. Each section consist of a brief motivation, experimental techniques, data analysis procedures, results and a discussion. In the case of the out-of-plane magnetized materials the extraordinary Hall effect is in the focus, while in the case of the in-plane magnetized material the anisotropic magnetoresistance and the planar Hall effect are investigated.

4.1 Scanning Electron Microscopy

One, but not the simplest, imaging method is the scanning electron microscopy. Since, the resolution of an optical microscope is limited by the wavelength of the used light (visible light: about 400 nm to 800 nm), it is not suitable to image structures on the nanoscale in detail. Hence, electrons with a de-Broglie wavelength being much shorter are more suitable for these types of structures. These short wavelengths can be achieved by tuning the acceleration voltage of the electrons. The only limitation of the resolution is then given by the quality of the used electron lenses and the spot size of the electrons. Nevertheless, wavelengths down to a few nm can be created for typical acceleration voltages of a few kV. The generated electron beam is now moved across the surface of the sample creating secondary electrons, which are detected by either an in-lens detector resulting in a spatially high resolved top-view image or an secondary electron detector being suitable for surface images.

Next, scanning electron microscopy images of different magnetic structures are shown in Fig. 4.1 and Fig. 4.2. In general, the pads with the brighter contrast indicate the gold contacts, which are bonded to the electrical leads of the sample holder. Since, the magnetization configurations, in-plane and out-of-plane, generate different effects, various types of geometries are required. In the case of out-of-plane magnetized materials (see Fig. 4.1), the Hall cross geometry is commonly used. Here, the gold contacts are chosen to be in close proximity to reduce the total resistance in between making these structures also suitable for experiments with short ns pulses. In most cases, larger pads, so-called nucleation pads, as indicated in Fig. 4.1(c) and Fig. 4.1(d) are attached at one end of the wire to increase the probability to nucleate domain walls. Another approach to nucleate domain walls is the creation of local Oersted fields (see also section 1.4.1) by use of gold bars placed across the nanowire as indicated in Fig. 4.1(d).

In case of in-plane magnetized materials, the nucleation of domain walls can be achieved by a zigzag-wire geometry and specific sequences of external magnetic fields (for details see Sec. 4.3). In Fig. 4.2(a) it can be seen that two gold contacts are located around a kink of the top wire and of the bottom wire. This contact design is useful to locally detect the presence of a domain wall.

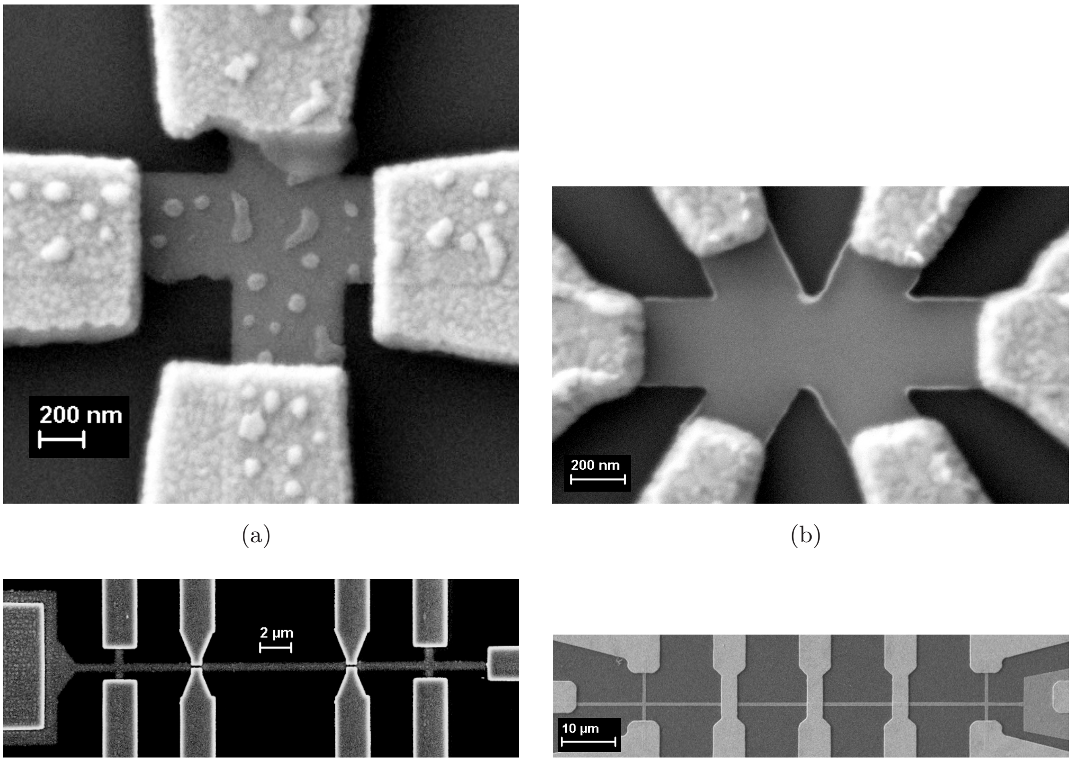

(a) (b)

(c) (d)

Figure 4.1: Scanning electron microscopy images of the out-of-plane magnetized structures. The pads with the brighter contrast indicate the gold contacts, which are bonded to the electrical leads of the sample holder. (a) Single Hall cross geometry with gold contacts close to the Hall cross to reduce the total resistance between the contacts. Defects arising from a remaining resist can be seen. (b) Two Hall crosses attached along a wire in a diagonal geometry. The short distance between the gold contacts enable the injection of ns pulses. (c) A several µm long nanowire with two attached Hall crosses and two further gold contacts in Hall cross geometry in between. A large domain wall nucleation pad is added to the wire on the left side. (d) Several tens of µm long wire with two attached Hall crosses and gold contacts aligned across the magnetic wire to locally create Oersted fields. Additionally a domain wall nucleation pad is attached on the right side of the wire.

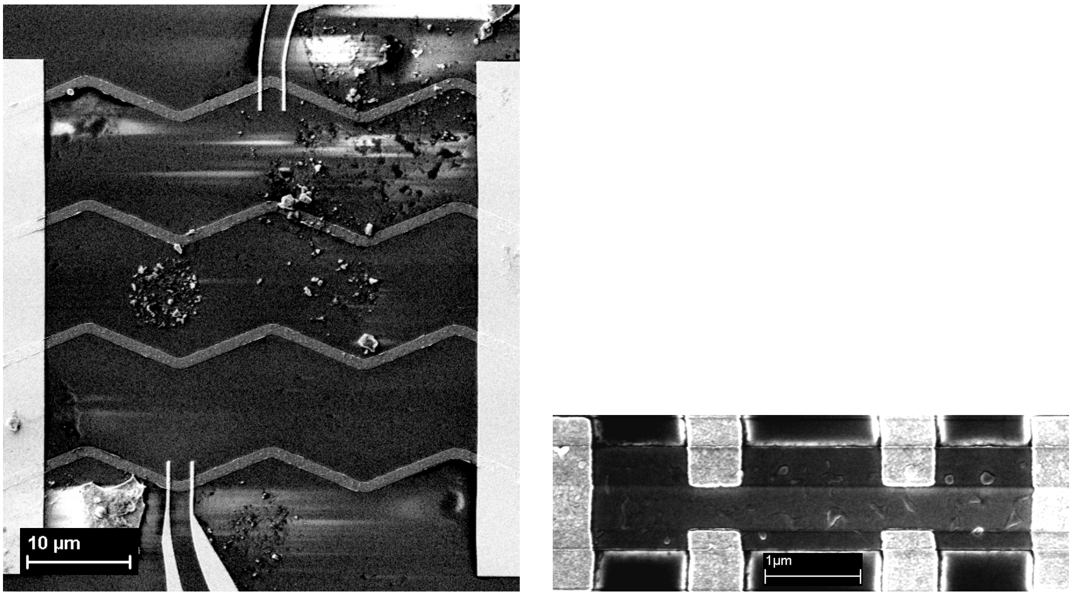

(a) (b)

Figure 4.2: Scanning electron microscopy images of in-plane magnetized structures. (a) Four parallel zigzag-wires with overlapping gold contacts on each side. Furthermore, one kink of the top zigzag-wire and one of the bottom zigzag-wire is enclosed by two more gold contacts. (b) Simple rectangular structure with gold contacts on each side. Four further gold contacts are attached along the rectangle in Hall cross geometry. Defects and impurities on top of the structures can be seen in both images.

4.2 Out-of-plane Magnetization Configurations

The first class of material compositions exhibit out-of-plane magnetization configurations. The experiments presented will provide basic knowledge about the material properties and their temperature dependence. Especially the determination of the magnetic properties is necessary to gain preliminary information whether a material is suitable for spintronic applications or not.

An important electronic property of a material is the longitudinal resistivity ρ_{xx} when studying current-induced magnetization dynamics. An example for a measurement scheme is shown in Fig. 4.3. Here, an alternating current is generated with high accuracy by an AC current source (Keithley 6221). The voltage drop is then measured using Lock-in amplifiers (Signal Recovery 7265 or 7225). Then a longitudinal resistance R_0 is measured at zero external magnetic field for various constant cryostat temperatures ranging from 310 K to 4.3 K (liquid Helium temperature). The resistivity is then determined as:

$$\rho_{\mathrm{xx}} = \mathrm{R}_0 \frac{\mathrm{A}}{\mathrm{L}} \tag{4.1}$$

with the cross-sectional area A of the wire and the length between the Hall contacts L.

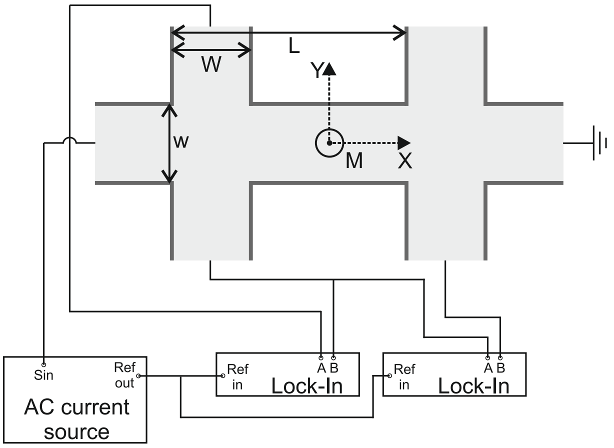

Figure 4.3: Measurement scheme for transversal ρ_{xy} and longitudinal ρ_{xx} resistivity. The magnetization M is pointing along the Z-direction. A *Keithley 6221* is used as an AC current source providing also a TTL reference signal to trigger all other devices. The voltages at the Hall cross contacts are measured with high accuracy using *Signal Recovery* Lock-in amplifiers (models: *DSP 7265* or *DSP 7225*). The width of the wire w, the width of a Hall cross W and the length between the Hall contacts L are indicated.

The second electronic property studied, the transversal resistivity ρ_{xy}, is dependent on the magnetization configuration and is theoretically introduced in Sec. 1.5.3. The measurement technique is analogous to the one used for the longitudinal resistivity. In Fig.

4.4 a three dimensional simulation[1] shows the distribution of an injected constant current density within a Hall cross geometry using Comsol Multiphysics [AB]. A homogeneous current density can be assumed at the beginning and the end of the Hall cross. The transversal resistivity ρ_{xy} is then calculated as:

$$\rho_{\mathrm{xy}} = \mathrm{R_t}\frac{\mathrm{A}}{\mathrm{W}} \tag{4.2}$$

with the transversal resistance $\mathrm{R_t}$, the cross-sectional area A of the wire and the width of the Hall cross W. The ρ_{xy} values are measured at zero field in order to exclude the ordinary Hall effect (see Fig. 4.5). Other publications might differ by a factor of 1/2 due to a different definition of ρ_{xy}.

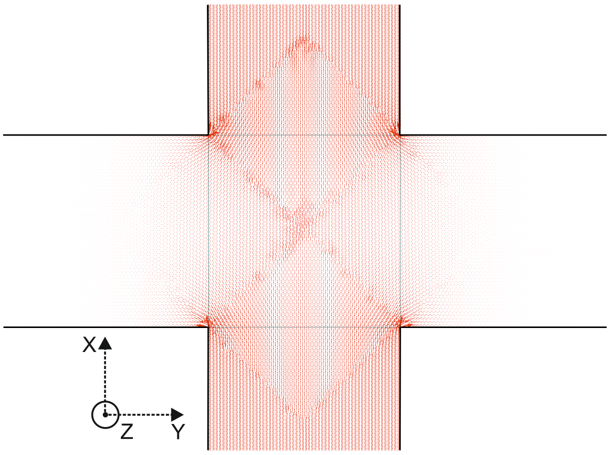

Figure 4.4: Three dimensional simulation of a constant current density ($1 \cdot 10^{10}$ A/m^2) injected into a wire with an attached Hall cross using Comsol Multiphysics [AB]. The length of the arrows represents the local magnitude of the current density.

The next part of this section shows the results for different material compositions, whose stable magnetic configurations point out-of-plane. The data points are acquired by measuring five hysteresis curves at each constant cryostat temperature and calculating their corresponding mean value. The errors defined as the standard deviation of the mean value are negligibly small in case of the longitudinal and transversal resistivity measurements and therefore not shown in the plots.

In order to analyze the data, the plots of the transversal resistivity ρ_{xy} are divided in two temperature regimes: i) a low temperature regime (4.3 K to < 50 K) and ii) a high

---

[1] Simulation parameters: Geometry: wire width w = 500 nm, Hall cross width W = 500 nm and wire thickness d = 10 nm; Mesh: Free tetrahedral (min. size 1 nm, max. size 10 nm); Current density: $1 \cdot 10^{10}$ A/m^2 injected perpendicular to one end of the wire, the ground is fixed at the other end of the wire.

temperature regime (50 K to 310 K). This classification of regimes has been chosen, since a deviation from the linear scaling of the longitudinal resistivity ρ_{xx}, which is a crucial parameter for the following analysis, occurs for most of the examined materials at about 50 K (see for instance Fig. 4.6(a)). At lower temperatures the resistance converges towards the residual resistivity ρ_{xx0}, which is in the following measurements approximated as the longitudinal resistivity at 4.3 K.

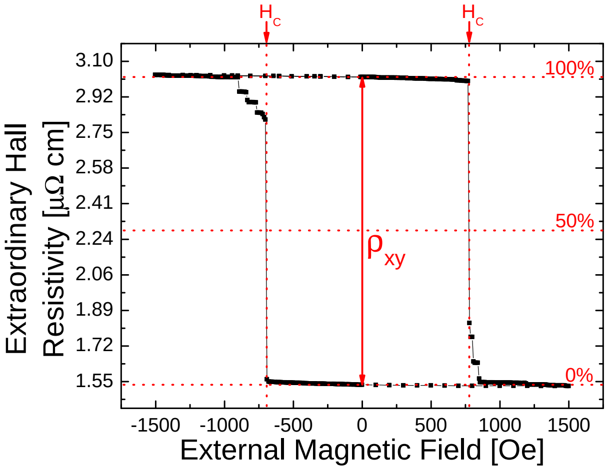

Figure 4.5: Demonstration of the definition of ρ_{xy} using a hysteresis curve measured at 4.3 K using the Co/Pt multilayer material. The coercive field $\mathrm{H_C}$ is defined as the external magnetic field necessary to reverse 50% of the magnetization within a Hall cross, which is indicated by a 50% change of the extraordinary Hall signal.

The mechanisms of the extraordinary Hall effect (see Sec. 1.5.3) are predicted to follow the scaling behavior described in Eq. 1.75. By following the approach proposed by Vilanova *et al.* [VSJ11], we separate the temperature-dependent part of the extraordinary Hall resistivity by subtracting the low temperature data from the high temperature data, which can be expressed as follows [VSJ11]:

$$\begin{aligned}&\rho_{\mathrm{xy}}(\mathrm{T_{high}}) - \rho_{\mathrm{xy}}(\mathrm{T_{low}}) = \\ &(\mathrm{a} + 2\sigma^{\mathrm{int-sj}}\rho_{\mathrm{xx0}})\left[\rho_{\mathrm{xxT}}(\mathrm{T_{high}}) - \rho_{\mathrm{xxT}}(\mathrm{T_{low}})\right] \\ &+\sigma^{\mathrm{int-sj}}\left[\rho_{\mathrm{xxT}}(\mathrm{T_{high}})^2 - \rho_{\mathrm{xxT}}(\mathrm{T_{low}})^2\right]. \end{aligned} \tag{4.3}$$

Rescaling the temperature dependent quantities ($\rho_{\mathrm{xy}}(\mathrm{T})$ and $\rho_{\mathrm{xx}}(\mathrm{T})$) using their corresponding values at 50 K allows one to choose $\rho_{\mathrm{xxT}}(\mathrm{T_{low}}) = \rho_{\mathrm{xxT}}(50\,\mathrm{K})$ and to fit the rescaled data with Eq. 4.3.

At last, the coercive field as a function of a constant cryostat temperature was determined for the different materials. The coercive field is defined as the external magnetic field necessary to reverse 50% of the magnetization within a Hall cross, which is indicated by a 50% change of the extraordinary Hall signal (see Fig. 4.5). The data points at each constant cryostat temperature are then calculated as the mean value of the coercive fields measured for positive and negative applied magnetic fields.

4.2.1 Co/Pt Multilayer

The first material consists of the following multilayer composition:

$$\mathrm{Si/SiO_2(220\,nm)/Pt(2\,nm)/\left[Co(0.6\,nm)/Pt(1.4\,nm)\right]_2/Co(0.6\,nm)/Pt(2\,nm)}.$$

The material was deposited on a $\mathrm{Si/SiO_2(220\,nm)}$ substrate by sputtering. An AlN(200 nm) insulating capping layer has been deposited on top. This thermally highly conductive material is suitable to support heat dissipation and therefore Joule heating effects are lowered during the current-induced experiments. The sample structure design is of the type presented in Fig. 4.1(c) with a wire width $\mathrm{w} \approx 500\,\mathrm{nm}$, Hall cross width $W \approx 500\,\mathrm{nm}$ and the length between the Hall contacts $\mathrm{L} \approx 10\,\mu\mathrm{m}$.

The first spin torque measurements on this material were performed by Boulle *et al.* confirming the out-of-plane magnetization by polar magneto-optical Kerr effect measurements. Furthermore, the saturation magnetization was determined as $\mathrm{M_S} = 1.4 \cdot 10^6\,\mathrm{A\,m^{-1}}$ at 300 K and an effective easy-axis anisotropy $\mathrm{K_{eff}} = 2.5 \cdot 10^5\,\mathrm{J/m^3}$ has been measured [Bou+08]. Assuming an exchange constant $\mathrm{A_{ex}} = 1.6 \cdot 10^{-11}\,\mathrm{J\,m^{-1}}$[Met+07] allows one to estimate the domain wall width λ according to Eq. 1.39: $\lambda_{\mathrm{Co/Pt}} \approx 6.3\,\mathrm{nm}$.

The longitudinal resistivity ρ_{xx} as a function of the cryostat temperature is shown in Fig. 4.6(a). Here, the resistivity is linearly decreasing with decreasing temperature fitting to the expected metallic behavior. At low temperatures ($< 50\,\mathrm{K}$) the resistance converges towards the residual resistivity ρ_{xx0}.

The rescaled transversal resistivity $\rho_{\mathrm{xy}} - \rho_{\mathrm{xy}}(50\,\mathrm{K})$ as a function of the rescaled longitudinal resistivity $\rho_{\mathrm{xx}} - \rho_{\mathrm{xx}}(50\,\mathrm{K})$ is shown in Fig. 4.6(b). Since the experimental temperature is close to the Curie temperature T_C, which ranges from approximately 400 K to 500 K [Met+07; Sug+92], we can assume that the saturation magnetization only remains constant at low temperatures. At high temperatures (large longitudinal resistivities) a decreasing saturation magnetization would lead to a decrease of the transversal resistivity since the extraordinary Hall effect is directly proportional to the magnetization.

To determine the temperature (longitudinal resistivity) range for which the saturation magnetization probably remains constant, we use a linear function $\rho_{\mathrm{xy}}^{\mathrm{linear}}$ to fit the rescaled

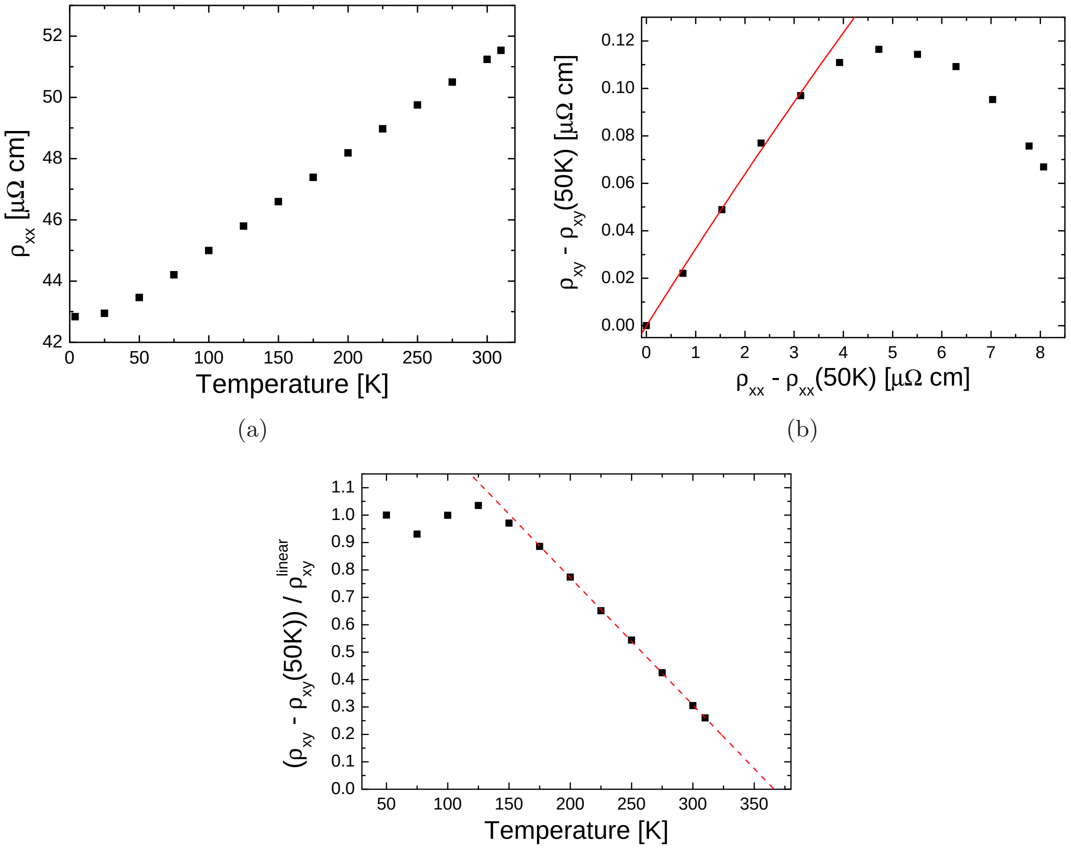

(a)

(b)

(c)

Figure 4.6: Measurement of (a) the longitudinal resistivity ρ_{xx} as a function of a constant cryostat temperature and (b) $\rho_{\mathrm{xy}} - \rho_{\mathrm{xy}}(50\,\mathrm{K})$ as a function of $\rho_{\mathrm{xx}} - \rho_{\mathrm{xx}}(50\,\mathrm{K})$ using a Co/Pt multilayer nanowire. The red solid line shows the fit using Eq. 4.3 taking into account the data points for which a constant saturation magnetization is assumed. (c) The ratio $(\rho_{\mathrm{xy}} - \rho_{\mathrm{xy}}(50\,\mathrm{K}))/\rho_{\mathrm{xy}}^{\mathrm{linear}}$ as a function of the constant cryostat temperature. The red dashed line indicates the linear extrapolation of the data in the range of 175 K to 310 K.

transversal resistivity data in the temperature range of 50 K to 100 K, where the saturation magnetization is assumed to be constant. Next, we plot the ratio $(\rho_{\mathrm{xy}} - \rho_{\mathrm{xy}}(50\,\mathrm{K}))/\rho_{\mathrm{xy}}^{\mathrm{linear}}$ as a function of the constant cryostat temperature (see Fig. 4.6(c)). Although, neither the Bloch $-\,\mathrm{T}^{\frac{3}{2}}$ law nor the $(\mathrm{T_c} - \mathrm{T})^{\beta}$ law fit the experimental data well. A linear extrapolation (see Fig. 4.6(c)) of the data in the range of 175 K to 310 K results in an intercept with the X-axis at about 366 K being smaller than the Curie Temperature (400 K to 500 K) reported previously [Met+07; Sug+92]. However, a decreasing saturation magnetization cannot be excluded.

A comparable behavior has been found by Sugimoto *et al.* [Sug+92] in the case of a Co/Pt multilayer material with similar Co thicknesses. Here, a strong decrease of the saturation magnetization of about 50% below 300 K has been observed. Therefore, the following data analysis concerning the determination of the contributions to the extraordinary Hall effect is restricted to the data points in the temperature range of 50 K to 150 K, for which the ratio $(\rho_{\mathrm{xy}} - \rho_{\mathrm{xy}}(50\,\mathrm{K}))/\rho_{\mathrm{xy}}^{\mathrm{linear}}$ remains larger than 0.9.

Following the approach introduced in Sec. 4.2, we fit the rescaled transversal resistivity $\rho_{\mathrm{xy}} - \rho_{\mathrm{xy}}(50\,\mathrm{K})$ using the Eq. 4.3. The deduced coefficients a and $\sigma^{\mathrm{int-sj}}$ are shown in Fig. 4.13.

4.2.2 Pt/CoFeB/Pt

A soft magnetic material based on CoFeB is composed of:

$$\mathrm{Si/SiO_2/Pt(3\,nm)/Co_{60}Fe_{20}B_{20}(0.6\,nm)/Pt(2\,nm)}.$$

The structure for the measurements was chosen to be of the type shown Fig. 4.1(c). The hysteresis loops measured using perpendicular external magnetic fields reveal a square shape proving the out-of-plane magnetization configuration, which has been confirmed by magneto-optical Kerr effect measurements of Boulle *et al.* [Bou+09].

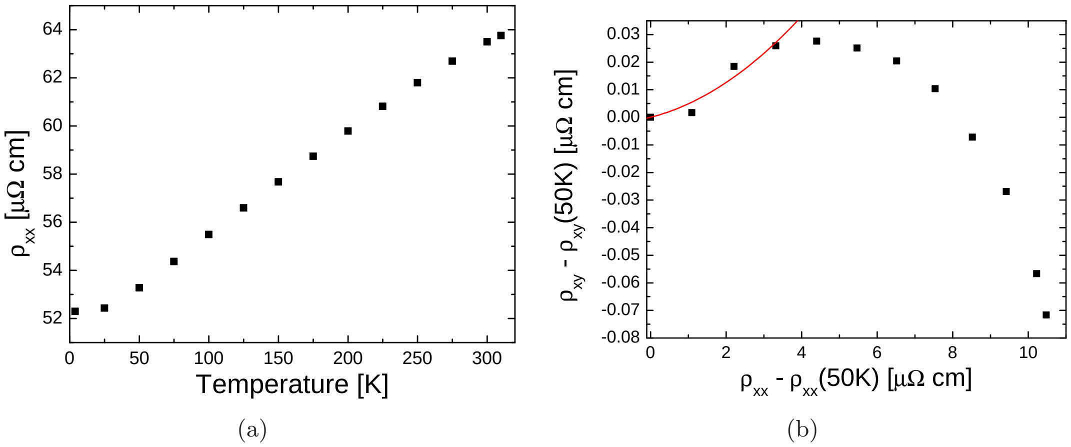

(a) (b)

Figure 4.7: Measurement of (a) the longitudinal resistivity ρ_{xx} as a function of a constant cryostat temperature and (b) $\rho_{\mathrm{xy}} - \rho_{\mathrm{xy}}(50\,\mathrm{K})$ as a function of $\rho_{\mathrm{xx}} - \rho_{\mathrm{xx}}(50\,\mathrm{K})$ using a Pt/CoFeB/Pt nanowire. The red solid line shows the fit using Eq. 4.3 taking into account the data points for which a constant saturation magnetization is assumed.

The measurements presented in Fig. 4.7 reveal a more complex behavior compared to the results of the Co/Pt multilayer material. A change of the sign occurs at about 250 K. Assuming again a decreasing saturation magnetization at higher temperatures, we follow the same approach as used before on the Co/Pt multilayer material to extrapolate the variation of the saturation magnetization with temperature. As a result, we restrict the data analysis of the extraordinary Hall resistivity to temperatures ranging from 50 K to 125 K for which we assume a constant saturation magnetization. The results of the fits using Eq. 4.3 are shown in Fig. 4.13.

4.2.3 Co/Ni Multilayer

The next material is a multilayer stack with the following composition:

$$\mathrm{Si/SiO_2/Ta(2\,nm)/Cu(6\,nm)/\left[Ni(0.6\,nm)/Co(0.2\,nm)\right]_5/Ru(3\,nm)/Ta(5\,nm)}.$$

Similar to the Co/Pt multilayer material a Si/SiO$_2$ substrate has been used, but no additional thermally conductive material was deposited. Two sample batches using this material composition have been produced, one using the lift-off process and the other one using the etching process. The structure type used for the measurements below is shown in Fig. 4.1(b). Hysteresis loop measurements on both sample batches using external magnetic fields perpendicular to the surface reveal square hysteresis loops confirming an out-of-plane magnetization configuration.

Until now, several other groups have determined the basic material parameters of Co/Ni multilayer stacks with comparable material compositions and layer thicknesses [Ued+11]: $\mathrm{M_S} \approx 6.68 \cdot 10^5\,\mathrm{A\,m^{-1}}$ and $\mathrm{K_{eff}} \approx 4.2 \cdot 10^5\,\mathrm{J/m^3}$. The assumption of the exchange constant $\mathrm{A_{ex}} = 1.6 \cdot 10^{-11}\,\mathrm{J\,m^{-1}}$[Met+07] leads to a domain wall width $\lambda_{\mathrm{Co/Ni}} \approx 6.2\,\mathrm{nm}$.

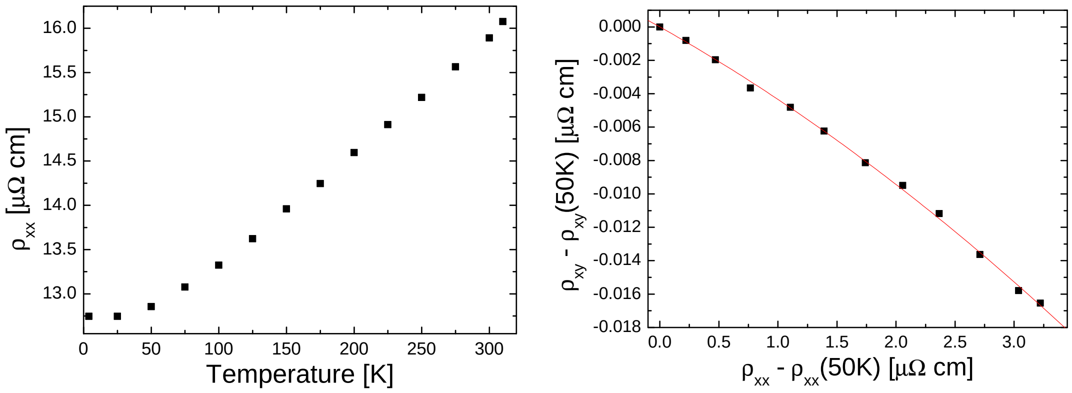

(a)

(b)

Figure 4.8: Measurement of (a) the longitudinal resistivity ρ_{xx} as a function of a constant cryostat temperature and (b) $\rho_{\mathrm{xy}} - \rho_{\mathrm{xy}}(50\,\mathrm{K})$ as a function of $\rho_{\mathrm{xx}} - \rho_{\mathrm{xx}}(50\,\mathrm{K})$ using a Co/Ni multilayer nanowire (preparation method: etching). The red solid line shows the fit using Eq. 4.3 taking into account the data points for which a constant saturation magnetization is assumed.

In the case of the structure processed by etching referred to as Co/Ni sample A, the dimensions are chosen as: wire width w $\approx$ 800 nm, Hall cross width $W \approx$ 590 nm and the length between the Hall contacts L $\approx$ 650 nm. The results of the longitudinal ρ_{xx} resistivity and rescaled transversal resistivity $\rho_{\mathrm{xx}} - \rho_{\mathrm{xx}}(50\,\mathrm{K})$ are shown in Fig. 4.8. Here, the longitudinal resistivity progresses similar to the Co/Pt multilayer material fitting to the expected metallic behavior.

The rescaled transversal resistivity monotonously decreases with increasing rescaled longitudinal resistivity. In contrast to the Pt-based multilayer materials, we assume a constant saturation magnetization over the whole measurement temperature (50 K to 310 K) according to the measurements by Hernando *et al.* [Her+96] reporting high Curie temperatures ranging from 600 K to 700 K depending on the Ni layer thickness. The results of the fits using Eq. 4.3 are shown in Fig. 4.13.

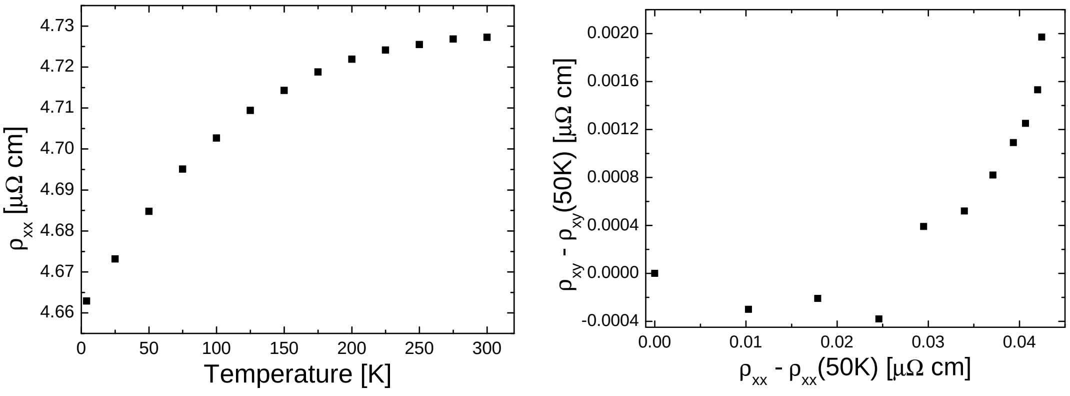

(a) (b)

Figure 4.9: Measurement of (a) the longitudinal resistivity ρ_{xx} as a function of a constant cryostat temperature and (b) $\rho_{\mathrm{xy}} - \rho_{\mathrm{xy}}(50\,\mathrm{K})$ as a function of $\rho_{\mathrm{xx}} - \rho_{\mathrm{xx}}(50\,\mathrm{K})$ using a Co/Ni multilayer nanowire (preparation method: lift-off).

In the case of the structures processed by lift-off referred to as Co/Ni sample B, the dimensions are chosen as: wire width w $\approx$ 330 nm, Hall cross width $W \approx$ 330 nm and the length between the Hall contacts L $\approx$ 750 nm. The results of the longitudinal ρ_{xx} resistivity and rescaled transversal resistivity $\rho_{\mathrm{xx}} - \rho_{\mathrm{xx}}(50\,\mathrm{K})$ are shown in Fig. 4.9. Note, that the longitudinal resistivity is deduced from a different structure of the same sample batch. The measured results of the resistivities differ from the samples produced by the etching process. In the case of the longitudinal resistivity, a monotonous decrease with decreasing temperature can be seen, but no convergence towards the residual resistivity ρ_{xx0} in the low temperature regime, which does not fit to the expected metallic behavior. Furthermore, the residual resistivity ratio $\frac{\rho_{300\,\mathrm{K}}}{\rho_{4.3\,\mathrm{K}}}$ is close to one indicating a bad quality of the samples used. Since the longitudinal resistivity is a crucial parameter of the extraordinary Hall effect, repetitions of the measurements on further samples are required before an appropriate analysis can be performed.

4.2.4 Co/Ni-CoFeB Multilayer

The following sample is based on a Co/Ni multilayer stack plus an additional CoFeB capping layer:

$$\mathrm{Si/SiO_2/Ta(3\,nm)/Pt(3\,nm)/\left[Co(0.2\,nm)/Ni(0.6\,nm)\right]_3/CoFeB(0.3\,nm)/Pt(3\,nm).}$$

The deposition has been done on a Si/SiO$_2$ substrate. The structure type is shown in Fig. 4.1(d).

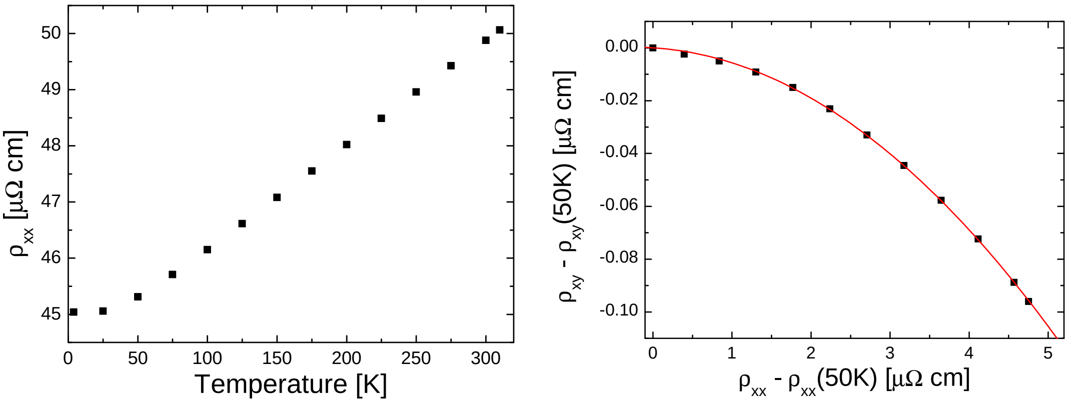

(a) (b)

Figure 4.10: Measurement of (a) the longitudinal resistivity ρ_{xx} as a function of a constant cryostat temperature and (b) $\rho_{\mathrm{xy}} - \rho_{\mathrm{xy}}(50\,\mathrm{K})$ as a function of $\rho_{\mathrm{xx}} - \rho_{\mathrm{xx}}(50\,\mathrm{K})$ using a Co/Ni-CoFeB multilayer nanowire. The red solid line shows the fit using Eq. 4.3 taking into account the data points for which a constant saturation magnetization is assumed.

The measurement results of the longitudinal ρ_{xx} resistivity and rescaled transversal resistivity $\rho_{\mathrm{xx}} - \rho_{\mathrm{xx}}(50\,\mathrm{K})$ are shown in Fig. 4.10. The variation of the longitudinal resistivity with temperature is in agreement with a metallic behavior. The behavior of the transversal resistivity is analog to the Co/Ni multilayer samples produced by etching. Since a high Curie temperature is reported in the case of CoFeB ($> 1300\,\mathrm{K}$) [Nag+00], we assume again a constant saturation magnetization over the whole measurement temperature and perform the data analysis analogously to the Co/Ni multilayer material. The results of the fits using Eq. 4.3 are shown in Fig. 4.13.

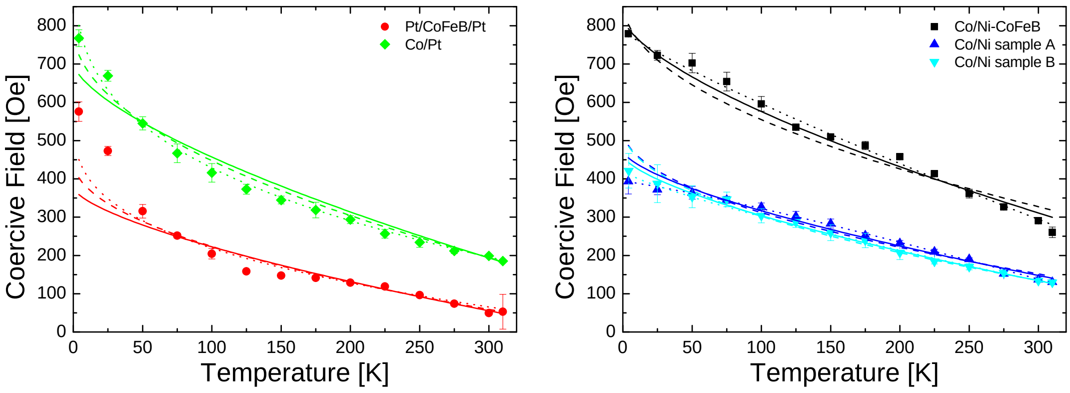

(a) (b)

Figure 4.11: Coercive fields as a function of a constant cryostat temperature for the (a) the Pt-based and (b) the Ni-based material compositions. Each data point represents the mean value of the coercive fields measured for positive and negative fields. The errors are the standard deviations of the mean values. The data is fitted using the temperature dependent function $\mathrm{H_c(T)}$ (see Eq. 4.4) with the critical exponents $\mathrm{m} = \frac{3}{2}$ (solid lines), $\mathrm{m} = 2$ (dashed lines) and a variable m (dotted lines).

4.2.5 Coercive Fields

The coercive fields shown in Fig. 4.11 monotonously decrease with increasing cryostat temperature for all material compositions. However, a difference concerning the slope exists between the Ni-based compositions exhibiting an almost linear slope and the Pt-based compositions revealing a similar decrease only at higher temperatures ($> 100\,\mathrm{K}$). Furthermore, the influence of the CoFeB differs depending on the basic composition of the multilayers. In the case of a Pt-based composition, the coercive fields at higher temperatures are rapidly decreasing compared to the Co/Pt multilayer making it a soft-magnetic material. In contrast, the Ni-based composition shows higher coercive fields over the whole temperature range compared to the 'pure' Co/Ni multilayers. Note, that a direct comparison of the absolute values of the measured coercive fields is impossible, since the wire width, which also affects the coercive field, differs for each material composition.

However, the Pt/CoFeB/Pt multilayer and the 'pure' Co/Ni multilayers exhibit low coercive fields making them suitable candidates for experiments with external domain nucleation using the Oersted field effect. Successful applications of these materials have been demonstrated by several groups [Ued+11; Koy+11; Koy+08; Tan+09].

The solid, dotted and dashed lines in Fig. 4.11 are fits according to a thermal fluctuation model [Liu+08; Zen+02]:

$$H_c(T) = H_0 \left\{ 1 - [25 k_B T / E_0]^{1/m} \right\} \tag{4.4}$$

with the zero-temperature coercivity H_0 and energy barrier E_0. The exponent m is kept either variable or fixed to account for either the normal thermal activation of Stoner-Wohlfarth particles ($m = 2$) or for a non-symmetric energy landscape ($m = 3/2$) [Zen+02; Vic89]. The results of the fits (see Fig. 4.11) are listed in table 4.1. In order to obtain a converging fit using m as a variable, we assumed that the coercive field determined at 4.3 K does not differ much from the zero-temperature coercivity H_0 in the case of Pt/CoFeB/Pt, Co/Ni sample A and Co/Ni sample B.

Material	m	H_0 [Oe]	E_0 [10^{-19} J]
Pt/CoFeB/Pt	3.07 ± 0.4	$575.7(H_c(4.3\,K))$	1.50 ± 0.15
	2	447.8 ± 39.7	1.37 ± 0.10
	3/2	377 ± 34.9	1.31 ± 0.1
Co/Pt	3.38 ± 0.49	1035.4 ± 85.2	2.10 ± 0.09
	2	793.4 ± 20.6	1.81 ± 0.04
	3/2	701.3 ± 25.8	1.68 ± 0.05
Co/Ni-CoFeB	1.17 ± 0.07	789.2 ± 9.9	1.78 ± 0.07
	2	865.5 ± 2.1	2.68 ± 0.16
	3/2	821.1 ± 11.5	2.11 ± 0.06
Co/Ni sample A	0.86 ± 0.03	$393.7(H_c(4.3\,K))$	1.50 ± 0.02
	2	531 ± 2.1	2.03 ± 0.11
	3/2	473.2 ± 13.1	1.81 ± 0.06
Co/Ni sample B	1.25 ± 0.05	$421.1(H_c(4.3\,K))$	1.67 ± 0.03
	2	531.2 ± 10.7	1.86 ± 0.03
	3/2	461.5 ± 6.7	1.73 ± 0.02

Table 4.1: Parameters of the fitted coercive fields.

4.2.6 Discussion

As a first result of the characterization measurements, the deduced energy barrier E_0 from the temperature dependent coercive field measurements is of the same order of magnitude independent on the material composition and sample geometry. The variation of the exponent m does not strongly affect the determined values. Furthermore, the energy barrier E_0 turns out to be in good agreement with results on different ferromagnetic materials deduced by other groups [Dag+07; Him+05].

In the high temperature regime ($T > 50\,K$) a good agreement between the fitted curves using m=2 or m=3/2 and the experimental data is found indicating that normal thermally activated processes dominate. In the case of a non-symmetric energy landscape (m=3/2), the additional thermal energy at higher temperatures supports the domain wall nucleation and motion by providing energy to overcome energy barriers. In general, the fits using a variable exponent m reveal the best agreement to the experimental data over the whole temperature range. Especially at low temperatures, the variation of the coercive field with decreasing temperature is reliably reproduced. The only exception occurs in the case of the Pt/CoFeB/Pt multilayer. The deviation from the m=2 and m=3/2 laws might be explained by further contributions such as interlayer dipolar interactions and/or intrinsic anisotropies such as magnetoelastic, interface and exchange anisotropy [Liu+08].

Next, the residual resistivity defined at the beginning of this section is shown for the aforementioned material compositions in Fig. 4.12. As a first result, the Pt-based compositions reveal higher residual resistivity values than in the case of the bulk values of the pure elements listed in Table 4.2. This increased residual resistivity might arise from the increasing importance of the surface scattering, grain boundaries, and stress, which have been observed by Freitas *et al.* studying the resistivity of Co thin films [Fre+90]. In addition, defects within the material might also become more important the thinner a material is. Here, the material compositions using CoFeB reveal considerably higher residual resistivities due to the amorphous structure [Jen+06].

The 'pure' Co/Ni samples reveal much lower residual resistivities than the other materials. The production method itself seem to have an influence on the residual resistivity. The values found are comparable to the resistivities measured by Freitas *et al.*, who discovered a strong variation of the residual resistivity depending on the Co film production method

Figure 4.12: Residual resistivity ρ_{xx0} approximated as the longitudinal resistivity at 4.3 K for the various material compositions.

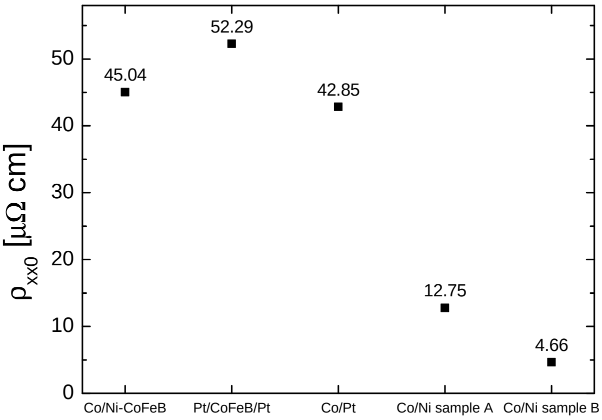

[Fre+90]. Finally, the results of the analysis of the rescaled transversal resistivities will be presented.

As discussed in Sec. 4.2.1, the decreasing extraordinary Hall resistivity at high temperatures in the case of the Pt-based multilayer materials might be explained by the proportionality of the extraordinary Hall effect to the magnetization itself (see Eq. 1.70). In the case of a low Curie temperature T_C, the saturation magnetization would already decrease in this temperature regime resulting in a decreasing extraordinary Hall resistivity. In the presented experiments, this influence could not completely be ruled out since a detailed measurement of the saturation magnetization as a function of temperature for these specific material compositions (Co/Pt and Pt/CoFeB/Pt) are missing. However, the fit of the rescaled transversal resistivity using Eq. 4.3 succeeded for all material compositions in the temperature regimes for which the saturation magnetization can be assumed constant. The deduced coefficients a and $\sigma^{\mathrm{int-sj}}$ are shown in Fig. 4.13 for the different materials. In general, the basic elements, Pt and Ni, seem to have a strong

Element	Resistivity [μΩ cm]	Temperature [K]	Reference
Co (bulk)	13	300	[MP75]
Co (bulk)	0.2	4.3	[Fre+90]
Co (film)	0.54 to 14	4.3	[Fre+90]
Ni (bulk	7.8	300	[MP75]
Pt (bulk)	10		[Míše70]
Fe (bulk)	9.8	300	[MP75]
B (bulk)	$6.1 \cdot 10^8 - 1.7 \cdot 10^{12}$	300	[SHD57]

Table 4.2: Resistivities of the elements

influence since the qualitative shape of the transversal resistivity curves seem similar for both, the Pt-based or the Ni-based compositions, but in direct comparison they differ regarding the slope of the linear term of Eq. 4.3.

A quantitative analysis is given by comparing the order of magnitudes of the coefficients. Here, the $\sigma^{\mathrm{int-sj}}$ values are in the order of $10^{-4}\,(\mu\Omega\,\mathrm{cm})^{-1}$, while the linear coefficient $(\mathrm{a} + 2\sigma^{\mathrm{int-sj}}\rho_{\mathrm{xx0}})$ is in the order of 10^{-2} with ρ_{xx0} in the range of $\approx 10^{1}\,(\mu\Omega\,\mathrm{cm})$. This leads to a skew scattering coefficient a in the range of $\approx 10^{-3}$. Thus neither the skew scattering contribution nor the combined intrinsic and side jump effects are dominating the temperature dependent extraordinary Hall effect.

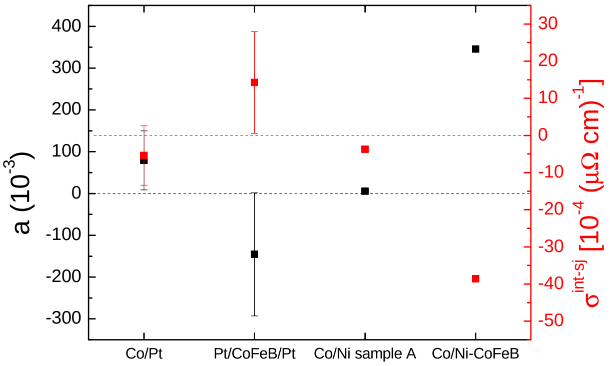

Figure 4.13: Coefficients a and $\sigma^{\mathrm{int-sj}}$ from the fit of the temperature dependent transversal resistivity acquired for the various materials.

However, the resulting coefficients of the 'pure' material compositions (Co/Pt and Co/Ni) are quite similar, while the multilayer materials consisting of CoFeB reveal larger coefficients and even of opposite sign in the case of the Pt-based composition. Here, the use of CoFeB induces a change from a crystalline structure to an amorphous structure possibly resulting in the enhancement of all contributions.

4.3 In-plane Magnetization Configuration

The next material class studied in this work exhibit in-plane magnetization configurations. Amongst the various other in-plane magnetized materials (permalloy, Co, Fe, etc.) the Heusler compounds turn out to be very promising for spintronic applications. A vast variety of properties ranging from semiconductors, superconductors, shape memory alloys to half-metallic ferromagnets are possible by tuning the material compositions. An overview with focus on the structure, properties and possible applications can be found in the review by Graf *et al.* [GPF11]. One of the exceptional properties is the expected high spin polarization P, which theoretically can reach $\mathrm{P} = 1$ making these materials most suitable for current-induced domain wall motion experiments [GPF11].

In this work, preliminary characterization experiments on the following half-metallic Heusler alloy stack were performed:

$$\mathrm{MgO/Cr(10\,nm)/Co_2FeAl_{0.4}Si_{0.6}(15\,nm)/Ru(4\,nm)}.$$

Manganese oxide (MgO) has been used as a substrate, and the Cr seed layer provided the necessary base for the $\mathrm{Co_2FeAl_{0.4}Si_{0.6}}$ to form a $\mathrm{L2_1}$ phase. The post annealing in vacuum (500 °C, 20 min) should induce a strong (001) texture [Rhe11].

A detailed knowledge about the spin structures in these material have been extensively studied by J. Rhensius [Rhe11] using magnetic imaging methods such as photoemission electron microscopy and magnetic force microscopy. The images verify an in-plane magnetization configuration, and the possibility of stable domain wall configurations within ring-shape and wire structures. These domain walls can easily be nucleated in zigzag-wire structures (see Fig. 4.2(a)) or ring structures with a two step field sequence: First, a sufficiently large external in-plane magnetic field is applied under the angle $\varphi = 90^\circ$ as defined in Fig. 4.14. Second, the field is relaxed back to zero leaving either a transverse domain wall or a vortex domain wall in the kinks or bent parts of the wires behind (see Sec. 1.3.1). The goal of the following experiments is to electrically detect the presence of such domain wall structures. In Sec. 1.5 two effects, anisotropic magnetoresistance and planar Hall effect, have been introduced, which are suitable to locally determine the magnetization configuration of materials with

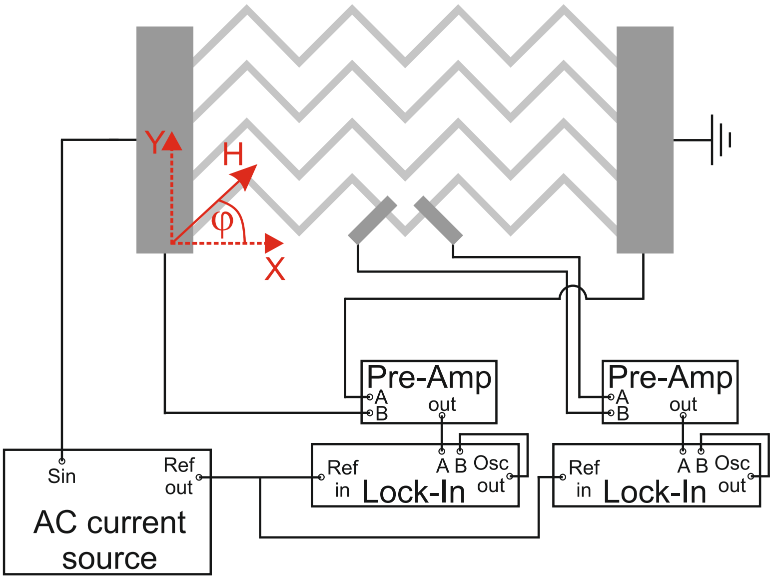

Figure 4.14: Measurement scheme for 2-point and 4-point resistance. The external magnetic field H is applied in-plane under the angle φ. A *Keithley 6221* is used as an AC current source providing also a TTL reference signal to trigger all other devices. The voltages at the Hall cross contacts are measured with high accuracy using *Signal Recovery* Lock-in amplifiers (models: *DSP 7265* or *DSP 7225*). Differential voltage preamplifiers (*SR560*) are used to differentiate the voltages measured in 2-point or 4-point geometry. The amplified output signals are connected to the Lock-in amplifier inputs A. Since, the expected resistance changes are small (a few mΩ), the measured high voltages have to be compensated in order to reduce the voltage ranges of the Lock-in amplifiers. The necessary compensation voltage is provided by the reference outputs of the Lock-in amplifiers.

in-plane magnetization configuration. Successful use of these effects has been shown in experiments using Permalloy nanostructures [Tho+06; Kl03].

The resistance change in the presence of a domain wall is expected to be in the order of a few tenth of a percent of the total resistance (see Sec. 1.5.1) since, the domain wall width is usually small compared to the whole section, which is measured. Therefore, only a small part of the magnetization changes its orientation with respect to the direction of the current flow and causes a change of the anisotropic magnetoresistance. The measurement scheme is based on simple 2-point and 4-point resistance measurements, but an amplification and offset voltage compensation circuit were added to resolve even resistance changes in the mΩ range (see Fig. 4.14). Here, differential voltage preamplifiers (model: SR560) are used to amplify the differential voltages measured either in a 2-point geometry between the outer gold contacts, which are also used for the electrical current injection, or in a 4-point geometry using the contacts enclosing a kink of the zigzag-wire. The Lock-in reference output voltages are then used to compensate the amplified voltages in order to reduce the voltage range of the Lock-ins increasing the sensitivity.

4.3.1 Zigzag-wire Structure

The first structure type is a zigzag-wire as shown in Fig. 4.2(a) with a wire width w $\approx$ 2000 nm. The resistance measurements were performed at 4.3 K. The 2-point resistances are plotted in Fig. 4.15 as a function of the external in-plane magnetic field under various angles φ (see Fig. 4.14). In general, independent of the angle φ, the resistance decreases for high magnetic fields (> 1500 Oe), but an asymmetry exists concerning the field direction (positive or negative field values). In the low field regime (< 1500 Oe), two resistance peaks appear, which seem to vary in height depending on the angle φ.

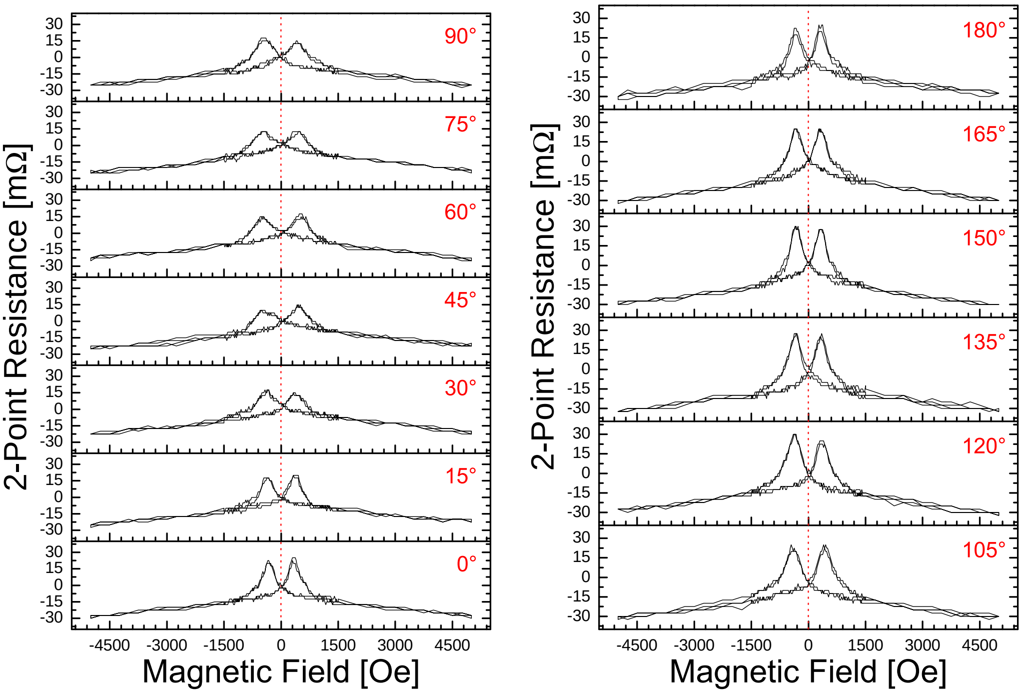

(a)

(b)

Figure 4.15: 2-point resistance measurements performed on the zigzag-wire structure using the gold contacts on each side of the four wires at a constant cryostat temperature of 4.3 K. The external in-plane magnetic field is swept two times from $-5000\,\mathrm{Oe}$ to $5000\,\mathrm{Oe}$ under different angles φ as defined in Fig. 4.14.

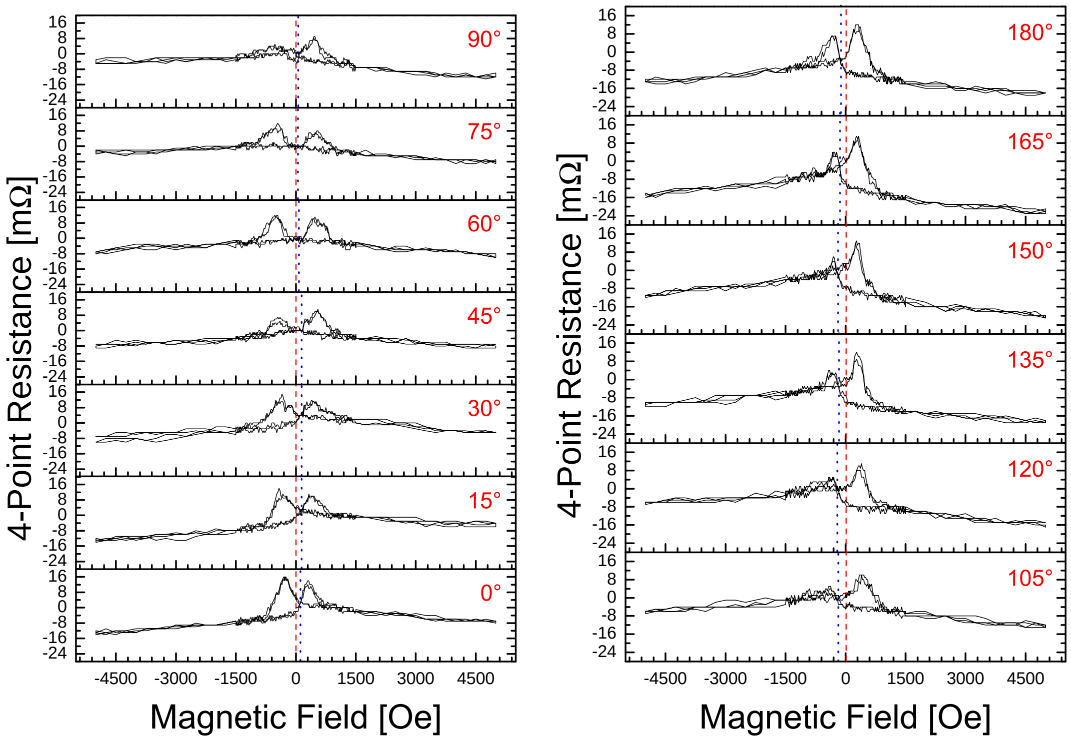

(a) (b)

Figure 4.16: 4-point resistance measurements performed on the zigzag-wire structure using the two gold contacts around a kink at a constant cryostat temperature of 4.3 K. The external in-plane magnetic field is swept two times from $-5000\,\mathrm{Oe}$ to $5000\,\mathrm{Oe}$ under different angles φ as defined in Fig. 4.14. The blue dotted lines indicate the shift of the crossing point between the two peaks by a field H^*, which depends on the angle φ.

The 4-point resistance is measured analogous to the 2-point resistance. The results for the various angles φ are shown in Fig. 4.16. Again the distinct resistance decrease for high external in-plane magnetic fields can be observed. The direct comparison of the measured resistances at two constant field values as shown in Fig. 4.17(a) clearly reveals a constant shift in the resistance independent of the angle φ.

The assumed changes in the peak heights are even more obvious in the 4-point resistance measurements and seem to be strongly depending on the angle φ. Furthermore, a shift of the cross point between both peaks by a field H^* can be observed in either positive or negative applied in-plane magnetic field direction.

To rule out the effect of a domain wall being present in the kink during the field sweeps, we performed a so-called ”mode etoile” measurement. Using this measurement scheme, the 4-point resistance is measured at zero external in-plane magnetic field after performing the field sequence described before to nucleate a domain wall at a kink of a wire. This measurement procedure was repeated three times. The results are shown in Fig. 4.17(b). For all angles φ the values are equally distributed around zero allowing no determination whether a domain wall structure might be present.

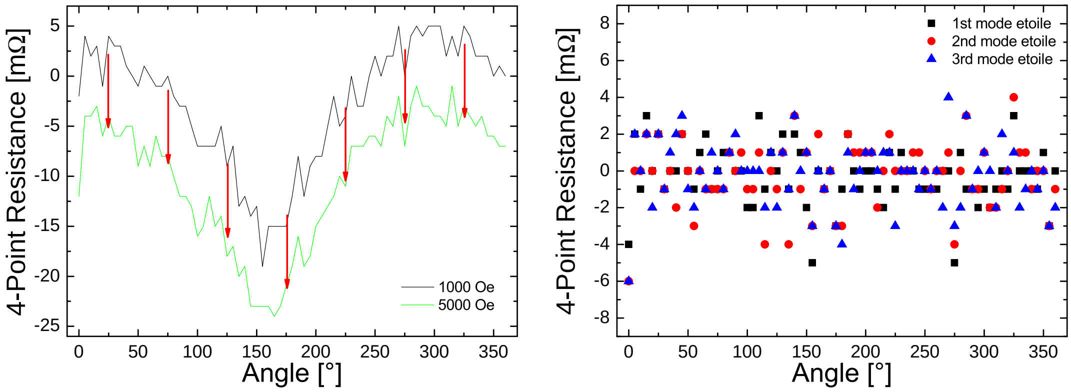

(a) (b)

Figure 4.17: 4-point resistance measurements performed on the zigzag-wire structure using the two gold contacts around a kink at a constant cryostat temperature of 4.3 K. (a) The 4-point resistance values for two different constant external in-plane magnetic fields are plotted as a function of the angle φ. The arrows indicate a constant reduction of the resistance with higher fields independent of the angle φ. (b) Results of the mode etoile measurements to detect the presence of a domain wall within a kink of the zigzag-wire after the domain wall nucleation field sequence.

4.3.2 Rectangular Structure

To further investigate the asymmetry of the resistance changes depending on the angle φ, a simple rectangular structure has been patterned (see Fig. 4.2(b)). The dimensions are as follows: wire width w $\approx$ 1050 nm, Hall cross width W $\approx$ 540 nm and the length between the Hall contacts L $\approx$ 2050 nm. The measurement scheme presented in Fig. 4.14 was adapted with slight changes to fit for the rectangular structure. To avoid the influence of a Hall voltage, each pair of gold contacts in Hall geometry (see Fig. 4.2(b)) were combined outside the cryostat before amplifying the differential voltage.

The acquisition of sufficiently large sets of data including the extension of the experiments to different measurement temperatures required several days. During this time period the sample exhibited resistance changes and an alteration of the magnetization configuration, which is indicated by anisotropic magnetoresistance measurements at a constant cryostat temperature for five different times of the measurement period (see Fig. 4.18). During the times between the measurements, the sample had been heated and cooled between 4.3 K and 310 K, and several external magnetic field sweeps (in- and out-of-plane) had been performed. The reasons for the changes remain unclear since structural changes had not been observed using the scanning electron microscopy when comparing images of before and after the measurement period. Nevertheless, the magnetization seems to have stabilized, which is indicated by a stable signal during the last two time steps. The following results stem from this time period.

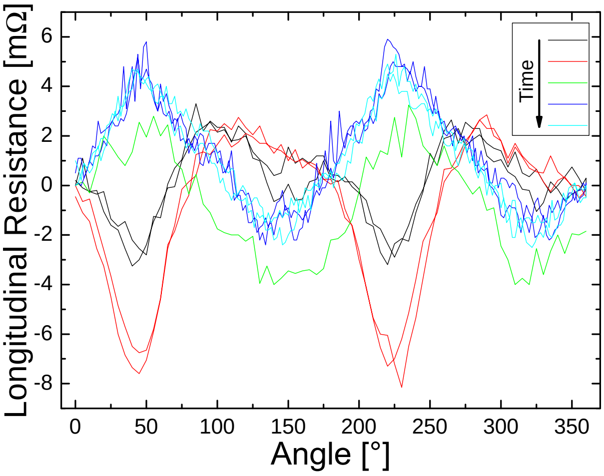

Figure 4.18: Chronology of anisotropic magnetoresistance measurements performed at 4.3 K at different times during the whole measurement period.

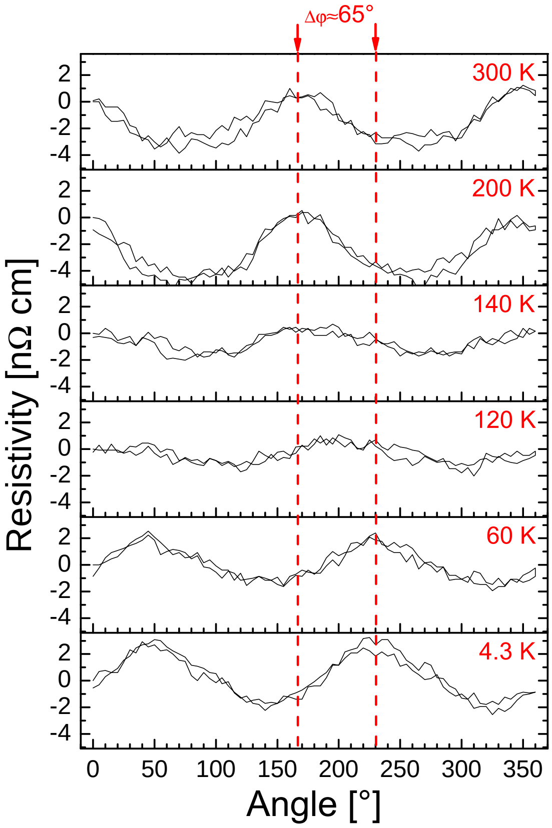

Figure 4.19: Measurement of the anisotropic magnetoresistance for different temperatures using the rectangular structure. The red dashed lines indicate the shift of one maximum by $\Delta\varphi \approx 65^\circ$ between the measurement at 4.3 K and 300 K.

The anisotropic magnetoresistance was measured by applying a constant external in-plane magnetic field (3000 Oe) and rotating it from 0° to 360° and back to 0° at several constant cryostat temperatures ranging from 4.3 K to 300 K. The results of the measurements (see Fig. 4.19) are fitted with the following function according to the theory presented in Sec. 1.5.1:

$$\rho_{\mathrm{AMR}}(\varphi) = \mathrm{a} * \cos(2 * (\varphi + \delta)) + \mathrm{b} * \cos(4 * (\varphi + \delta)) + \mathrm{const.} \tag{4.5}$$

including a phase-shift δ.

The results of the fitting parameters are shown in Fig. 4.21. The main contribution to the anisotropic magnetoresistance comes from the first term, while the higher order term in comparison remains small and almost constant. The coefficient a undergoes a change of sign at about 125 K, which can also be seen in Fig. 4.19. However, no asymmetry concerning the angle φ is observed for the whole temperature range.

At last, the arrangement of the gold contacts in Hall cross geometry allowed the measurement of the transversal resistivity following a measurement scheme similar to the one used for the determination of the extraordinary Hall effects (see Fig. 4.3). A constant external in-plane magnetic field (10000 Oe) was rotated from 0° to 360° and back to 0° at several constant cryostat temperatures ranging from 4.3 K to 300 K. The results of the measurements are shown in Fig. 4.20 and reveal asymmetric amplitudes depending on the angle φ. In order to determine the magnitude of this asymmetry, the data is fitted with a function according to the theory of the planar Hall effect (see Sec. 1.5.2):

$$\rho_{\mathrm{PHE}}(\varphi) = \rho_{\mathrm{s}}\sin(2*(\varphi+\delta)) + \rho^{0}_{\mathrm{as}}\cos(\varphi+\delta) + \rho^{1}_{\mathrm{as}}\cos^{3}(\varphi+\delta) + \mathrm{const.}. \tag{4.6}$$

The symmetric part is described by the coefficient ρ_{s} and the asymmetric parts by the coefficients $\rho^{\mathrm{i}}_{\mathrm{as}}$. A phase-shift δ is used. The results of the coefficients are presented in Fig. 4.22. The temperature range for which ρ_{s} shows a maximum is in coincidence

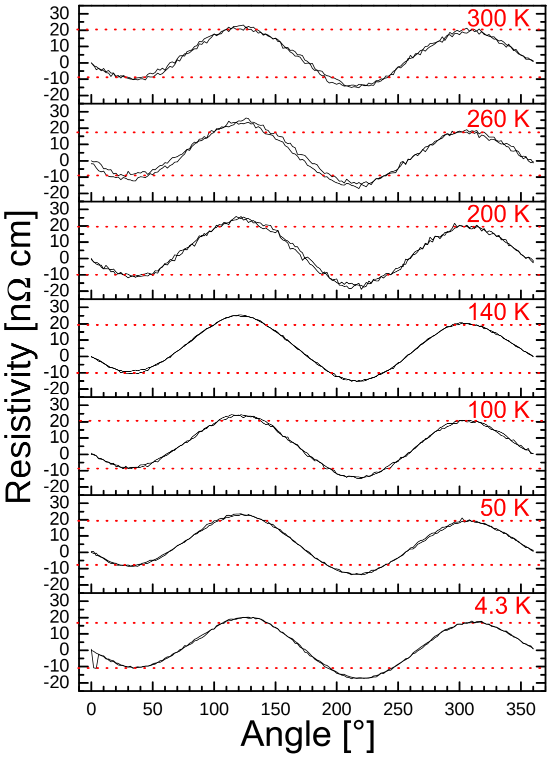

Figure 4.20: Measurement of the planar Hall effect for different temperatures using the rectangular structure. The red dotted lines highlight the asymmetry of the resistivity depending on the angle φ.

with the sign change of the coefficient a of the anisotropic magnetoresistance (see Fig. 4.21(a)).

The asymmetric behavior of the resistivity depending on the angle φ is well described by the asymmetric parts of Eq. 4.6 revealing a negative coefficient ρ^0_{as}. The higher order term is almost zero at low temperatures and remain small even at higher temperatures compared to the ρ^0_{as} values.

4.3.3 Discussion

An explanation for the linearly decreasing resistance observed for high external in-plane magnetic fields might be given by the suppression of magnon scattering and the reduction of spin-flip scattering due to the forced alignment of the spins along the external magnetic field direction. The reduction of scattering events results in a lower longitudinal resistance. These phenomena have also been observed by Schneider *et al.* [Sch+07] while studying Co_2FeSi Heusler films. A detailed understanding of the magnon scattering and spin-flip scattering effects is presented by Raquet *et al.* studying 3d ferromagnets [Raq+01; Raq+02].

The direct comparison between the 2-point and 4-point resistance measurements performed on the zigzag-wire structure shows that the asymmetric behavior of the resistance

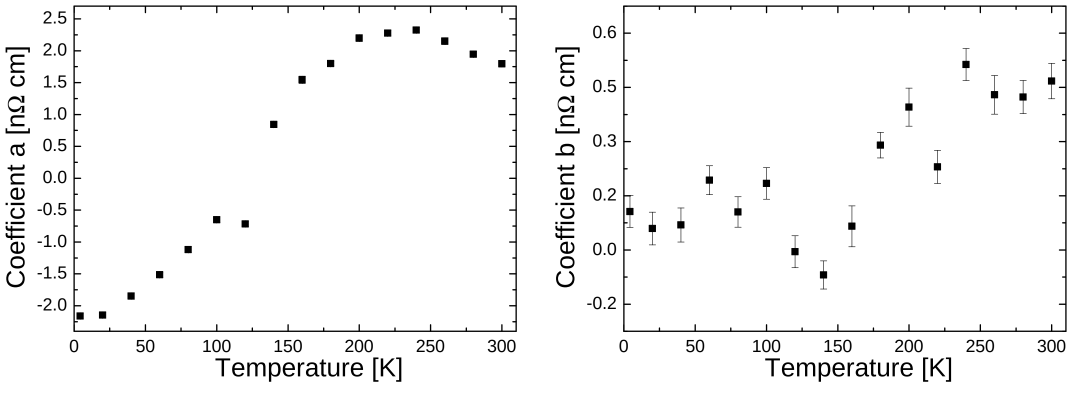

(a) (b)

Figure 4.21: Results of the fits of the temperature dependent anisotropic magnetoresistance measurements using a function $\rho_{\mathrm{AMR}}(\varphi)$ as defined in Eq. 4.5.

depending on the angle φ is a localized effect since its presence in the 4-point measurements, which represents a small magnetic region with a specific orientation in respect to the applied in-plane magnetic field, is more obvious compared to the 2-point measurements. The analysis of the rectangular structure allowed for a detailed study of the transversal voltage revealing a good agreement with the theory of an asymmetric planar Hall effect, which has been extensively studied on other materials such as ferromagnetic semiconductors[He+10; Mud+05; Tan+03], $La_{2/3}Ca_{1/3}MnO_3$[Li+10] and $La_{0.8}Sr_{0.2}MnO_3$[Bas+09]. This additional transverse voltage might affect also the longitudinal resistance measured using the zigzag-wire structure causing the observed asymmetric resistance peaks since the gold contacts used for these measurements are placed across the whole zigzag-wire, but due to bad interfaces one side of the wire might contribute more to the measurement of the voltages than the other side.

The field shift H^*, which depends on the angle φ, might be due to an exchange bias effect, which is present in the case of bilayer or multilayer materials consisting of coexisting magnetic phases. This effect has already been investigated during planar Hall effect measurements on nanocrystalline $Co_{60}Fe_{20}B_{20}$[See+11] and other materials [GPM11]. The presence of such an effect in the measurements could be the result of a coupling between the Heusler alloy and the Cr layer below, which might exhibit an antiferromagnetic magnetization [Sau+88]. Furthermore, oxidation of the material might induce an antiferromagnetic configuration in some regions leading to the exchange bias effect.

The temperature dependent anisotropic magnetoresistance effect measurements reveal a sign change of the coefficient a (see Eq. 4.5) at a temperature of about 125 K. In the same temperature range, the planar Hall effect exhibits a maximum of the coefficient ρ_s representing the magnitude of the symmetric part of Eq. 4.6. A possible explanation might given by temperature-induced strain, which might cause distortions of the $L2_1$-phase and therefore alters the magnetoresistivity tensor $\rho_{ij}(\alpha)$ introduced in Sec. 1.5.1 resulting in a variation of the perpendicular and parallel resistivities ($\rho_\perp$ and $\rho_\|$) [MP75].

For further experiments with focus on current-induced domain wall dynamics, a systematic survey of the crystallographic phases and the resulting magnetization configurations of the half-metallic Heusler alloy and their temperature stability are required.

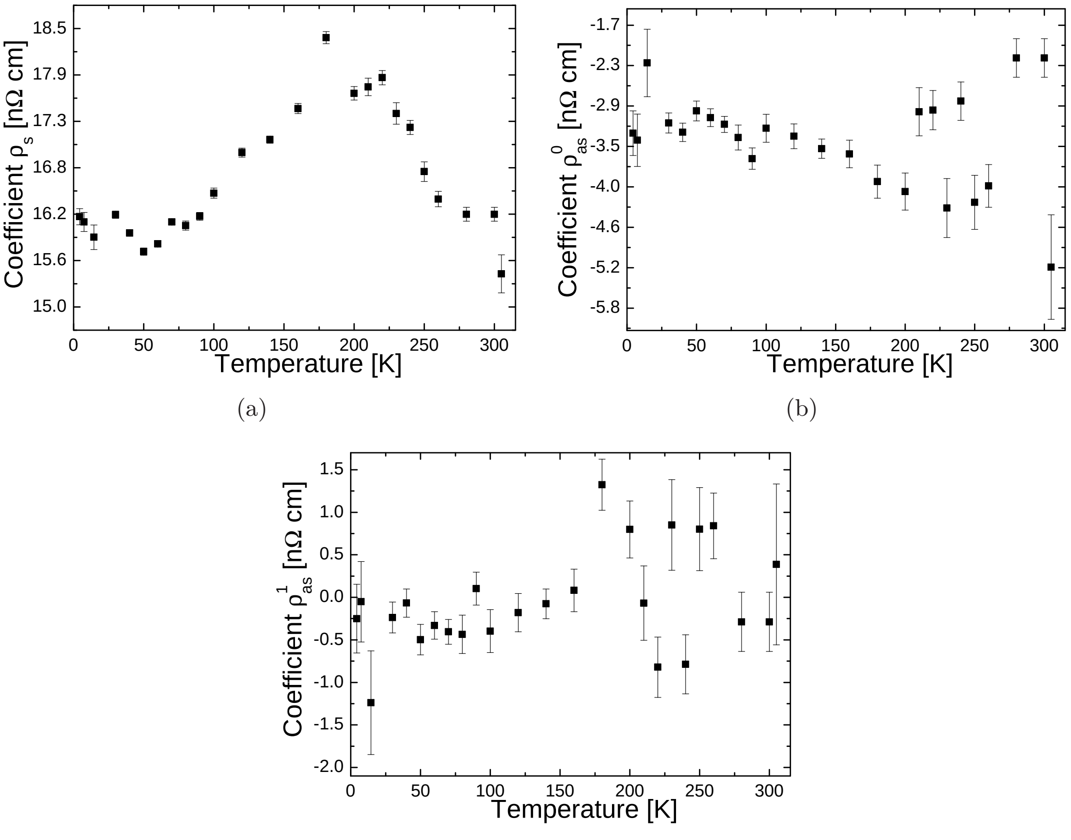

(a)

(b)

(c)

Figure 4.22: Results of the fits of the temperature dependent planar Hall effect measurements using a function $\rho_{\mathrm{PHE}}(\varphi)$ as defined in Eq. 4.6.

5

Experiments on Current-induced Domain Wall Dynamics

This chapter is dedicated to the experiments intended to determine current-induced domain wall dynamics in metallic ferromagnetic multilayer structures. In the first section of this chapter a measurement scheme to separate the spin torque contributions, the Oersted field effect and the Joule heating effect will be introduced. In the following sections, experimental results from different material compositions show its successful application. Each experiment is covered by a separate section consisting of a brief motivation, a description of the measurement technique, the results and a discussion.

The last section is dedicated to a thermally activated domain wall depinning experiment highlighting the importance of probing the reliability of the various theoretical and experimental approaches. Here, we were able to use two independent approaches to extract the non-adiabaticity parameter β (see Sec. 1.4.5) at the same time on one sample.

5.1 Separating the Acting Torques

The approach to separate the contributions to current-induced domain wall dynamics (see Sec. 1.4.1) is based on the measurement of the domain wall depinning field under the influence of a charge and spin current. In general, the depinning field can be expressed as a sum of the spin torque contribution H_{ST}, the Oersted field H_{Oe} and the Joule heating effect $\mathrm{H}_{\mathrm{Joule}}$:

$$\mathrm{H}_{\mathrm{dep}} = \mathrm{H}_{\mathrm{ST}} + \mathrm{H}_{\mathrm{Oe}} + \mathrm{H}_{\mathrm{Joule}}. \tag{5.1}$$

For all these effects, one can find distinct symmetries depending on the local magnetization configuration ($\mathrm{M}_{\pm}$) and the polarity of the injected charge current ($\mathrm{I}_{\pm}$) (see Fig. 5.1):

1. **Spin torque**: As formerly introduced in Sec. 1.4.1, the adiabatic and non-adiabatic spin torque are independent of the initial magnetization configuration. The direction of the domain wall motion v_{ST} indicated in Fig. 5.1 is only determined by the polarity of the injected charge current. This relation can be written as:

$$\mathrm{H}_{\mathrm{ST}}(\mathrm{I}_+, \mathrm{M}_+) = \mathrm{H}_{\mathrm{ST}}(\mathrm{I}_+, \mathrm{M}_-) = -\mathrm{H}_{\mathrm{ST}}(\mathrm{I}_-, \mathrm{M}_+) = -\mathrm{H}_{\mathrm{ST}}(\mathrm{I}_-, \mathrm{M}_-). \tag{5.2}$$

2. **Oersted field effect**: The direction of the domain wall motion v_{Oe} indicated in Fig. 5.1 is determined by both the initial magnetization configuration and the polarity of the injected charge current. Its effect is inverted when either the polarity of the charge current or the magnetization configuration is reversed. An expression for this behavior is given by:

$$\mathrm{H}_{\mathrm{Oe}}(\mathrm{I}_+, \mathrm{M}_+) = -\mathrm{H}_{\mathrm{Oe}}(\mathrm{I}_+, \mathrm{M}_-) \text{ and } \mathrm{H}_{\mathrm{Oe}}(\mathrm{I}_+, \mathrm{M}_+) = -\mathrm{H}_{\mathrm{Oe}}(\mathrm{I}_-, \mathrm{M}_+). \tag{5.3}$$

3. **Joule heating effect**: Increasing current density leads to heating thus lowering the depinning field independently of the polarity of the injected charge current and of the magnetization configuration ($\mathrm{H}_{\mathrm{Joule}}(|\mathrm{I}|, |\mathrm{M}|)$).

The separation of the contributions can be achieved by measuring the domain wall depinning field for all combinations of initial magnetization configuration ($\mathrm{M}_{\pm}$) and current polarity ($I_\pm$). The spin torque contribution can be calculated as:

$$H_{ST} = \frac{[H_{dep}(I_+, M_+) - H_{dep}(I_-, M_+)] + [H_{dep}(I_+, M_-) - H_{dep}(I_-, M_-)]}{4} \tag{5.4}$$

and the Oersted field contribution is given by:

$$H_{Oe} = \frac{[H_{dep}(I_+, M_+) - H_{dep}(I_-, M_+)] - [H_{dep}(I_+, M_-) - H_{dep}(I_-, M_-)]}{4}. \tag{5.5}$$

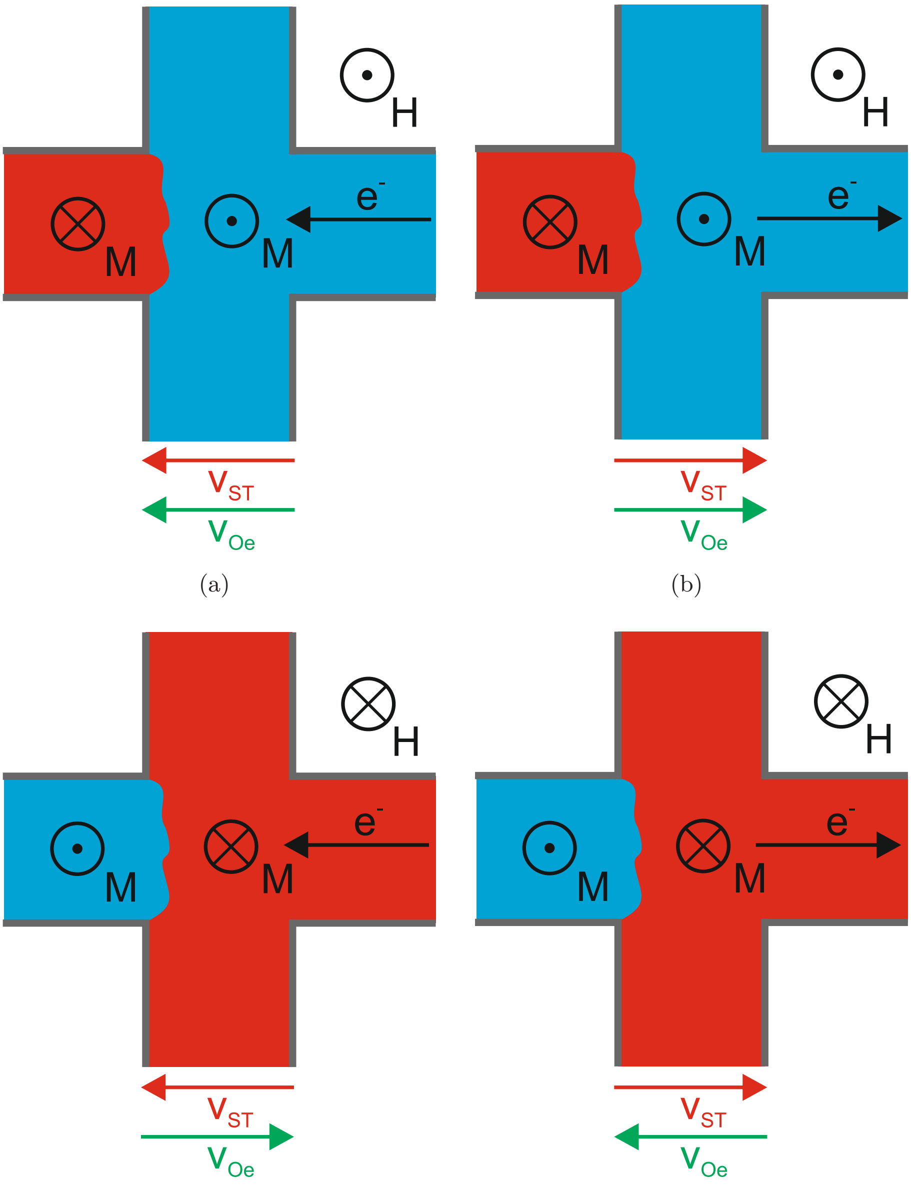

(a) (b) (c) (d)

Figure 5.1: Schematics of the directions of domain wall motion due to the injection of a charge current causing the spin torque (v_{ST}) and the Oersted field effect (v_{Oe}) as indicated in the sketches (a) to (d). In each case, the direction of the magnetic field H is chosen to move the domain wall to the left. The domain wall is assumed to be pinned at the lower left edge of the Hall cross.

5.2 Non-adiabatic Spin Torque in Co/Pt Multilayer Nanowires

The first material composition used for current-induced domain wall motion experiments is the Co/Pt multilayer material described in Sec. 4.2.1. This material is a promising candidate for spintronic applications since a strong magnetization gradient (narrow domain wall width $\lambda \approx 6.3\,\mathrm{nm}$) is present for which theory predicts a strong contribution from the non-adiabatic spin torque. In the following section, a measurement scheme to determine the domain wall depinning field as a function of the injected current density will be presented. The structure used is similar to the geometry presented in Fig. 4.1(c) with a wire width $\mathrm{w} \approx 290\,\mathrm{nm}$. Together with the approach presented in the previous section, we are able to separate the Oersted field effect and the spin torque contribution. Furthermore, the non-adiabaticity parameter β will be determined.

The results shown in this section have been published in Applied Physics Letters [Hei+10].

5.2.1 Measurement Technique

The out-of-plane magnetization configuration of the Co/Pt multilayer material allows one to use the extraordinary Hall effect to detect locally the presence of a domain wall within a Hall cross with high spatial resolution (see Sec. 1.5.3). The measurement scheme is presented in Fig. 5.2. A small alternating current ($\approx 2\,\mu\mathrm{A}$) is generated by the Lock-In reference output ($1\,\mathrm{V}$) and a $510\,\mathrm{k\Omega}$ resistor in series with the sample. The extraordinary Hall voltages are then measured with high accuracy using the Lock-In amplifiers. The pulse-generator is directly connected to the sample, which is grounded using a $50\,\Omega$ resistor. This arrangement of resistances enables the use of an oscilloscope to perform a 4-point resistance measurement in order to deduce the temperature increase during the pulse injection. Therefore, the voltage drop at the $50\,\Omega$ resistor allows one to calculate the current density flowing through the wire. The 2-point and 4-point resistances can then be determined from the voltage differences between the contacts 1-4.

Prior to the current injection, a domain wall needs to be reproducibly placed within the Hall cross. At a constant cryostat temperature $\mathrm{T}_{\mathrm{cryo}} = 100\,\mathrm{K}$, the field driven hysteresis loops revealed plateaus during the magnetization reversal processes. These

Figure 5.2: Measurement scheme for the detection of current-induced domain wall motion. The magnetization reversal within a Hall cross structure is detected using the extraordinary Hall effect. A small alternating current of a few µA is applied in order to measure the extraordinary Hall voltages with high accuracy using Lock-In amplifiers. The pulse generator is either directly connected to the sample or via a Bias-Tee located at the position marked by the red circle. The additional 50 Ω resistor is used to measure the injected current through the wire by using an oscilloscope. The measurement of the voltage differences using the contacts 1-4 allows one to determine the 2-point and 4-point resistance change during the pulse injection.

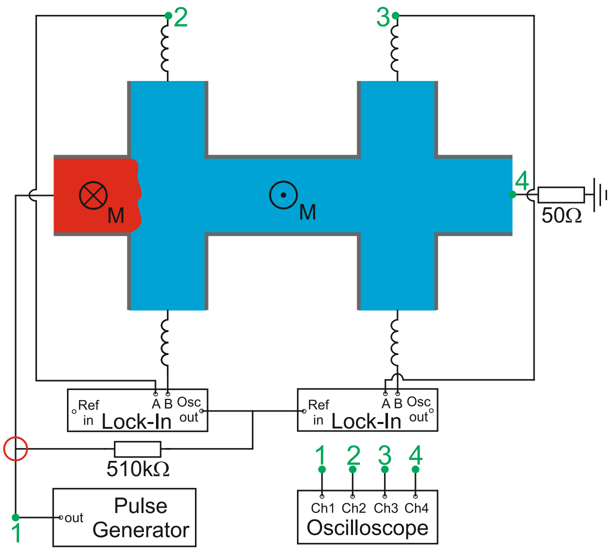

plateaus can be attributed to the fact that a domain wall enters a Hall cross, but stays pinned, e.g. at defects, until a sufficiently large magnetic field is applied to overcome the pinning barrier. The following field sequence was then used to prepare a domain wall with both magnetization configurations: First, the wire is saturated by an external out-of-plane magnetic field (see Fig. 5.3(a), sketch I or III). Afterwards, the field is relaxed to zero and then increased in the opposite field direction until a 5% change of the extraordinary Hall signal is observed, indicating that a domain wall has entered the Hall cross. Again the field is relaxed to zero, while the domain wall stays pinned. This pinning is reflected by the constant extraordinary Hall signal (see Fig. 5.3(a), sketch II and IV).

To determine the domain wall depinning field, the external out-of-plane magnetic field is increased in steps of 5 Oe until the extraordinary Hall signal passes the threshold value of 10% (90%) in the case of positive (negative) applied out-of-plane magnetic fields. After each field step a single 50 µs pulse with a slow rise time of 18 µs is injected into the wire. For the example shown in Fig. 5.3(a), we injected current pulses with a current density $\mathrm{J} = 1.02 \cdot 10^{10}\,\mathrm{A/m^2}$. This measurement procedure was repeated for both magnetization configurations and a variety of current densities. The absolute value

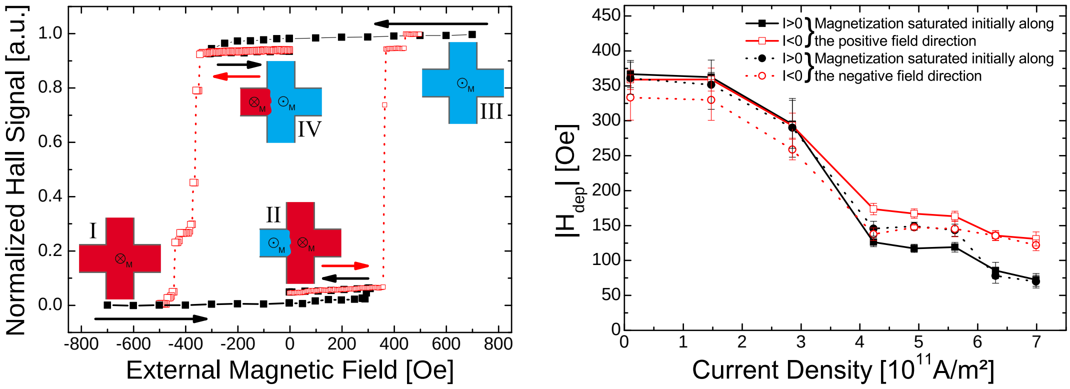

(a)

(b)

Figure 5.3: (a) Normalized Hall signal as a function of the external out-of-plane magnetic field at a constant cryostat temperature $T_{cryo} = 100\,K$. The sketches show the magnetization configuration $M_\pm$ during the domain wall preparation (solid lines, filled squares) and the domain wall depinning by single pulses with a current density of $J = 1.02 \cdot 10^{10}\,A/m^2$ (dotted lines, open squares). (b) The absolute value of the depinning field as a function of the injected current density for both initial magnetization configurations and both current polarities. Each data point represents the mean value of H_{dep} averaged over at least eight repetitions. The error bars represent the corresponding standard deviations. (from Ref. [Hei+10])

of the depinning field as a function of the injected current density J is shown in Fig. 5.3(b).

5.2.2 Results

The measured depinning fields stay almost constant for low current densities, but decrease rapidly at higher current densities independent of the current polarity or initial magnetization configuration. This behavior can be attributed to the Joule heating effect. Nevertheless, an obvious splitting between both current polarities occur for current densities exceeding $4 \cdot 10^{11}\,A/m^2$, which can be attributed to either spin torque or Oersted field effects (see Fig. 5.3(b)). Combining all four sets of measurements following the approach presented in Sec. 5.1 allows us to separate the spin torque contribution and the Oersted field effect. The estimates of these contributions are shown in Fig. 5.4.

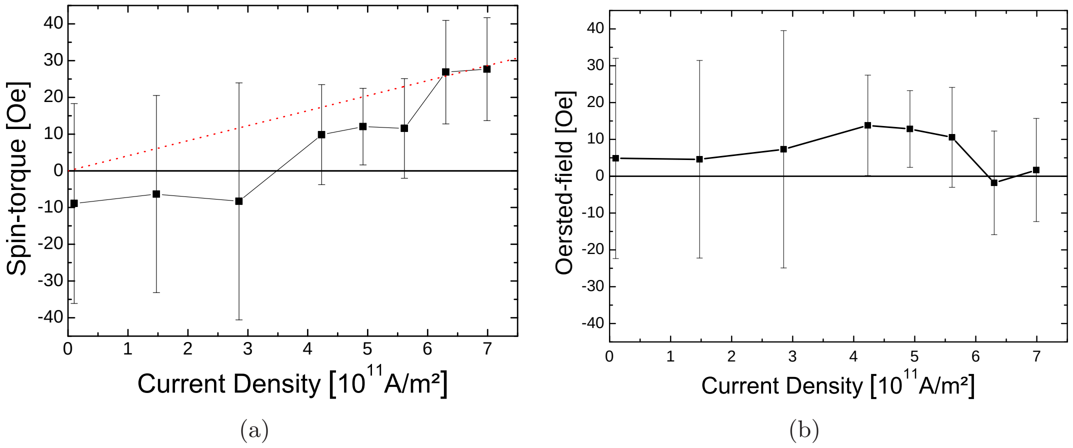

(a)

(b)

Figure 5.4: The deduced spin torque contribution (a) and Oersted field effect (b). The efficiency ϵ is deduced from a linear fit (red, dotted line) using the the data points with the lowest Oersted field effect and the origin since zero current density causes zero spin torque. (from Ref. [Hei+10])

Our results show that the spin torque contribution increases with increasing current density. The largest values, of more than 25 Oe, are reached for current densities larger than $6 \cdot 10^{11}\,\mathrm{A/m^2}$. The Oersted field effect stays close to zero over the whole range of injected current densities.

5.2.3 Discussion

The negligible contribution from the Oersted field effect might be explained by the narrow wire width for which the net force arising from the Oersted field effect is almost zero (see Sec. 1.4.1) and therefore too small to help the domain wall to overcome the pinning barrier. Additionally the Oersted field effect would only be efficient if the pinning of the domain wall occurs at the edges of the wire, where the Oersted field effect would be largest.

Concerning the spin torque contribution, two torques have to be considered: the adiabatic and the non-adiabatic spin torque. As regards the adiabatic spin torque, calculations of the necessary critical current density (see Sec. 1.4.1), which have been performed by Boulle *et al.* on the same Co/Pt material [Bou+08], reveal a much higher current density ($2.1 \cdot 10^{12}\,\mathrm{A/m^2}$) than used in the present experiment. Furthermore, the monotonous increase of the spin torque effect with increasing current density does not fit to the expected adiabatic torque behavior, where a step-like variation at a critical current density is expected. Hence, we conduct that the non-adiabatic spin torque dominates in these Co/Pt multilayer nanowires.

Current-field Equivalence

A quantitative description of the non-adiabatic spin torque contribution is given by the non-adiabaticity parameter β. Following the current-field equivalence approach introduced in Sec. 1.4.5, we determine the efficiency $\epsilon = \beta \frac{\mathrm{P}\hbar}{2\mathrm{eM_S}\lambda}$, which is defined as the slope $|\Delta\mathrm{H}/\Delta\mathrm{J}|$. For the linear fit, we take into account only the values of the two highest injected current densities for which the Oersted field contribution is zero. Additionally we use the origin of the plot since zero current density causes zero spin torque. The resulting efficiency is $\epsilon = (2.49 \pm 0.2) \cdot 10^{-15}\,\mathrm{Tm^2/A}$. The material parameters used to calculate β are: spin polarization of the current $\mathrm{P} = 0.46$ (assumed to be similar to pure Co), saturation magnetization $\mathrm{M_S} = 1.4 \cdot 10^6\,\mathrm{A\,m^{-1}}$ [Bou+08] and domain wall width $\lambda = 6.3\,\mathrm{nm}$ (see Sec. 4.2.1). The resulting non-adiabaticity parameter is $\beta \approx 0.24$, which almost doubles the Gilbert damping constant $\alpha \approx 0.15$ [Bar+07].

It should be noted that the measurements were performed at a constant cryostat temperature $\mathrm{T_{cryo}} = 100\,\mathrm{K}$. As can be seen in Fig. 5.3(b) Joule heating effects lead to a rapid reduction of the depinning field with increasing current density indicating a change of the sample temperature during the current pulse injection. Previous measurements on 530 nm wide wires revealed a temperature increase for current densities larger than $6 \cdot 10^{11}\,\mathrm{A\,m^{-1}}$ of more than 200 K. The current densities used in the present experiment to determine β are of the same order of magnitude. Note that a lower current is needed in the case of our narrower wire structure to produce the same current density. Therefore, less power is produced resulting in less heating. Since, the heat dissipation is reduced due to the smaller surface compared to the wider wire, the effect of lower power might be compensated, resulting in a similar temperature increase of about 200 K. This could lead to a temperature increase of our sample up to 300 K during the injection of the highest current densities allowing us to compare our deduced $\beta \approx 0.24$ to the previously deduced value $\beta \approx 0.35$ at a constant sample temperature $\mathrm{T_{sample}} = 300\,\mathrm{K}$, which was determined by Boulle *et al.* [Bou+08]. Both values are in good agreement showing that the spin torque efficiency is intrinsic to the material.

5.3 Dominant Adiabatic Spin Torque in Co/Ni Multilayer Nanowires

Another promising candidate for spintronic applications is the Co/Ni multilayer material introduced in Sec. 4.2.3, which possesses similar material parameters (effective anisotropy, saturation magnetization) compared to the Co/Pt multilayer material. Therefore, one might expect high β values since narrow domain walls are present, too. This assumption is also furthered by the fact that high domain wall velocities in similar Co/Ni multilayer compositions have been observed [Koy+11].

The results shown in this section have been published in Journal of Physics: Condensed Matter [Hei+12].

5.3.1 Measurement Technique

The knowledge gained from the Co/Pt measurements allows us to extend the measurement scheme (see Fig. 5.2) so that short ns-long pulses can be injected into the nanowire in order to reduce the Joule heating effects. We used a short ($< 2\,\mu\text{m}$) nanowire structure of the type presented in Fig. 4.1(b), which possesses a low longitudinal resistance of a few hundred Ω. The production of the sample was performed using the lift-off process. The attached SMD coils in close proximity to the Hall cross contacts reduces possible reflections of short ns-long pulses, so that we were able to inject 10 ns long pulses along the wire.

The determination of the injected current density required an alteration of the electrical circuit presented in Fig. 5.2. First, we separated the Lock-In reference output from the pulse generator by inserting a Bias-Tee at the position marked by the red circle. Furthermore, a beam-splitter inserted close to the pulse generator was used to split the pulse into two equal parts. Using the oscilloscope's 50 Ω mode enabled us to measure the injected current and additionally the 2-point resistance (between contact points 1 and 4).

The domain wall depinning field was then measured similarly as for the Co/Pt multilayer material. The absolute values of the depinning field for both initial magnetization configurations and both current polarities are plotted in Fig. 5.5. Additionally, we determined the domain wall depinning field when starting the pulse injection from a saturated state for which no domain wall is present in the wire.

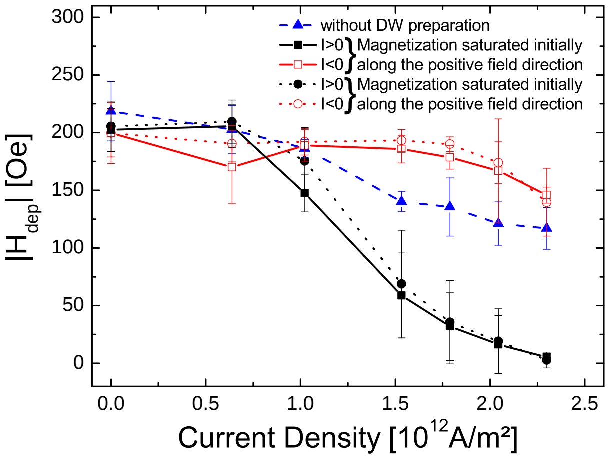

Figure 5.5: $|\mathrm{H}_{\mathrm{dep}}|$ as a function of the injected current density for both initial magnetization configurations and both current polarities. In addition, the measurement without initial domain wall preparation highlights the importance of Joule heating effects. Each data point represents the mean value of $\mathrm{H}_{\mathrm{dep}}$ averaged over several repetitions. The error bars represent the corresponding standard deviations. The lines are interpolations between the data points.

5.3.2 Results

Even in the case of the saturated state the depinning field decreases with increasing current density, highlighting the strong influence of Joule heating effects due to the injection of high current densities. The variation of the depinning fields with increasing current density reveals a drastic decrease in the cases of the positive current polarities at about $1.5 \cdot 10^{12}\,\mathrm{A/m^2}$, while the other two curves (negative current polarities) remain almost constant.

Again, the combination of all four sets of data allows us to separate the spin torque contribution, the Oersted field effects, and the Joule heating effects (see Sec. 5.1). The results of the spin torque contribution and Oersted field effect are presented in Fig. 5.6.

Here, the spin torque contribution reveals a step-like behavior at a threshold current density of about $1.5 \cdot 10^{12}\,\mathrm{A/m^2}$. For the four highest injected current densities the spin torque contribution remains about 70 Oe. Meanwhile, the Oersted field effect is zero within the error bars over the whole range of injected current densities.

5.3.3 Discussion

The successful application of short ns-pulses in order to reduce Joule heating can be observed regarding the case of no domain wall preparation (see Fig. 5.5). Despite a decrease of the depinning field with increasing current density, it remains almost constant

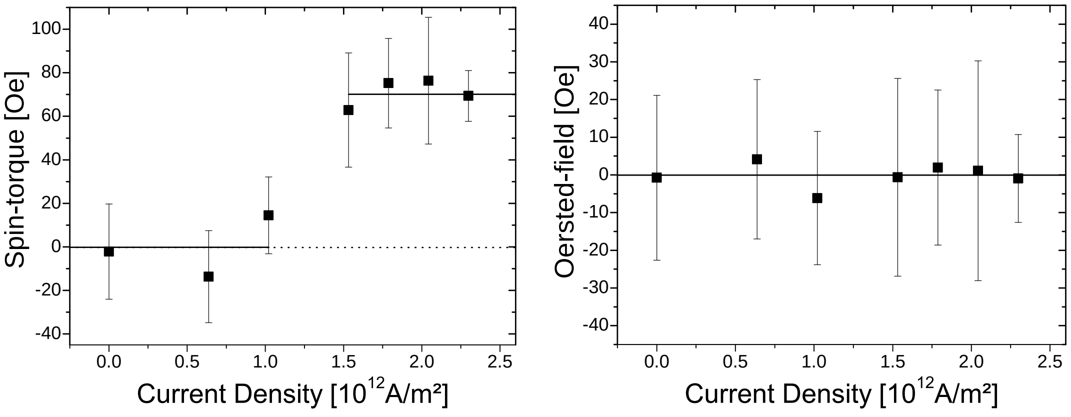

(a) (b)

Figure 5.6: The deduced spin torque contribution (a) and Oersted field effect (b). A step-like behavior of the spin torque contribution is observed at a critical current density of about $1.5 \cdot 10^{12}\,\mathrm{A/m^2}$. (from Ref. [Hei+12])

at even higher current densities compared to the injected current densities used in the Co/Pt multilayer experiment. Still, a temperature increase of more than 100 K can be expected.

The step-like behavior of the spin torque contribution does not fit to the expected linear dependence of the non-adiabatic spin torque, which has been observed in the case of the Co/Pt multilayer wire. Moreover, the existence of a critical current density of about $1.5 \cdot 10^{12}\,\mathrm{A/m^2}$ points towards the adiabatic spin torque as the driving mechanism and to $\beta \approx 0$. The same conclusion has been found by other groups performing experiments on similar Co/Ni multilayer materials [Ued+11; Koy+11; Fuk+10]. The observed critical current densities are similar to our experimental result.

The reason for the dominating non-adiabatic spin torque in the Co/Pt multilayer material and the dominating adiabatic torque for the Co/Ni multilayer material remains unclear, since most of the material parameters (effective anisotropy, saturation magnetization, domain wall width) are similar. A possible explanation might be found by analyzing the Gilbert damping constant α, which is predicted to be related to the spin relaxation mechanism β_{SR} [Thi+05; ZL04] possibly dominating the non-adiabatic spin torque contribution in the case of the Co/Pt multilayer material, where $\beta = 0.24$ turned out to be of the same order of magnitude like the Gilbert damping constant $\alpha = 0.15$ [Bar+07]. In contrast, ten times smaller Gilbert damping constants have been reported in Co/Ni multilayer materials consisting of similar compositions with respect to the Co and Ni thicknesses [Bea+07; Miz+11]. Therefore, the non-adiabatic spin torque in the Co/Ni multilayer materials might be too small to be resolved by the experimental approach used.

5.4 Domain Wall Nucleation in Co/Ni-CoFeB Multilayer Nanowires

The last out-of-plane magnetized material used for the domain wall depinning field measurements is the Co/Ni-CoFeB multilayer material (see Sec. 4.2.4). The hysteresis curves measured at different cryostat temperatures revealed no plateaus indicating that within the Hall crosses no pinning occurs, which could be used to reproducibly prepare a domain wall using an external out-of-plane magnetic field. In the next section, a measurement scheme will be presented utilizing the Oersted field effect as described in Sec. 1.4.1. This measurement technique enabled us to perform the domain wall depinning field measurements even at constant cryostat temperatures of a few Kelvin. Important to note is that the first experiments were performed at 300 K. Here, the injection of current lead to a change of the coercive field, which might be caused by Joule heating effects leading either to an alteration of the domain wall nucleation sites or to a change of the magnetic configuration itself. To prevent the sample from further damage, we decided to lower the cryostat temperature to $\mathrm{T}_{\mathrm{cryo}} = 4.3\,\mathrm{K}$.

5.4.1 Measurement Technique

The measurement scheme is an adaptation of the technique used for the Co/Pt multilayer measurements. The wire geometry was chosen to be of the type presented in Fig. 4.1(d). The insertion of two remotely controlled switches close the positions 1 and 4 indicated in Fig. 5.7 allows us to use one pulse generator to create the local Oersted field and to inject a current along the wire. Since, high currents were required to create sufficiently large Oersted fields, we inserted a pulse amplifier (max. 200 mA) and a rectifier after the pulse generator output. Here, the rectifier prevents the current created by the Lock-In from flowing into the pulse amplifier, but this causes a disadvantage since a change of the current polarity (direction of electron flow) now requires the manual switching of the ground and the current injection contact at the ends of the sample. Furthermore, long pulses (100 µs) with a long rise and fall time (10 µs) were used due to a limitation of the pulse amplifier.

To determine the necessary current to create a sufficiently large Oersted field to locally reverse the magnetization, we used the same field-pulse sequence as used for the domain wall depinning field measurements. The resulting switching fields (defined as a 50% change of the extraordinary Hall signal) as a function of the injected current density

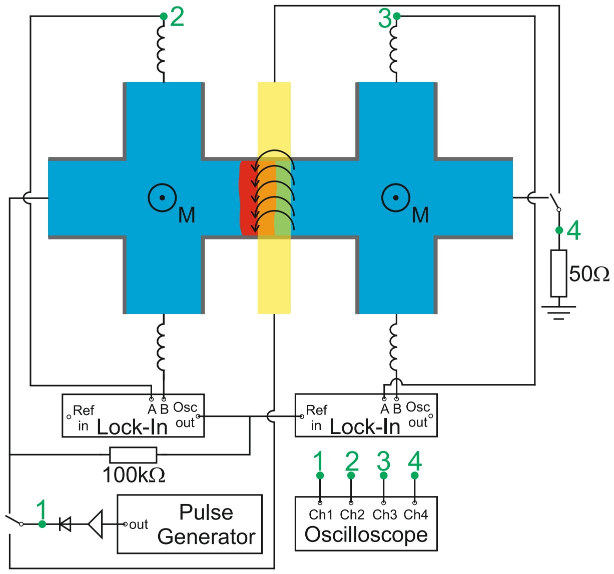

Figure 5.7: Measurement scheme for current-induced domain wall motion using Oersted field domain wall nucleation. A standard Lock-In technique is used to detect the magnetization reversal within the Hall crosses. In order to create sufficiently large Oersted fields to reverse locally the magnetization, a high current (≈ 200 mA) is generated by a pulse generator plus an additional pulse amplifier. A rectifier is used to prevent the alternating Lock-In current from flowing into the amplifier. The injected current is determined using an oscilloscope.

into the gold wire are plotted in Fig. 5.8. After a reproducible domain wall preparation sequence is found, the domain wall depinning measurements can be performed as described before.

5.4.2 Results

First, we focus on the domain wall nucleation procedure. In Fig. 5.8 both Hall crosses switch during the measurement since the local reversal of the magnetization below the gold wire creates at least two domain walls as indicated in Fig. 5.7. The external applied out-of-plane magnetic field supporting the domain wall nucleation and motion was chosen to move the domain walls in opposite directions. At low current densities $(< 1 \cdot 10^{11}\,\mathrm{A/m^2})$ the switching field remains constant and within the error of the coercive field determined from the pure field driven hysteresis loops. For high current densities $(> 1 \cdot 10^{11}\,\mathrm{A/m^2})$ the switching field is reduced in two steps ($\approx 800\,\mathrm{Oe}$ to $\approx 500\,\mathrm{Oe}$ to $< 200\,\mathrm{Oe}$).

The data points acquired at the highest current density are obtained from the domain wall preparation measurements performed during the domain wall depinning field measurements. Here, a maximum external out-of-plane magnetic field of 200 Oe was applied leading to a reversal of the second Hall cross located close (a few µm) to the gold wire, while no reversal of the first Hall cross located far away (several tens of µm) from the

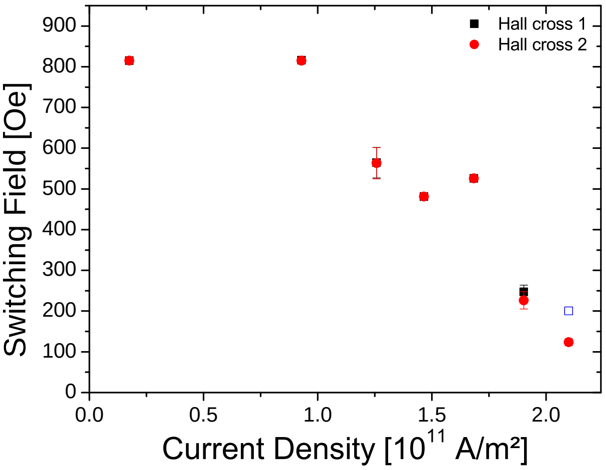

Figure 5.8: Switching field of both Hall crosses as a function of the injected current density through the gold wire across the magnetic structure. The data points acquired at the highest current density stem from the domain wall preparation measurements performed during the domain wall depinning field measurements. Here, a maximum external out-of-plane magnetic field of $200\,\mathrm{Oe}$ indicated by the blue open square was applied.

gold wire occurred. This combination of external out-of-plane magnetic field and current density allowed us to reproducibly prepare a domain wall within a Hall cross and a second one along the wire.

The extracted spin torque contribution and Oersted field effect shown in Fig. 5.9 are from the domain wall depinning field measurement. Here, we analyze the data of the first Hall cross, which was used to detect the current-induced motion of the domain wall prepared along the wire. The analysis of the data of the second Hall cross, where the second domain wall had been positioned, reveals no obvious spin torque contribution and Oersted field effects. This might be caused by a deformation of the domain wall shape within the Hall cross compared to the domain wall moving along the wire, which might have a more straight and rigid shape.

However, the usage of different threshold values in order to detect the entrance of the domain wall into the first Hall cross (10%), it's motion within the Hall cross (50%) or the domain wall leaving the Hall cross (90%), reveals a variation of the strenght of the spin torque and Oersted field effect for current densities larger than $3 \cdot 10^{11}\,\mathrm{A/m^2}$. At low current densities ($< 2.5 \cdot 10^{11}\,\mathrm{A/m^2}$) the spin torque contribution stays almost zero, while the Oersted field effect remains almost zero even for current densities up to $3 \cdot 10^{11}\,\mathrm{A/m^2}$.

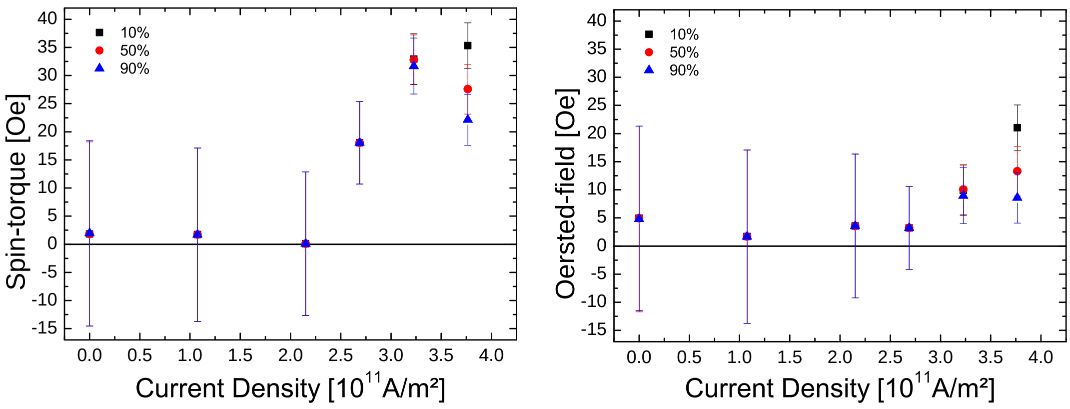

(a) (b)

Figure 5.9: The deduced spin torque contribution (a) and Oersted field effect (b) using different threshold values in order to detect the entering of the domain wall into the first Hall cross (10%), it's motion within the Hall cross (50%) or the domain wall leaving the Hall cross (90%).

5.4.3 Discussion

In general, the domain wall nucleation utilizing the Oersted field effect turns out to be technically challenging, but is most suitable to reproducibly nucleate and position domain walls along wire structures over a large temperature range. Various other groups also presented its successful application at different structure types and temperatures [Koy+11; Ued+11; Koy+08; NIA11; Fuk+10; Tan+11; Chi+10; Ohs+11].

The differences in the variation of the spin torque contribution and the Oersted field effect with the threshold value used point to a strong influence by the shape of the domain wall and its position within the Hall cross. A domain wall entering a Hall cross might get pinned at one of the edges and therefore becomes prone to depinning by a local Oersted field. At this position, the domain wall remains straight and rigid possibly leading to an efficient spin torque. A complete deformation of the domain wall structure for the positions within the Hall cross (50% and 90%) might explain the lowering of the efficiency of both effects.

Moreover, neither an adiabatic nor non-adiabatic spin torque contribution seems to be dominant as far as the qualitative shape of the curves is concerned. A clarification of the variation of both contributions at higher current densities requires the injection of current densities exceeding $5 \cdot 10^{11}\,\mathrm{A/m^2}$ leading to significant Joule heating in the case of the present pulse width of $100\,\mu\mathrm{s}$.

5.5 Thermally Activated Domain Wall Motion in Co/Pt Multilayer Nanowires

In the preceding sections, the successful application of the domain wall depinning field measurement technique was shown. However, it turned out that this approach underlies many restrictions concerning the sample temperature stability and therefore requires cumbersome measurements. In this section, a technique based on the thermally activated domain wall motion under the influence of combined charge currents and magnetic fields will be presented. This technique allows us to determine the non-adiabaticity parameter β following i) the current-field equivalence and ii) the Arrhenius law approach introduced in Sec. 1.4.5.

The Co/Pt multilayer material introduced in Sec. 4.2.1 is used for this experiment, since the domain wall depinning measurements presented in Sec. 5.2 revealed a large non-adiabaticity parameter $\beta = 0.35$ at room temperature. Therefore, one might also expect a strong influence from the injected spin-polarized charge current on the thermally activated domain wall motion between two metastable pinning sites within a Hall cross structure of the type presented in Fig. 4.1(a). The dimensions of the Hall cross are: wire width $\mathrm{w} = 500\,\mathrm{nm}$ and width of the Hall cross $\mathrm{W} = 500\,\mathrm{nm}$.

The results shown in this section have been published in Applied Physics Letters [Hei+11].

5.5.1 Measurement Technique

The high spatial sensitivity of the extraordinary Hall effect allows one not only to detect the entrance of a domain into a Hall cross structure, but also its movement within. In order to determine these movements, a small direct current ($< 2 \cdot 10^{11}\,\mathrm{A/m^2}$) is injected along the wire and an oscilloscope is used for a time resolved monitoring of the extraordinary Hall voltage (see Fig. 5.10). A differential voltage preamplifier (*SR560*) is used, since the extraordinary Hall voltages are too small (a few µV) to be directly measured by the oscilloscope. An amplification factor of 1000x was chosen and the lowpass filter of the differential voltage preamplifier set to a value below 100 kHz. Here, the use of a lowpass filter significantly reduces the noise, while the measurements of the dwell times for which a domain wall stays in a metastable state, typically in the range of

Figure 5.10: Measurement scheme to detect thermally activated domain wall motion in a Hall cross. The extraordinary Hall voltages generated by a direct current are amplified using a differential voltage preamplifier (*SR560*) before using an oscilloscope to monitor their time dependence.

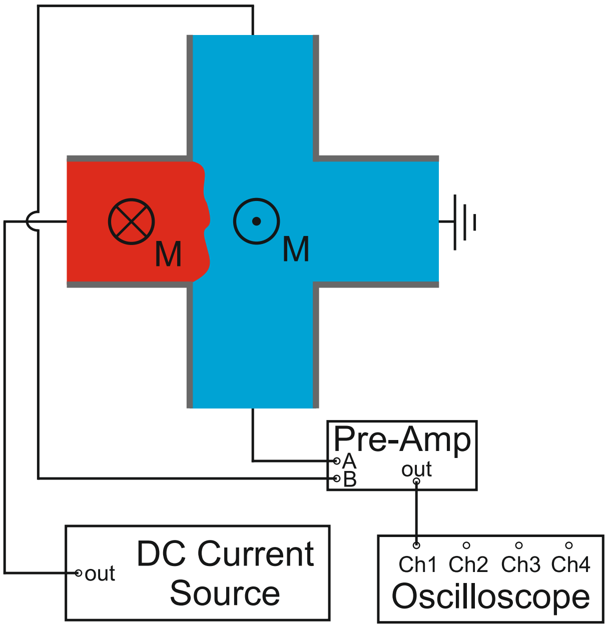

a few ms to even hours, are not affected. Statistically even shorter dwell times ($<$ ms) occur, which can be neglected since their contribution to the cumulative distributions (see Fig. 5.12) are small.

For temperatures close to room temperature, the domain wall nucleation and positioning can be achieved by using an external out-of-plane magnetic field. Initially, the sample is saturated in one out-of-plane magnetic field direction before it is relaxed to zero. Increasing the out-of-plane magnetic field in the opposite direction leads to a change in the extraordinary Hall voltage indicating that a domain wall has entered the Hall cross. By sweeping the out-of-plane magnetic field back and forth in small steps of a few Oersted, metastable pinning states can be found, which are indicated by 'jumps' in the extraordinary Hall voltage between discrete values (see Fig. 5.11).

5.5.2 Results

In the present experiment, we focused on the thermally activated motion of a domain wall between two metastable pinning states (State 0 and State 1). The cryostat temperature was stabilized at $(296.6 \pm 0.1)\,\mathrm{K}$. Temperature instabilities due to Joule heating effects are assumed to be negligible, since small current densities ($< 2 \cdot 10^{11}\,\mathrm{A/m^2}$) were used for

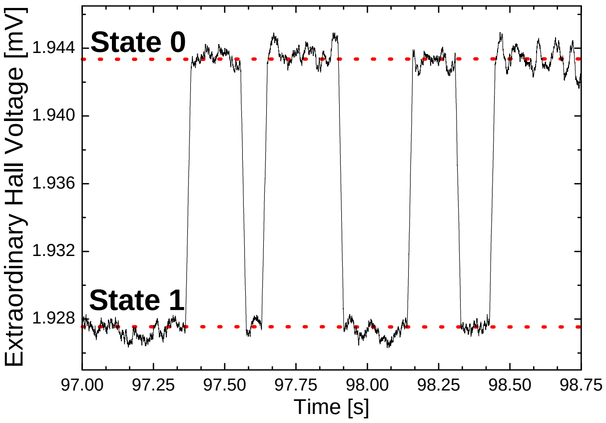

Figure 5.11: The time resolved measurement of the extraordinary Hall voltage reveals two metastable pinning states for a constant out-of-plane magnetic field (3.41 Oe) and a constant current density ($J = 1.16 \cdot 10^{11}$ A/m^2). (from Ref. [Hei+11])

which no change of the depinning field could be observed in the previous measurements (see Fig. 5.3(b)).

An example of the extraordinary Hall voltage variation as a function of time is shown in Fig. 5.11. The extraordinary Hall voltage is recorded for several minutes before the external magnetic field or direct current is changed to obtain sufficient statistics of the dwell times for which the domain wall stays in one of the states $\mathrm{S} = 0, 1$. This procedure is repeated for several combinations of current densities, current polarities and magnetic field amplitudes.

We use the normalized cumulative distributions to show the influence of either current or magnetic field on the dwell times of the metastable states S. In Fig. 5.12(a)) the increase of the magnetic field amplitude leads to longer dwell times of the state 1, while a drastic decrease for the state 0 is observed. The influence of a change of current polarity is shown in Fig. 5.12(b). Here, the change of current polarity leads to increasing dwell times for the state 1 and decreasing dwell times for the state 0. The similarity of the effect due to a magnetic field and the effect of the charge current points towards the expected current-field equivalence (see Sec. 1.4.5).

For each parameter set of current density and magnetic field, we calculate the dwell times τ_0 and τ_1 as the average values of all measured times for which the domain wall stays in either state 0 or state 1. The errors correspond to the standard deviation of the mean value multiplied with $1/\sqrt{\mathrm{N}}$ (N number of measured times). Consistent results can be obtained using the cumulative distribution function [Att+06]:

$$\mathrm{F(t)} = 1 - \mathrm{e}^{-\frac{\mathrm{t}}{\tau_\mathrm{S}}}, \tag{5.6}$$

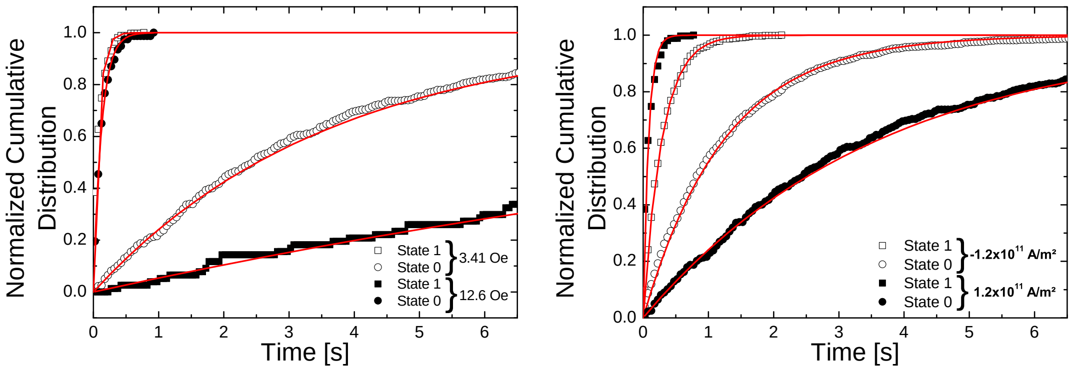

(a) (b)

Figure 5.12: The normalized cumulative distributions of both metastable states at either a constant current density for two different magnetic fields (a) or at a constant magnetic field for two different constant current densities (b) are fitted using the cumulative distribution function F(t) (red, solid lines).

which yields a good fit to the experimental data, indicating that a single transition path between both metastable pinning states is present.

Following the current-field equivalence approach, we plot $\ln(\tau_1/\tau_0)$ as a function of the magnetic field for the case of two different constant currents (see Fig. 5.13(a)). In order to analyze the data following the Arrhenius law approach presented in Sec. 1.4.5, we plot $\ln(\tau_1/\tau_0)$ as a function of the current density for the case of different constant magnetic fields (see Fig. 5.13(b)). In both cases, $\ln(\tau_1/\tau_0)$ values progresses linearly.

5.5.3 Discussion

The extensive study of the dwell times under the influence of spin-polarized charge currents and out-of-plane magnetic fields presented in the preceding section allows us to utilize the current-field equivalence and the Arrhenius law approach to independently determine the non-adiabaticity parameter β. To justify the use of these approaches, we first determine whether we are in a weak pinning regime, which is governed by β. Following the theoretical approach of Tatara *et al.* [Tat+06], which has been discussed in Sec. 1.4.3, we can show that our approaches are valid due to an existing weak pinning regime Ib as defined in Ref. [Tat+06].

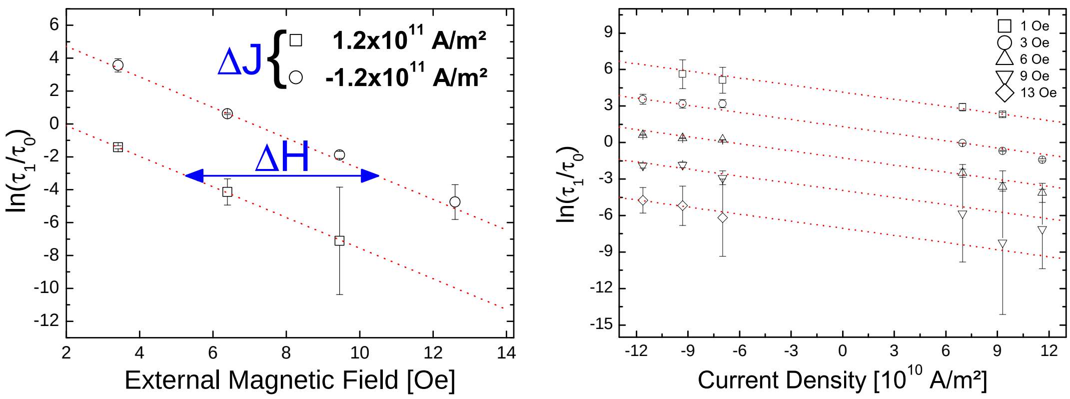

(a) (b)

Figure 5.13: (a) $\ln(\tau_1/\tau_0)$ as function of the magnetic field for two constant current densities. We use a linear fit to determine the slope for each data set at a constant current density. To calculate the shift in magnetic field $\Delta\mathrm{H}$, the data is refitted using an average slope determined from all fits (red, dotted lines). (b) $\ln(\tau_1/\tau_0)$ as function of the injected current density for different constant magnetic fields. The non-adiabaticity parameter is determined from the average slope of all fits. (from Ref. [Hei+11])

Current-field Equivalence

Based on previous measurements we calculate the shift in the magnetic field $\Delta\mathrm{H}$, which is caused by a change of the current density $\Delta\mathrm{J}$. For each data set at a constant current density (see Fig. 5.13(a)) (including the measurements at constant current densities not shown), we use a linear fit and the resulting average slope ξ to deduce the intercepts Γ_J with the Y-axis. The shift in the magnetic field $\Delta\mathrm{H}$ is then obtained by solving the following equation:

$$\xi\mathrm{H} + \Gamma_{+\mathrm{J}} = \xi(\mathrm{H} + \Delta\mathrm{H}) + \Gamma_{-\mathrm{J}}. \tag{5.7}$$

The efficiency is then given by:

$$\epsilon = \left|\frac{\Delta\mathrm{H}}{\Delta\mathrm{J}}\right| = \beta\frac{\mathrm{P}\hbar}{2\mathrm{eM_S}\lambda} \tag{5.8}$$

using the same material parameters as in Sec. 5.2.3. Taking all possible combinations of $\Delta\mathrm{H}$ and $\Delta\mathrm{J}$ into account and their corresponding errors as weighing factors, we calculate an average value of $\beta_\text{effective} = 0.13 \pm 0.02$.

The repetition of the experiment at different metastable pinning states and a slightly different cryostat temperature ($(287.2 \pm 0.1)\,\mathrm{K}$) revealed non-adiabaticity parameters $\beta_{\mathrm{effective}}$ ranging from 0.13 to 0.23. In general, all determined values turn out to be in good agreement with the previous experiments presented in Sec. 5.2 ($\beta = 0.24$ at $300\,\mathrm{K}$) and by Boulle *et al.* ($\beta = 0.35$ at $300\,\mathrm{K}$) [Bou+08].

Arrhenius Law Approach

Now we turn to the Arrhenius law approach, which allows us to independently determine β on the same sample. Since the cumulative distribution function $\mathrm{F(t)}$ provides a good fit to our experimental data, we can assume that a single transition path between the two metastable pinning states is present. As discussed in Sec. 1.4.5, we consider the domain wall as a quasi particle moving in a one dimensional potential landscape separated by an energy barrier ϵ [DNM07]. In order to simplify the analysis of the data, we replace the Eq. 1.65 by a linear fit of the form $\mathrm{F}(\ln(\tau_0/\tau_1)) = \sigma \mathrm{J} + \mathrm{const.}$ using the slope [Elt+10]:

$$\sigma = \beta \frac{2\mathrm{A}\hbar\mathrm{P}}{\mathrm{k_B Te}} \frac{\mathrm{X_0}}{\lambda} \tag{5.9}$$

with spin polarization of the current P, the domain wall cross-sectional area A, domain wall displacement distance $\mathrm{X_0}$ (indicated in Fig. 1.11) and domain wall width λ.

The displacement distance $\mathrm{X_0}$ is estimated by using the change of the extraordinary Hall resistance between both metastable states ($\Delta\mathrm{R} \approx 0.032\,\Omega$). Taking into account the width of the Hall cross and the change of the extraordinary Hall resistance of a full hysteresis loop ($\Delta\mathrm{R} \approx 1.1\,\Omega$), the hopping distance can roughly be estimated as $\mathrm{X_0} \approx 14.5\,\mathrm{nm}$. Furthermore, the domain wall cross-sectional area $\mathrm{A} \approx 4300\,\mathrm{nm}^2$ is calculated from the material thickness multiplied by the wire width assuming a straight and rigid domain wall profile. From the fit of the data shown in Fig. 5.13(b), we are now able to calculate an average slope and determine the non-adiabaticity parameter $\beta_{\mathrm{Arrhenius}} = 0.013 \pm 0.001$ using Eq. 5.9.

The direct comparison of the non-adiabaticity parameters, $\beta_{\mathrm{effective}} = 0.13 \pm 0.02$ and $\beta_{\mathrm{Arrhenius}} = 0.013 \pm 0.001$, reveals a deviation of an order of magnitude. To understand the origin of this discrepancy, one needs to reconsider the parameters entering the analysis.

In the present experiment, we study a domain wall within a Hall cross structure, where deformations of the domain wall profile occur. From this might follow that the assumption of a rigid domain wall does not hold, thus affecting the calculation of the domain wall displacement distance X_0, which is a crucial parameter of the Arrhenius law approach. A comparable problem is discussed in the work of Kim *et al.* [Kim+09], where a transition from the one dimensional to the two dimensional behavior in the scaling criticality of creep domain wall motion as a function of the wire width has been observed. A similar behavior in the present experiment would result in an overestimation of the displacement distance X_0. A more precise value might be found using time resolved magnetic imaging techniques such as are used in the work of Eltschka *et al.* [Elt+10] or by full micromagnetic simulations at finite temperatures. The latter possibility has already been performed by Garcia-Sanchez *et al.* [Gar+10] showing that the effective activation volume assumed from the displacement distance in the one dimensional model can be much smaller than expected. However, approaches using micromagnetic simulations are limited by computational power, since the timescale of thermally activated processes at room temperature is at least in the ms-regime, while one simulation step is typically in the the order of fs to ps.

The discussion about the experimentally determined parameters, especially the domain wall displacement distance X_0, highlights the problem of using one dimensional models to analyze systems with two dimensional dynamics. In the case of the Arrhenius law approach, the precise knowledge of the domain wall displacement distance X_0 is key to reliably ascertain the non-adiabaticity parameter β. In contrast, the current-field equivalence approach might prove to be more robust since the deduced β values are in good agreement with previous results and most of the used parameters are reasonably well known.

6

Conclusions and Outlook

In this thesis, current-induced domain wall dynamics was probed in ferromagnetic nanowire structures using electrical measurement techniques. Furthermore, material specific magnetoresistance effects (anisotropic magnetoresistance, planar and extraordinary Hall effect) were analyzed to test the suitability of a material for spintronic applications.

In order to perform these experiments, a cryogenic system with an adjustable temperature environment and a 3D-vector magnet system was employed and adjusted to fit the experimental electronic requirements. Significant effort was put into the development of a sample holder suitable for the injection of nanosecond long current pulses into the nanowire structures. The continuous improvements of the whole electrical wiring of the setup over the last years enabled the measurement of even small magnetoresistance effects (anisotropic magnetoresistance and planar Hall effect) in the mΩ regime. These electronic improvements also lead to time-resolved measurements of the extraordinary

Hall effect and even to the observation of thermally activated domain wall dynamics in a Hall cross structure with high spatial sensitivity.

The measurements on the Heusler alloy $Co_2FeAl_{0.4}Si_{0.6}$ revealed several magnetoresistance effects such as the anisotropic magnetoresistance, which changes its sign with temperature. Additionally, the presence of an antisymmetric planar Hall effect was observed and a temperature dependent study in the range of 4.3 K to 310 K was performed. The strong temperature dependence of both effects indicated the presence of temperature induced strain resulting in a change of the magnetoresistivity tensor. Nevertheless, the existence of domain walls in localized areas of the nanowires studied could not be detected by transport for the experimental temperature range. Thus the material was not suitable for further experiments on current-induced domain wall dynamics.

By studying the extraordinary Hall effect in various multilayer materials with an out-of-plane magnetization, a strong dependence on the basic materials, Pt or Ni, was found resulting in either an increasing or decreasing extraordinary Hall resistivity with increasing temperature. However, neither the skew scattering contribution nor the combined intrinsic and side jump effects seem to dominate the extraordinary Hall effect in these materials. In the case of the material compositions with an additional layer of CoFeB, larger coefficients are found, which turn out to be even of opposite sign in the case of the Pt-based composition. Here, the use of CoFeB induces a change from a crystalline structure to an amorphous structure possibly resulting in the enhancement of all contributions.

However, the extraordinary Hall effect in the out-of-plane magnetized multilayer materials enabled the detection of domain walls within the Hall cross structures with high spatial resolution. A newly developed measurement approach allowed the separation of Joule heating effects, Oersted field effects and the spin torque contribution on current-induced domain wall motion. In the case of the Co/Pt multilayer material, the non-adiabatic spin torque dominates the other contributions (Oersted field effect and adiabatic spin torque) to the current-induced domain wall motion and allowed us to use the current-field equivalence to determine the non-adiabaticity parameter $\beta = 0.24$ at 300 K, which turns out to be in line with previous results ($\beta = 0.35$) [Bou+08]. Surprisingly, the Co/Ni multilayer material revealed a dominating adiabatic spin torque despite its similarity to the Co/Pt multilayer regarding the material properties such as saturation magnetization and effective anisotropy.

The theoretical prediction of strong non-adiabatic contributions due to narrow domain walls of only a few nanometers, which are present in both materials, could not be confirmed. Further investigations concerning the Gilbert damping constant α could provide further insight since the spin relaxation mechanism is directly coupled to this parameter. In the case of the Co/Pt multilayer material $\beta = 0.24$ is of the same order of magnitude as $\alpha = 0.15$ [Bar+07], while for the Co/Ni multilayer material ten times smaller Gilbert damping constants have been reported [Bea+07; Miz+11]. Therefore, the non-adiabatic spin torque in the Co/Ni multilayer materials might be too small to be resolved by the experimental approaches used.

The measurements on the Co/Ni-CoFeB multilayer material show the successful application of the Oersted field domain wall nucleation technique. Here, domain walls were reproducibly nucleated and positioned within a nanowire structure with two attached Hall crosses to detect the domain wall motion at both ends of the nanowire. However, the current densities used for the domain wall depinning field experiment were too low to determine whether an adiabatic and/or non-adiabatic spin torque is present. A repetition of this experiment using higher current densities could clarify this. However, at much lower current densities ($< 3 \cdot 10^{11}\,\mathrm{A/m^2}$), non-zero contributions from spin torque mechanisms emerge compared to the case of the 'pure' Co/Ni multilayer material ($\mathrm{J_c} \approx 1.5 \cdot 10^{12}\,\mathrm{A/m^2}$).

Further measurements of thermally activated domain wall motion under the influence of a spin polarized charge current and external magnetic fields were performed using the Co/Pt multilayer material. The variation of both, current and field, allows to test the reliability and robustness of the two independent approaches, current-field equivalence and Arrhenius law, at the same time on one sample. The β values determined differ by an order of magnitude highlighting possible problems when analyzing two dimensional dynamics using one dimensional models. Here, the Arrhenius law approach was found to be strongly dependent on the precise knowledge of the domain wall displacement and the domain wall cross-sectional area to reliably ascertain the non-adiabaticity parameter β. In contrast, the current-field equivalence approach proves more robust since the β values are in good agreement with previous experiments.

In general, the measurement techniques developed in the framework of this thesis provide reliable approaches to test further out-of-plane magnetized materials and their abilities to be suitable for future spintronic applications.

Outlook

Theoretical and experimental approaches are limited in general by the precise knowledge about a vast variety of material parameters and measurement conditions, which are sometimes difficult to determine from the data. As an outlook, full micromagnetic simulations could be performed to confirm the experimental observations and provide better approximations of the critical parameters such as the domain wall displacement distance and the domain wall cross-sectional area, which could only be roughly estimated from the experimental data. Moreover, one might also gain a deeper insight into the influence of the Gilbert damping constant on the domain wall motion in out-of-plane magnetized materials. Additionally, simulations of multilayer materials concerning interlayer domain wall interactions could be performed, since strong dependencies on the layer thicknesses and number of stack repetitions have been reported [Xie+07].

In the framework of this thesis, just local areas of the magnetic nanowire structures could be observed since the extraordinary Hall effect only provides information about a changing magnetization within the Hall cross geometry. Thus the use of magnetic imaging techniques is required to resolve the current-induced domain wall motion over the whole sample structure. Possible techniques are the magnetic force microscopy (MFM), scanning electron microscopy with polarization analysis (SEMPA), x-ray magnetic circular dichroism photo electron emission microscopy (XMCD-PEEM), scanning transmission x-ray microscopy (STXM), or x-ray holography. The latter three techniques provide high temporal (a few tens of ps) [Pfa+10] and spatial resolutions (a few nm) [Cha+09] making them suitable for current-induced domain wall motion experiments. Furthermore, these techniques would be able to provide accurate informations about the domain wall displacement distance and cross-sectional area as shown by Eltschka *et al.* [Elt+10].

In general, detailed temperature dependent studies of the basic material parameters such as the saturation magnetization, effective anisotropy, spin polarization and the Gilbert damping constant are required since the origin of spin torque effects and their correlations to these parameters are still not fully understood.

From an experimental point of view, the precise nucleation and positioning of the domain walls can be optimized further by using electrical leads surrounding the actual magnetic wire. In Fig. 6.1 a schematic of a new nanowire design is shown. Here, the large currents

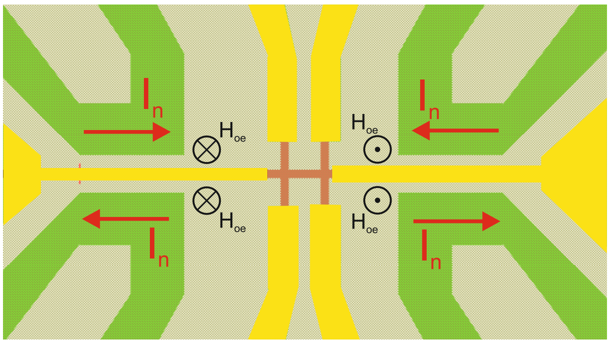

Figure 6.1: Schematic of a new sample design to nucleate domain walls using strip lines (green), which are electrically decoupled from the magnetic structure (bright red). Therefore, the injected current I_n used to create the necessary Oersted fields for domain wall nucleation cannot affect the magnetic structure itself. The remaining contacts (yellow) are used to measure the extraordinary Hall effect in order to detect the domain wall nucleation and motion.

I_n generating the Oersted fields needed to nucleate a domain wall are injected into strip lines, which are electrically decoupled from the magnetic nanostructure. This results in a significant reduction of Joule heating effects, which would lead to an alteration of the experimental conditions. Using a standard Lock-in technique the extraordinary Hall effect can be used to monitor the domain wall nucleation and motion.

This new sample design could also allow the direct determination of the intrinsic domain wall resistance since the total resistance of the magnetic nanowire is reduced due to the narrow contacts. Using this new design, a single domain wall could be positioned along the wire between the Hall cross contacts. Hence, a 4-point resistance measurement is expected to be sensitive enough to even resolve resistances in the sub-$\mu\Omega$ regime. Based on the intrinsic domain wall resistance, the non-adiabaticity parameter β could be determined. Additionally, the possibility to use the approaches to determine β as described in this thesis would remain and could thus be compared.

A

Technical Drawings

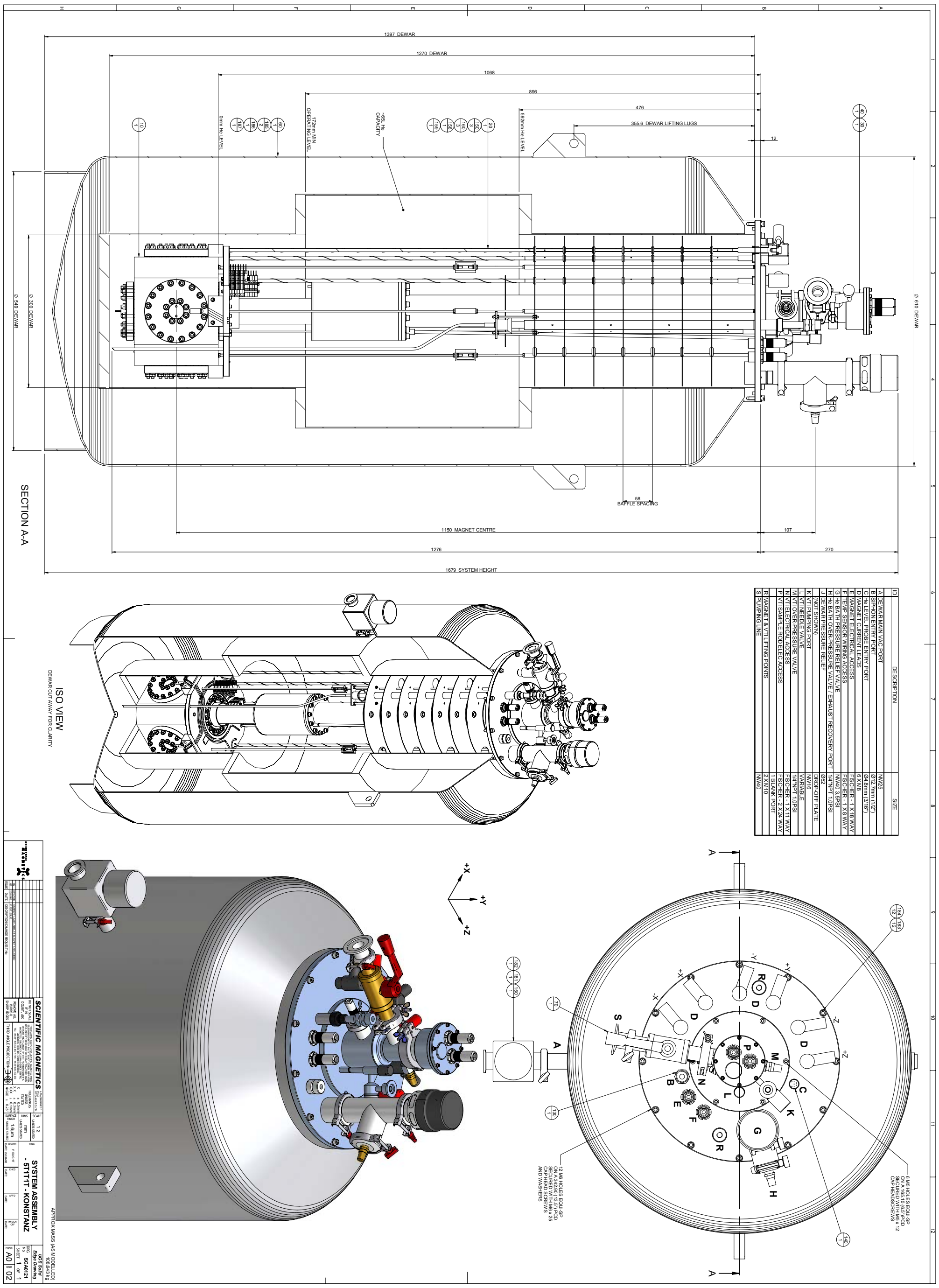

Figure A.1: Assembly of the cryostat system designed by Scientific Magnetics. [Mag08]

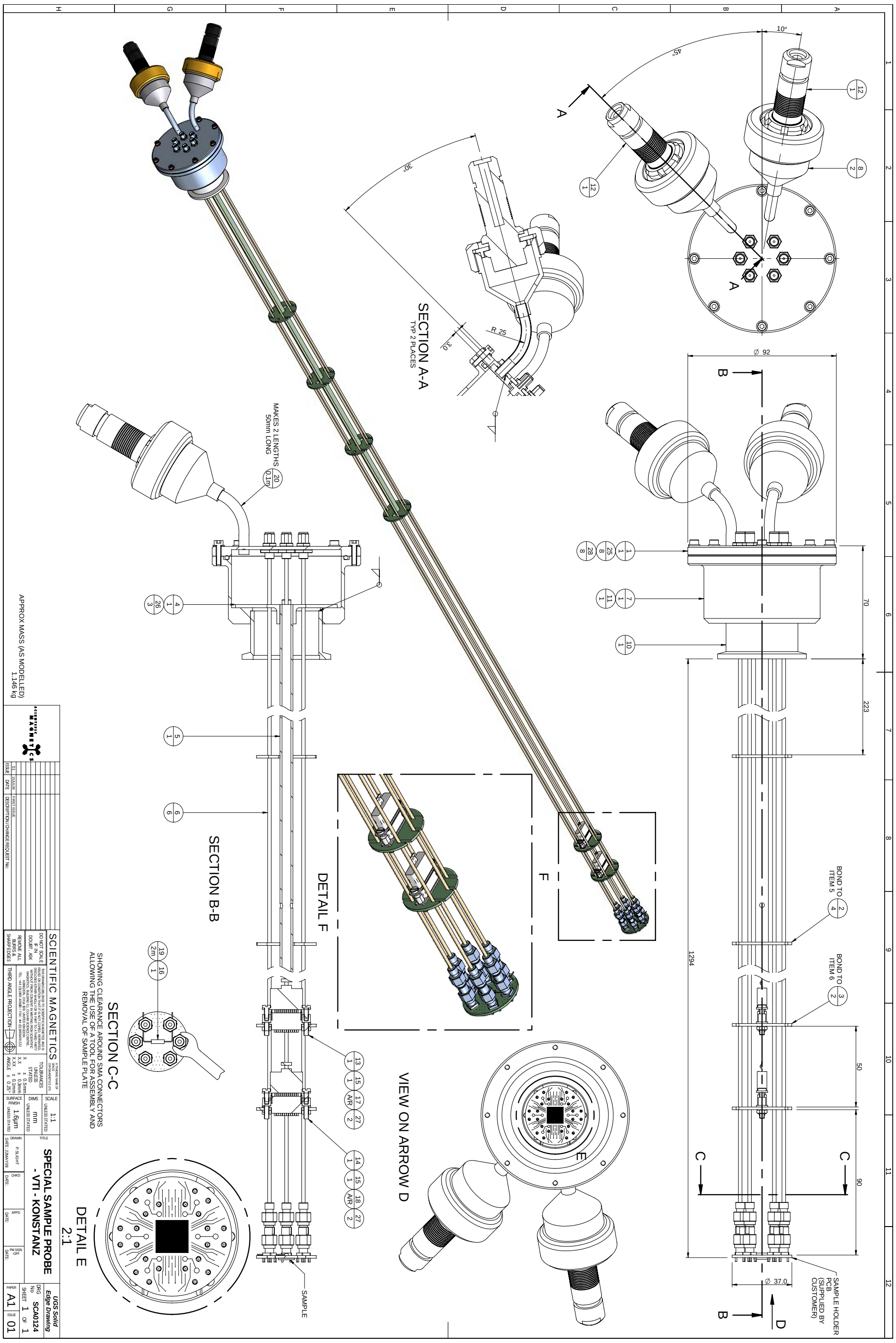

Figure A.2: Assembly of the sample rod designed by Scientific Magnetics. [Mag08]

Bibliography

[AB] Comsol AB. *Comsol Multiphysics.*

[Aha00] A. Aharoni. *Introduction to the theory of ferromagnetism.* 2nd. Oxford, 2000.

[Att+06] J. P. Attané, D. Ravelosona, A. Marty, Y. Samson, and C. Chappert. 'Thermally Activated Depinning of a Narrow Domain Wall from a Single Defect'. In: *Physical Review Letters* 96 (2006), p. 147204.

[Bar+07] A. Barman, S. Wang, O. Hellwig, A. Berger, E. E. Fullerton, and H. Schmidt. 'Ultrafast magnetization dynamics in high perpendicular anisotropy $[Co/Pt]_n$ multilayers'. In: *Journal of Applied Physics* 101 (2007), p. 09D102.

[Bas+09] Y. Bason, J. Hoffman, C. H. Ahn, and L. Klein. 'Magnetoresistance tensor of $La_{0.8}Sr_{0.2}MnO_3$'. In: *Physical Review B* 79 (2009), p. 092406.

[Bea+07] J.-M.L. Beaujour, W. Chen, K. Krycka, C.-C. Kao, J. Z. Sun, and A. D. Kent. 'Ferromagnetic resonance study of sputtered Co/Ni multilayers'. In: *The European Physical Journal B - Condensed Matter and Complex Systems* 59 (2007), p. 475.

[Bed08] D. Bedau. 'Domain Wall Dynamics in Magnetic Nanostructures'. PhD thesis. Konstanz: Universität Konstanz, 2008.

[Ber70] L. Berger. 'Side-Jump Mechanism for the Hall Effect of Ferromagnets'. In: *Physical Review B* 2 (1970), p. 4559.

[Ber78] L. Berger. 'Low-field magnetoresistance and domain drag in ferromagnets'. In: *Journal of Applied Physics* 49 (1978), p. 2156.

[BHB91] F.J.A. den Broeder, W. Hoving, and P.J.H. Bloemen. 'Magnetic anisotropy of multilayers'. In: *Journal of Magnetism and Magnetic Materials* 93 (1991), p. 562.

[Bir64] R. R. Birss. *Symmetry and Magnetism.* North-Holland, Amsterdam, 1964.

[BMK11] O. Boulle, G. Malinowski, and M. Kläui. 'Current-induced domain wall motion in nanoscale ferromagnetic elements'. In: *Materials Science and Engineering: R: Reports* 72 (2011), p. 159.

[Bou+08] O. Boulle, J. Kimling, P. Warnicke, M. Kläui, U. Rüdiger, G. Malinowski, H. J. M. Swagten, B. Koopmans, C. Ulysse, and G. Faini. 'Nonadiabatic Spin Transfer Torque in High Anisotropy Magnetic Nanowires with Narrow Domain Walls'. In: *Physical Review Letters* 101 (2008), p. 216601.

[Bou+09] O. Boulle, L. Heyne, J. Rhensius, M. Kläui, U. Rüdiger, L. Joly, L. Le Guyader, F. Nolting, L. J. Heyderman, G. Malinowski, H. J. M. Swagten, B. Koopmans, C. Ulysse, and G. Faini. 'Reversible switching between bidomain states by injection of current pulses in a magnetic wire with out-of-plane magnetization'. In: *Journal of Applied Physics* 105 (2009), p. 07C106.

[Bro63] W. F. Brown. *Micromagnetics.* New York: Wiley, 1963.

[Bur+10] C. Burrowes, A. P. Mihai, D. Ravelosona, J.-V. Kim, C. Chappert, L. Vila, A. Marty, Y. Samson, F. Garcia-Sanchez, L. D. Buda-Prejbeanu, I. Tudosa, E. E. Fullerton, and J.-P. Attané. 'Non-adiabatic spin-torques in narrow magnetic domain walls'. In: *Nature Physics* 6 (2010), p. 17.

[Cha+09] W. Chao, J. Kim, S. Rekawa, P. Fischer, and E. H. Anderson. 'Demonstration of 12 nm Resolution Fresnel Zone Plate Lens based Soft X-ray Microscopy'. In: *Optics Express* 17 (2009), p. 17669.

[Chi+10] D. Chiba, G. Yamada, T. Koyama, K. Ueda, H. Tanigawa, S. Fukami, T. Suzuki, N. Ohshima, N. Ishiwata, Y. Nakatani, and T. Ono. 'Control of Multiple Magnetic Domain Walls by Current in a Co/Ni Nano-Wire'. In: *Applied Physics Express* 3 (2010), p. 073004.

[Cow+07] R. Cowburn, D. Petit, D. Read, and O. Petracic. 'Patent wo 2007/132174a1'. In: *Patent wo 2007/132174a1* (2007).

[Dag+07] P. Dagras, M. Kläui, M. Laufenberg, D. Bedau, L. Vila, G. Faini, C. A. F. Vaz, J. A. C. Bland, and U. Rüdiger. ‘The influence of thermal activation and the intrinsic temperature dependence of the spin torque effect in current-induced domain wall motion’. In: *Journal of Physics D: Applied Physics* 40 (2007), p. 1247.

[DNM07] R. A. Duine, A. S. Núñez, and A. H. MacDonald. ‘Thermally Assisted Current-Driven Domain-Wall Motion’. In: *Physical Review Letters* 98 (2007), p. 056605.

[DP99] M. J. Donahue and D. G. Porter. *OOMMF user’s guide; version 1.0 interagency report NISTIR 6376*. Gaithersburg, MD, 1999.

[Elt+10] M. Eltschka, M. Wötzel, J. Rhensius, S. Krzyk, U. Nowak, M. Kläui, T. Kasama, R. E. Dunin-Borkowski, L. J. Heyderman, H. J. van Driel, and R. A. Duine. ‘Nonadiabatic Spin Torque Investigated Using Thermally Activated Magnetic Domain Wall Dynamics’. In: *Physical Review Letters* 105 (2010), p. 056601.

[Fre+90] P.P. Freitas, A.A. Gomes, T.R. McGuire, and T.S. Plaskett. ‘Anisotropic magnetoresistance in Co films’. In: *Journal of Magnetism and Magnetic Materials* 83 (1990), p. 113.

[Fuk+10] S. Fukami, T. Suzuki, H. Tanigawa, N. Ohshima, and N. Ishiwata. ‘Stack Structure Dependence of Co/Ni Multilayer for Current-Induced Domain Wall Motion’. In: *Applied Physics Express* 3 (2010), p. 113002.

[Gar+10] F. Garcia-Sanchez, H. Szambolics, A. P. Mihai, L. Vila, A. Marty, J.-P. Attané, J.-C. Toussaint, and L. D. Buda-Prejbeanu. ‘Effect of crystalline defects on domain wall motion under field and current in nanowires with perpendicular magnetization’. In: *Physical Review B* 81 (2010), p. 134408.

[Get08] M. Getzlaff. *Fundamentals of Magnetism*. Berlin; Heidelberg: Springer, 2008.

[Gil04] T. L. Gilbert. ‘A phenomenological theory of damping in ferromagnetic materials’. In: *IEEE Transactions on Magnetics* 33 (2004), p. 3443.

[GPF11] T. Graf, S. Parkin, and C. Felser. ‘Heusler Compounds - A Material Class With Exceptional Properties’. In: *IEEE Transactions on Magnetics* 47 (2011), p. 367.

[GPM11] S. Giri, M. Patra, and S. Majumdar. ‘Exchange bias effect in alloys and compounds’. In: *Journal of Physics: Condensed Matter* 23 (2011), p. 073201.

[He+10] H. T. He, X. C. Cao, T. Zhang, Y. Q. Wang, and J. N. Wang. ‘Systematic study of anisotropic magnetoresistance effect in (311)A GaMnAs films’. In: *Journal of Applied Physics* 107 (2010), p. 063902.

[Hei+10] J. Heinen, O. Boulle, K. Rousseau, G. Malinowski, M. Kläui, H. J. M. Swagten, B. Koopmans, C. Ulysse, and G. Faini. ‘Current-induced domain wall motion in Co/Pt nanowires: Separating spin torque and Oersted-field effects’. In: *Applied Physics Letters* 96 (2010), p. 202510.

[Hei+11] J. Heinen, D. Hinzke, O. Boulle, G. Malinowski, H. J. M Swagten, B. Koopmans, C. Ulysse, G. Faini, and M. Kläui. ‘Extraction of the spin torque non-adiabaticity from thermally activated domain wall hopping’. In: *Applied Physics Letters* 99 (2011), p. 242501.

[Hei+12] J. Heinen, D. Hinzke, O. Boulle, G. Malinowski, H. J. M. Swagten, B. Koopmans, C. Ulysse, G. Faini, B. Ocker, J. Wrona, and M. Kläui. ‘Determination of the spin torque non-adiabaticity in perpendicularly magnetized nanowires’. In: *Journal of Physics: Condensed Matter* 24 (2012), p. 024220.

[Her+96] A. Hernando, I. Navarro, C. Prados, D. Garciá, M. Vázquez, and J. Alonso. ‘Curie-temperature enhancement of ferromagnetic phases in nanoscale heterogeneous systems’. In: *Physical Review B* 53 (1996), p. 8223.

[Hey+09] L. Heyne, J. Rhensius, Y.-J. Cho, D. Bedau, S. Krzyk, C. Dette, H. S. Körner, J. Fischer, M. Laufenberg, D. Backes, L. J. Heyderman, L. Joly, F. Nolting, G. Tatara, H. Kohno, S. Seo, U. Rüdiger, and M. Kläui. ‘Geometry-dependent scaling of critical current densities for current-induced domain wall motion and transformations’. In: *Physical Review B* 80 (2009), p. 184405.

[Him+05] A. Himeno, T. Okuno, T. Ono, K. Mibu, S. Nasu, and T. Shinjo. ‘Temperature dependence of depinning fields in submicron magnetic wires with an artificial neck’. In: *Journal of Magnetism and Magnetic Materials* 286 (2005), pp. 167–170.

[HS98] A. Hubert and R. Schäfer. *Magnetic domains*. 1st. Berlin: Springer, 1998.

[HTB90] P. Hänggi, P. Talkner, and M. Borkovec. ‘Reaction-rate theory: fifty years after Kramers’. In: *Reviews of Modern Physics* 62 (1990), p. 251.

[IL09] H. Ibach and H. Lüth. *Festkörperphysik*. 7th. Berlin: Springer-Verlag, 2009.

[Ilg+08] D. Ilgaz, M. Kläui, L. Heyne, O. Boulle, F. Zinser, S. Krzyk, M. Fonin, U. Rüdiger, D. Backes, and L. J. Heyderman. 'Selective domain wall depinning by localized Oersted fields and Joule heating'. In: *Applied Physics Letters* 93 (2008), p. 132503.

[Jen+06] S. U. Jen, Y. D. Yao, Y. T. Chen, J. M. Wu, C. C. Lee, T. L. Tsai, and Y. C. Chang. 'Magnetic and electrical properties of amorphous CoFeB films'. In: *Journal of Applied Physics* 99 (2006), p. 053701.

[KA00] P. J. Kelly and R. D. Arnell. 'Magnetron sputtering: a review of recent developments and applications'. In: *Vacuum* 56 (2000), p. 159.

[Kim+09] K.-J. Kim, J.-C. Lee, S.-M. Ahn, K.-S. Lee, C.-W. Lee, Y. J. Cho, S. Seo, K.-H. Shin, S.-B. Choe, and H.-W. Lee. 'Interdimensional universality of dynamic interfaces'. In: *Nature* 458 (2009), p. 740.

[Kim+11] K.-J. Kim, J. Ryu, G.-H. Gim, J.-C. Lee, K.-H. Shin, H.-W. Lee, and S.-B. Choe. 'Electric Current Effect on the Energy Barrier of Magnetic Domain Wall Depinning: Origin of the Quadratic Contribution'. In: *Physical Review Letters* 107 (2011), p. 217205.

[Kl03] M. Kläui, C. A. F. Vaz, J. Rothman, J. A. C. Bland, W. Wernsdorfer, G. Faini, and E. Cambril. 'Domain Wall Pinning in Narrow Ferromagnetic Ring Structures Probed by Magnetoresistance Measurements'. In: *Physical Review Letters* 90 (2003), p. 097202.

[KL54] R. Karplus and J. M. Luttinger. 'Hall Effect in Ferromagnetics'. In: *Physical Review* 95 (1954), p. 1154.

[Klä+05] M. Kläui, C. A. F. Vaz, J. A. C. Bland, W. Wernsdorfer, G. Faini, E. Cambril, L. J. Heyderman, F. Nolting, and U. Rüdiger. 'Controlled and Reproducible Domain Wall Displacement by Current Pulses Injected into Ferromagnetic Ring Structures'. In: *Physical Review Letters* 94 (2005), p. 106601.

[Koy+08] T. Koyama, G. Yamada, H. Tanigawa, S. Kasai, N. Ohshima, S. Fukami, N. Ishiwata, Y. Nakatani, and T. Ono. 'Control of Domain Wall Position by Electrical Current in Structured Co/Ni Wire with Perpendicular Magnetic Anisotropy'. In: *Applied Physics Express* 1 (2008), p. 101303.

[Koy+11] T. Koyama, D. Chiba, K. Ueda, K. Kondou, H. Tanigawa, S. Fukami, T. Suzuki, N. Ohshima, N. Ishiwata, Y. Nakatani, K. Kobayashi, and T. Ono. 'Observation of the intrinsic pinning of a magnetic domain wall in a ferromagnetic nanowire'. In: *Nature Materials* 10 (2011), p. 194.

[LD09] M. E. Lucassen and R. A. Duine. 'Fluctuations of current-driven domain walls in the nonadiabatic regime'. In: *Physical Review B* 80 (2009), p. 144421.

[Li+10] J. Li, S. L. Li, Z. W. Wu, S. Li, H. F. Chu, J. Wang, Y. Zhang, H. Y. Tian, and D. N. Zheng. 'A phenomenological approach to the anisotropic magnetoresistance and planar Hall effect in tetragonal $La_{2/3}Ca_{1/3}MnO_3$ thin films'. In: *Journal of Physics: Condensed Matter* 22 (2010), p. 146006.

[Liu+08] L.-F. Liu, W.-Y. Zhou, S.-S. Xie, O. Albrecht, and K. Nielsch. 'Microstructure and temperature-dependent magnetic properties of Co/Pt multilayered nanowires'. In: *Chemical Physics Letters* 466 (2008), p. 165.

[LL35] L. D. Landau and E. M. Lifschitz. 'On the theory of the dispersion of magnetic permeability in ferromagnetic bodies'. In: *Phys. Z. Sow.* 8 (1935), p. 153.

[LZ97] P. M. Levy and S. Zhang. 'Resistivity due to Domain Wall Scattering'. In: *Physical Review Letters* 79 (1997), p. 5110.

[Mag08] Scientific Magnetics. *3D-vector coil magnet system*. Tech. rep. Abingdon, United Kingdom: Scientific Magnetics, 2008.

[Met+07] P. J. Metaxas, J. P. Jamet, A. Mougin, M. Cormier, J. Ferré, V. Baltz, B. Rodmacq, B. Dieny, and R. L. Stamps. 'Creep and Flow Regimes of Magnetic Domain-Wall Motion in Ultrathin Pt/Co/Pt Films with Perpendicular Anisotropy'. In: *Physical Review Letters* 99 (2007), p. 217208.

[MFC06] I. R. McFadyen, E. E. Fullerton, and M. J. Carey. 'State-of-the-Art Magnetic Hard Disk Drives'. In: *MRS Bulletin* 31 (2006), p. 379.

[Míše70] K. Míšek. 'The size effect in electrical resistivity of platinum'. In: *Czechoslovak Journal of Physics* 20 (1970), p. 1214.

[Miz+11] S. Mizukami, X. Zhang, T. Kubota, H. Naganuma, M. Oogane, Y. Ando, and T. Miyazaki. 'Gilbert Damping in Ni/Co Multilayer Films Exhibiting Large Perpendicular Anisotropy'. In: *Applied Physics Express* 4 (2011), p. 013005.

[Möh11] P. Möhrke. ‘Domain Wall Dynamics probed by Magneto-Optical Kerr Magnetometry’. PhD thesis. Konstanz: University Konstanz, 2011.

[Mou+07] A. Mougin, M. Cormier, J. P. Adam, P. J. Metaxas, and J. Ferré. ‘Domain wall mobility, stability and Walker breakdown in magnetic nanowires’. In: *Europhysics Letters* 78 (2007), p. 57007.

[MP75] T. McGuire and R. Potter. ‘Anisotropic magnetoresistance in ferromagnetic 3d alloys’. In: *IEEE Transactions on Magnetics* 11 (1975), p. 1018.

[Mud+05] P. K. Muduli, K.-J. Friedland, J. Herfort, H.-P. Schönherr, and K. H. Ploog. ‘Antisymmetric contribution to the planar Hall effect of Fe_3 Si films grown on GaAs (113) A substrates’. In: *Physical Review B* 72 (2005), p. 104430.

[Nag+00] K. Nagasaka, L. Varga, Y. Shimizu, S. Eguchi, and A. Tanaka. ‘The temperature dependence of exchange anisotropy in ferromagnetic/PdPtMn bilayers’. In: *Journal of Applied Physics* 87 (2000), p. 6433.

[Nag+10] N. Nagaosa, J. Sinova, S. Onoda, A. H. MacDonald, and N. P. Ong. ‘Anomalous Hall effect’. In: *Reviews of Modern Physics* 82 (2010), p. 1539.

[Nak+10] N. Nakabayashi, A. Takeuchi, K. Hosono, K. Taguchi, and G. Tatara. ‘Theory of spin relaxation torque in metallic ferromagnets’. In: *Physical Review B* 82 (2010), p. 014403.

[Nak+98] N. Nakajima, T. Koide, T. Shidara, H. Miyauchi, H. Fukutani, A. Fujimori, K. Iio, T. Katayama, M. Nývlt, and Y. Suzuki. ‘Perpendicular Magnetic Anisotropy Caused by Interfacial Hybridization via Enhanced Orbital Moment in Co/Pt Multilayers: Magnetic Circular X-Ray Dichroism Study’. In: *Physical Review Letters* 81 (1998), p. 5229.

[NIA11] D.-T. Ngo, K. Ikeda, and H. Awano. ‘Direct Observation of Domain Wall Motion Induced by Low-Current Density in TbFeCo Wires’. In: *Applied Physics Express* 4 (2011), p. 093002.

[Ohs+11] N. Ohshima, T. Koyama, H. Tanigawa, M. Kotsugi, T. Ohkouchi, D. Chiba, T. Kinoshita, and T. Ono. ‘Real space observation of current-induced magnetic domain wall displacement in Co/Ni nano-wire by photoemission electron microscopy’. In: *Journal of Physics: Condensed Matter* 23 (2011), p. 382202.

[Pav+97] P. Pavan, R. Bez, P. Olivo, and B. Zanoni. ‘Flash memory cells-an overview’. In: *Proceedings of the IEEE* 85 (1997), p. 1248.

[Pfa+10] B. Pfau, C. M. Günther, S. Schaffert, R. Mitzner, B. Siemer, S. Roling, H. Zacharias, O. Kutz, I. Rudolph, R. Treusch, and S. Eisebitt. 'Femtosecond pulse x-ray imaging with a large field of view'. In: *New Journal of Physics* 12 (2010), p. 095006.

[PHT08] S. Parkin, M. Hayashi, and L. Thomas. 'Magnetic domain-wall racetrack memory'. In: *Science* 320 (2008), p. 190.

[Pic+08] M. Pickel, A. B. Schmidt, F. Giesen, J. Braun, J. Minár, H. Ebert, M. Donath, and M. Weinelt. 'Spin-Orbit Hybridization Points in the Face-Centered-Cubic Cobalt Band Structure'. In: *Physical Review Letters* 101 (2008), p. 066402.

[Raq+01] B. Raquet, M. Viret, P. Warin, E. Sondergard, and R. Mamy. 'Negative high field magnetoresistance in 3d ferromagnets'. In: *Physica B: Condensed Matter* 294 (2001), p. 102.

[Raq+02] B. Raquet, M. Viret, E. Sondergard, O. Cespedes, and R. Mamy. 'Electron-magnon scattering and magnetic resistivity in 3d ferromagnets'. In: *Physical Review B* 66 (2002), p. 024433.

[RCL11] J. Ryu, S.-B. Choe, and H.-W. Lee. 'Magnetic domain-wall motion in a nanowire: Depinning and creep'. In: *Physical Review B* 84 (2011), p. 075469.

[Rhe11] J. Rhensius. 'Spin Dynamics and Spin Configuration in Nanopatterned Elements'. PhD thesis. Konstanz: University Konstanz, 2011.

[Sau+88] F. Saurenbach, U. Walz, L. Hinchey, P. Grünberg, and W. Zinn. 'Static and dynamic magnetic properties of Fe-Cr-layered structures with antiferromagnetic interlayer exchange'. In: *Journal of Applied Physics* 63 (1988), p. 3473.

[Sch+07] H. Schneider, C. Herbort, G. Jakob, H. Adrian, S. Wurmehl, and C. Felser. 'Structural, magnetic and transport properties of Co_2FeSi Heusler films'. In: *Journal of Physics D: Applied Physics* 40 (2007), p. 1548.

[See+11] K. M. Seemann, F. Freimuth, H. Zhang, S. Blügel, Y. Mokrousov, D. E. Bürgler, and C. M. Schneider. 'Origin of the Planar Hall Effect in Nanocrystalline $Co_{60}Fe_{20}B_{20}$'. In: *Physical Review Letters* 107 (2011), p. 086603.

[SHD57] W. C. Shaw, D. E. Hudson, and G. C. Danielson. 'Electrical Properties of Boron Single Crystals'. In: *Physical Review* 107 (1957), p. 419.

[Sin08] N. A. Sinitsyn. 'Semiclassical theories of the anomalous Hall effect'. In: *Journal of Physics: Condensed Matter* 20 (2008), p. 023201.

[Smi51] J. Smit. 'Magnetoresistance of ferromagnetic metals and alloys at low temperatures'. In: *Physica* 17 (1951), p. 612.

[Smi58] J. Smit. 'The spontaneous hall effect in ferromagnetics II'. In: *Physica* 24 (1958), p. 39.

[Sug+92] T. Sugimoto, T. Katayama, Y. Suzuki, M. Hashimoto, Y. Nishihara, A. Itoh, and K. Kawanishi. 'Temperature dependence of perpendicular magnetic anisotropy in Co/Au and Co/Pt multilayers'. In: *Journal of Magnetism and Magnetic Materials* 104 (1992), p. 1845.

[SW74] N. L. Schryer and L. R. Walker. 'The motion of 180° domain walls in uniform dc magnetic fields'. In: *Journal of Applied Physics* 45 (1974), p. 5406.

[Tan+03] H. X. Tang, R. K. Kawakami, D. D. Awschalom, and M. L. Roukes. 'Giant Planar Hall Effect in Epitaxial (Ga,Mn)As Devices'. In: *Physical Review Letters* 90 (2003), p. 107201.

[Tan+09] H. Tanigawa, T. Koyama, G. Yamada, D. Chiba, S. Kasai, S. Fukami, T. Suzuki, N. Ohshima, N. Ishiwata, Y. Nakatani, and T. Ono. 'Domain Wall Motion Induced by Electric Current in a Perpendicularly Magnetized Co/Ni Nano-Wire'. In: *Applied Physics Express* 2 (2009), p. 053002.

[Tan+11] H. Tanigawa, K. Suemitsu, S. Fukami, N. Ohshima, T. Suzuki, E. Kariyada, and N. Ishiwata. 'Effect of Device Temperature on Domain Wall Motion in a Perpendicularly Magnetized Co/Ni Wire'. In: *Applied Physics Express* 4 (2011), p. 013007.

[Tat+06] G. Tatara, T. Takayama, H. Kohno, J. Shibata, Y. Nakatani, and H. Fukuyama. 'Threshold Current of Domain Wall Motion under Extrinsic Pinning, β-Term and Non-Adiabaticity'. In: *Journal of the Physical Society of Japan* 75 (2006), p. 064708.

[TF97] G. Tatara and H. Fukuyama. 'Resistivity due to a Domain Wall in Ferromagnetic Metal'. In: *Physical Review Letters* 78 (1997), p. 3773.

[TGS02] E. Du Trémolet de Lacheisserie, D. Gignoux, and M. Schlenker. *Magnetism: Fundamentals*. Ed. by E. D. Trémolet de Lacheisserie, D. Gignoux, and M. Schlenker. Springer, 2002.

[Thi+04] A. Thiaville, Y. Nakatani, J. Miltat, and N. Vernier. 'Domain wall motion by spin-polarized current: a micromagnetic study'. In: *Journal of Applied Physics* 95 (2004), p. 7049.

[Thi+05] A. Thiaville, Y. Nakatani, J. Miltat, and Y. Suzuki. 'Micromagnetic understanding of current-driven domain wall motion in patterned nanowires'. In: *Europhysics Letters* 69 (2005), p. 990.

[Tho+06] L. Thomas, M. Hayashi, X. Jiang, R. Moriya, C. Rettner, and S. Parkin. 'Oscillatory dependence of current-driven magnetic domain wall motion on current pulse length'. In: *Nature* 443 (2006), p. 197.

[Tho57] W. Thomson. 'On the electgro-dynamic qualities of metals: Effects of magnetization on the electric conductivity of nickel and iron'. In: *Proceedings of the Royal Society* 8 (1857), p. 546.

[TK04] G. Tatara and H. Kohno. 'Theory of Current-Driven Domain Wall Motion: Spin Transfer versus Momentum Transfer'. In: *Physical Review Letters* 92 (2004), p. 086601.

[TKS08a] G. Tatara, H. Kohno, and J. Shibata. 'Microscopic approach to current-driven domain wall dynamics'. In: *Phys. Rep.* 468 (2008), p. 213.

[TKS08b] G. Tatara, H. Kohno, and J. Shibata. 'Theory of Domain Wall Dynamics under Current'. In: *Journal of the Physical Society of Japan* 77 (2008), p. 031003.

[TYJ09] Y. Tian, L. Ye, and X. Jin. 'Proper Scaling of the Anomalous Hall Effect'. In: *Physical Review Letters* 103 (2009), p. 087206.

[Ued+11] K. Ueda, D. Chiba, T. Koyama, G. Yamada, H. Tanigawa, S. Fukami, T. Suzuki, N. Ohshima, N. Ishiwata, Y. Nakatani, and T. Ono. 'Current-induced domain wall motion in Co/Ni nano-wires with different Co and Ni thicknesses'. In: *Journal of Physics: Conference Series* 266 (2011), p. 012110.

[Újf+96] B. Újfalussy, L. Szunyogh, P. Bruno, and P. Weinberger. 'First-Principles Calculation of the Anomalous Perpendicular Anisotropy in a Co Monolayer on Au(111)'. In: *Physical Review Letters* 77 (1996), p. 1805.

[Vic89] R. H. Victora. 'Predicted time dependence of the switching field for magnetic materials'. In: *Physical Review Letters* 63 (1989), p. 457.

[Vir+05] M. Viret, A. Vanhaverbeke, F. Ott, and J.-F. Jacquinot. ‘Current induced pressure on a tilted magnetic domain wall’. In: *Physical Review B* 72 (2005), p. 140403.

[VSJ11] E. Vilanova Vidal, H. Schneider, and G. Jakob. ‘Influence of disorder on anomalous Hall effect for Heusler compounds’. In: *Physical Review B* 83 (2011), p. 174410.

[VV07] A. Vanhaverbeke and M. Viret. ‘Simple model of current-induced spin torque in domain walls’. In: *Physical Review B* 75 (2007), pp. 024411–024411.

[WV04] X. Waintal and M. Viret. ‘Current-induced distortion of a magnetic domain wall’. In: *Europhysics Letters* 65 (2004), p. 427.

[Xie+07] X. P. Xie, X. W. Zhao, J. W. Knepper, F. Y. Yang, and R. Sooryakumar. ‘Evolution of magnetic domain reversal with temperature in Co/Pt multilayers observed by magneto-optical Kerr imaging’. In: *Physical Review B* 76 (2007), p. 184433.

[Xu+08] P. Xu, K. Xia, C. Gu, L. Tang, H. Yang, and J. Li. ‘An all-metallic logic gate based on current-driven domain wall motion’. In: *Nature Nanotechnology* 3 (2008), p. 97.

[XZS06] J. Xiao, A. Zangwill, and M. D. Stiles. ‘Spin-transfer torque for continuously variable magnetization’. In: *Physical Review B* 73 (2006), p. 054428.

[YH07] C.-Y. You and S.-S. Ha. ‘Temperature increment in a current-heated nanowire for current-induced domain wall motion with finite thickness insulator layer’. In: *Applied Physics Letters* 91 (2007), p. 022507.

[You08] C.-Y. You. ‘Another method for domain wall movement by a nonuniform transverse magnetic field’. In: *Applied Physics Letters* 92 (2008), pp. 152507–152507–3.

[YSJ06] C.-Y. You, I. M. Sung, and B.-K. Joe. ‘Analytic expression for the temperature of the current-heated nanowire for the current-induced domain wall motion’. In: *Applied Physics Letters* 89 (2006), p. 222513.

[Zen+02] H. Zeng, R. Skomski, L. Menon, Y. Liu, S. Bandyopadhyay, and D. J. Sellmyer. ‘Structure and magnetic properties of ferromagnetic nanowires in self-assembled arrays’. In: *Physical Review B* 65 (2002), p. 134426.

[Zho+96] L. Zhong, M. Kim, X. Wang, and A. J. Freeman. ‘Overlayer-induced anomalous interface magnetocrystalline anisotropy in ultrathin Co films’. In: *Physical Review B* 53 (1996), p. 9770.

[ZL04] S. Zhang and Z. Li. ‘Roles of Nonequilibrium Conduction Electrons on the Magnetization Dynamics of Ferromagnets’. In: *Physical Review Letters* 93 (2004), p. 127204.

Publication List

Journal Articles

- J. Heinen, O. Boulle, K. Rousseau, G. Malinowski, M. Kläui, H. J. M. Swagten, B. Koopmans, C. Ulysse, and G. Faini. ’Current-induced domain wall motion in Co/Pt nanowires: Separating spin torque and Oersted-field effects’. In: Applied Physics Letters 96 (2010), p. 202510.
- J. Heinen, D. Hinzke, O. Boulle, G. Malinowski, H. J. M Swagten, B. Koopmans, C. Ulysse, G. Faini, and M. Kläui. ’Extraction of the spin torque non-adiabaticity from thermally activated domain wall hopping’. In: Applied Physics Letters 99 (2011), p. 242501.
- J. Heinen, D. Hinzke, O. Boulle, G. Malinowski, H. J. M. Swagten, B. Koopmans, C. Ulysse, G. Faini, B. Ocker, J. Wrona, and M. Kläui. ’Determination of the spin torque non-adiabaticity in perpendicularly magnetized nanowires’. In: Journal of Physics: Condensed Matter 24 (2012), p. 024220.

Conference Talks

- J. Heinen, J. Heidler, M. Kläui, and U. Rüdiger. ’Spin currents in magnetic nanostructures’. at: Klausurtagung SFB767, Söllerhaus (2010).
- J. Heinen, O. Boulle, G. Malinowski, C. Ulysse, G. Faini, and M. Kläui. ’Thermal activated domain wall depinning: Extraction of the non-adiabatic contribution’. at: DPG Spring Meeting, Dresden (2011).

- J. Heinen, O. Boulle, G. Malinowski, H. J. M Swagten, B. Koopmans, C. Ulysse, G. Faini, and M. Kläui. 'Thermally activated domain wall depinning: Extraction of the non-adiabaticity factor β'. at: INTERMAG, Taipeh (2011).

Posters

- O. Boulle, J. Heinen, L. Heyne, J. Rhensius, G. Malinowski, M. Kläui, U. Rüdiger, L. Le Guyader, F. Nolting, L. J. Heyderman, C. Ulysse, and G. Faini. 'Current induced domain wall motion and domain manipulation in out-of-plane magnetized nanowires'. at: DPG Spring Meeting, Dresden (2009).
- J. Heinen, O. Boulle, K. Rousseau, G. Malinowski, M. Kläui, H. J. M. Swagten, B. Koopmans, C. Ulysse, and G. Faini. 'Current induced domain wall motion in Co/Pt nanowires: Separating spin torque and Oersted field effects'. at: DPG Spring Meeting, Regensburg (2010).
- J. Heinen, J. Rhensius, M. Kläui, T. Graf, and C. Felser. 'Temperature dependent antisymmetric planar Hall effects in $\mathrm{Co_2FeAl_xSi_y}$ Heusler alloys'. at: DPG Spring Meeting, Dresden (2011).
- J. Heinen, D. Hinzke, O. Boulle, G. Malinowski, H. J. M. Swagten, B. Koopmans, C. Ulysse, G. Faini, and M. Kläui. 'Methods to extract the non-adiabaticity in high anisotropy out-of-plane magnetized nanowires'. at: SPS-Meeting, Lausanne (2011).

Acknowledgments

Cooperations, measurements, discussions, interpretations of results and a lot of work were the ingredients of this thesis, which would not have been possible without the help of many people. First of all, I want to say thank you to all who contributed to this thesis!

In particular, I thank Prof. Dr. Mathias Kläui for the possibility to join his group and this exciting field of research. I appreciate the time he spent on the many extensive and fruitful paper discussions and his support during the last years. Furthermore, I would like to thank Prof. Dr. Ulrich Nowak for writing the second referee report for this work. I also thank Olivier Boulle, who accompanied me during the first time as my supervisor giving me advice whenever needed. At this point, I would also like to thank all the other post-docs for sharing their experiences, scientific or non-scientific, leading to many ideas and discussions in and also out of the office.

Furthermore, I would like to thank Carlos Vaz, Michael Förster, Philipp Möhrke, Stephen Krzyk, Jan Rhensius, Helmut Körner, Daniel Rüffer, and Tomek Schulz for reading my thesis and for their advices, which helped a lot to improve it. I hereby thank also Prof. Dr. Gerhard Jakob for the recent discussions about the magnetoresistance effects.

Nevertheless, the content of this thesis could not have been written without the help of many people fabricating the samples. Thanks to Olivier Boulle, Gregory Malinowski, Christian Ulysse, and Giancarlo Faini for the design and fabrication of the Co/Pt based multilayer materials, Berthold Ocker and co-workers of Singulus Technologies AG for fruitful discussions and the preparation of the Co/Ni based multilayer materials, the group of Dafine Ravelosona for providing the Co/Ni-CoFeB sample, the group

of Claudia Felser for the fabrication of the Heusler alloys, Jan Rhensius and André Bisig for the patterning and contacting of the many nanostructures. Besides, I thank all the people from the mechanical and electrical workshops in Konstanz and at PSI, who helped us to get the measurement setup running. Especially the realization of the electrical wiring of the sample holder was cumbersome work. I also would like to acknowledge the financial support by the DFG (SFB767) and the EU STREP project MAGWIRE.

Apart from the scientific work, I appreciated the hours in the coffee corner and at PSI, where I got to know so many nice people. I thank you all for the funny and most interesting discussions, which cheered me up so many times. I wish you all the best for the future! I hereby also thank Jura for the creation of a coffee machine providing me with a lovely black liquid whenever needed.

Finally, for friendship, open minds for my 'brain-outsourcing' and much more, I would like to express my gratitude to all those, who helped me during the ups and downs of my thesis. You always listened to my problems and found words of encouragement.

Dieser Dank gebührt umso mehr meiner Familie, die mich stehts unterstüzt hat und mir mein Studium ermöglichte. Vorallem möchte ich hier meiner Frau danken, die mir stehts zur Seite stand und immer für mich da war!